

POLITECNICO DI TORINO

Faculty of Engineering
Master Degree in Electronics Engineering

Master of Science Thesis

A Novel Inductive Simultaneous Wireless Information and
Power Transfer System to Neural Dust Implants
for Reverting Blindness



Supervisors:

Prof. Danilo Demarchi
Prof. Sandro Carrara

Candidate:

Fabio Asti

Co-supervisors:

Dr. Paolo Motto Ros
Eng. Gian Luca Barbruni

April 2021



EPFL

A Novel Inductive Simultaneous Wireless Information and
Power Transfer System to Neural Dust Implants
for Reverting Blindness

Politecnico di Torino

Faculty of Engineering

Department of Electronics and Telecommunications (DET) - Turin, Italy

Academic year: 2020 - 2021

École polytechnique fédérale de Lausanne (EPFL)

Faculty of Engineering

Microcity Integrated Circuit Laboratory (ICLAB) - Neuchâtel, Switzerland

Academic year: 2020 - 2021

Supervisors:

Prof. Danilo Demarchi

Politecnico di Torino

Turin, Italy

Prof. Sandro Carrara

École polytechnique fédérale de Lausanne

Neuchâtel, Switzerland

Candidate:

Fabio Asti

Turin, April 2021

*Alla mia Famiglia,
e a tutti coloro che mi sono
stati accanto fino alla fine.*

*«Siate artefici del vostro destino e protagonisti
del cambiamento che favorisce crescita e sviluppo»
Antonio Pompeo*

*«L'umiltà e l'apertura di colui che è alle prime armi
facilitano l'esplorazione, e l'esperimento porta al compimento.
Tutto comincia con il primo, piccolo, timoroso passo»
La via dell'artista, Julia Cameron*

Acknowledgements

I am grateful for wise advice, huge support and precious encouragement received from many people during my academic years and throughout this research. First, I would like to extend my gratitude toward my thesis supervisor, Prof. Danilo Demarchi and Prof. Sandro Carrara, sources of inspiration and humanity. They have always been ready to advise me and contribute to my work with precious and valid suggestions, useful remarks and interesting discussions. It was a pleasure and honour to work under their supervision. They trusted me, allowing me to pursue my master studies at Microcity Integrated Circuit Laboratory (ICLAB) at École Polytechnique Fédérale de Lausanne (EPFL) in Neuchâtel, Switzerland. I feel lucky for the opportunity to participate in a multidisciplinary project in my field of interest, collaborating with prestigious institutions towards a solution that has the potential to improve the life's quality of millions of patients. This possibility has represented the most suitable MSc project that has been the ideal end to my university carrier and an entry point into the area in which I wish to work in the future.

I would like to thank my associate supervisor, Eng. Gian Luca Barbruni, to have supported me everyday working side by side. A deep gratitude for positive critical eye and the trust in my work, which has made possible my academic and personal growth during these last months. A deep honour to have collaborated with him, punctual references, sources of knowledge and consulting. It has been a big pleasure, as well as a great occasion. I am also sincerely grateful to Dr. Paolo Motto Ros for his practical advices and insightful comments. I thank Politecnico di Torino for providing me part of financial support throughout my academic master thesis project sustained abroad. I would like also to thank the administrative employee, Julie, for her precious availability because she had taken care of me. Even from the very first day I arrived in Neuchâtel, I had the opportunity to make friends who made me feel at home. I want to mention Sonia, Leonardo, Flavio, Arianna, Luigi, Karim and Benjamin. I want to express my gratitude to Prof. Maurizio Zamboni for having indicated and advised me on the path to take for my master's studies. I greatly appreciate his guidance and his precious counseling.

The academic years are somehow like a travel, where the travel-mates are as important as the destination. For this reason, a heartfelt thanks goes to all those friends that have been with me during this path studded with satisfactions and efforts and during this constructive experience lived abroad; who have shared with me feelings, emotions, knowledge and, most important, time. I am thankful to all of you to have ironed outsides of my being.

To conclude, the most heartfelt thanks to my family and my friends. With their unconditioned love, they have supported me during my academic years. They shared my successes and helped me during the times of discouragement. They helped me to distinguish the details from the important things. Their aid and their constant support have been fundamental and I would not have reached this achievement without them. It is nice to know that I can always count on you. You sustain has been, since always, a source of motivation and a spur not to give up in difficult moments.

I treasure what people, time, life and God have given me.

Fabio Asti

Ringraziamenti

Penso sia doveroso dedicare e spendere ancora qualche sentita parola alle persone che hanno contribuito al raggiungimento di questo traguardo, consapevole che queste poche righe non saranno mai sufficienti ad esprimere la mia immensa gratitudine.

La distanza in senso lato rivela la ricchezza e l'importanza di alcuni rapporti, e di alcuni legami. Quelli veri e sinceri li porta alla luce, e non può altro che renderli più forti.

In primis ringrazio di cuore i miei genitori, per me preziosa fonte di sostegno e di coraggio. Grazie per il vostro impegno morale e materiale, supportandomi di fronte ad ogni difficoltà e avversità incontrata. Immensamente grato.

Ringrazio mio fratello, solido punto di riferimento e uno dei più grandi regali a me concessi. A modo suo è in grado di supportarmi e sopportarmi.

Ringrazio la mia famiglia che mi ha sempre sostenuto e appoggiato in ogni mia scelta. Ringrazio i miei nonni, zii e cuginetti.

Un ringraziamento speciale va a nonna Filomena, esempio di vita, fonte di saggezza, la persona a cui devo tanto. Considerata la mia fidata consigliera. Mi ha sempre sostenuto nell'affrontare ogni difficoltà guidandomi saggiamente nell'affrontare le scelte più difficili e spronandomi quotidianamente a dare il massimo. Questo traguardo lo devo soprattutto a lei.

Un ringraziamento altrettanto speciale va sicuramente a chi ha condiviso con me questo percorso. Un sentito grazie va a due persone per me molto importanti, Pepe e Sara. Persone che ritengo dei fratelli acquisiti, fedeli confidenti, quotidiane spalle su cui poter sempre contare. Una di quelle amicizie che sono ricchezza rara da preservare. Pepe, il tuo quotidiano esempio mi ha trasmesso instancabilmente bontà d'animo, spirito critico e la capacità di sapere mettere nella giusta dose dedizione e curiosità in ogni cosa. Sara, il tuo rassicurante sostegno e le tue sagge parole mi hanno quotidianamente spronato. Grazie per le chiacchierate e per i consigli da vera sorella maggiore. A te che mi conosci meglio di quanto io conosca me stesso. Faccio tesoro di ogni vostra parola e di ogni vostro insegnamento. Ringrazio dal profondo del mio cuore Marilena e Nicola per avermi amato e trattato come un figlio. Ringrazio l'*Ostello Ferotti* per avermi accolto e fatto sentire ogni giorno come a casa. Avete alleggerito ogni fatica e ogni peso.

Ringrazio il mio gruppo di studio e i miei colleghi più stretti coi quali ho condiviso la mia quotidianità accademica, e non solo. Pepe, Giuliana e Gianluca; a noi che ci siamo trovati e che ci siamo saputi completare l'un con l'altro. Siete stati un valido punto di riferimento. Grazie per l'enorme pazienza che avete avuto nei miei confronti, per aver sopportato i miei sbalzi d'umore nei momenti di sconforto, per avermi spronato a dare il massimo e per non aver mai dubitato delle mie potenzialità.

Grazie ai miei compagni di corso che hanno contribuito a rendere le lezioni meno pesanti, rendendo questi anni accademici indimenticabili. Un grazie particolare a Lavinia, Dario, Gabriele, Giulia, Francesco, Ludovica e Andrea.

Ringrazio Luca, uno stretto collega di studio, un sincero confidente, un fidato compagno di avventure, un grande amico.

Ringrazio Valeria, persona speciale ed insostituibile. Un'amica su cui poter contare sempre.

Ringrazio anche chi piano piano si è fatto strada nella mia vita, contribuendo ad arricchire le mie giornate con piccoli sentiti gesti, creando sani legami che spero possano divenire sempre più saldi.

Ringrazio Lisa, per le chiacchierate durante le notti di volontariato in Croce Verde, per la sua preziosa amicizia, e per aver creduto quotidianamente in me.

Ringrazio Ruben, un amico di grande bontà d'animo.

Ringrazio Marco, Andrea e Michele, i più stretti compagni di scuola superiore sempre presenti nei traguardi più importanti della mia vita.

Ringrazio Mich e Francesca, due amiche dolcissime e di grande umiltà e saggezza. Siete una sincera ricchezza nella mia vita.

Ringrazio Ilaria e Andrea, riferimenti puntuali, e fonte di ispirazione e umanità.

Ringrazio Davide, Eleonora e Giulia, perchè in modo del tutto inaspettato e in poco tempo sono diventati buoni amici in grado di capirmi e con cui condividere momenti di puro divertimento.

Ringrazio *Young First* e la Prima Squadra della Croce Verde di Torino con la quale ho avuto la fortuna di condividere tra le più emotive e importanti esperienze della mia vita.

Ringrazio i *Pisciaturi*: Brunella, Diego e Francesca. Amici di avventure, e non solo. Amici coi quali ho condiviso le migliori risate e i migliori momenti di follia. Degli amici davvero speciali. Le nostre chiacchierate, le nostre sincere risate, le nostre cene "leggere" saranno dei ricordi indelebili.

Ringrazio Prof. Emilio, l'uomo a cui devo tanto; fonte di ispirazione e mio quotidiano esempio, che ha reso possibile la mia crescita professionale e personale.

Ringrazio Emilio, prezioso amico e mia personale guida spirituale, che ha sempre accompagnato la mia crescita nella preghiera.

Desidero ringraziare tutti coloro che in questi anni mi hanno sostenuto, spronato e incoraggiato, tutti coloro che hanno camminato accanto a me e con il quale siamo cresciuti insieme, condividendo un pezzo di metaforica strada. Un ringraziamento speciale va ai miei cari amici.

Spesso la quotidianità della vita si rivela tutt'altro che monotona, concedendoci doni inaspettati. La mia famiglia e i miei amici sono un regalo tutt'altro che scontato, forse immeritato, ma di cui non smetterò mai di esserne grato.

Faccio tesoro di ciò che le persone, il tempo, la vita e Dio mi hanno regalato.

Neuchâtel, Switzerland

April 2021

Fabio Asti

Abstract

Nowadays, the technological impact is becoming more and more significant, playing also an essential role in the diagnosis and the treatment of human diseases. An innovative solution is the new emerging concept of *Smart Dust*, introduced for the first time at the UC Berkeley. Smart Dust research investigates the feasibility of a future real-time diagnostic and therapy medicine. The two branches in biomedical are the *Body Dust* and the *Neural Dust*. Body Dust research aims at a new concept of shrinkable and drinkable electronics which can flow through the human blood for real-time monitoring. Neural Dust aims instead at a new generation of safely powered devices, micron-sized and freely distributed in the human brain, targeting and treating mental disorders and neuropathologies. Among the others, Neural Dust approach can be used to address illnesses like Parkinson's disease, epilepsy, Alzheimer's disease and blindness.

Blindness is a medical condition which affects more than 32 millions people worldwide. Some of these patients may be treated or operated while the remaining part, represented by 35%, is affected by incurable and unpreventable diseases. Several prosthetic approaches were proposed over the last years. Retinal prostheses showed the best clinical trial performances on patients affected by external retinal layer dystrophies (e.g. retinitis pigmentosa or dry age-related macular degeneration). Nevertheless, the above-mentioned diseases affect only a small fraction of blind patients worldwide, less than 7%. Recently, cortical visual prostheses have shown a tremendous impact on the future of neural implant since they might address every form of blindness. Miniaturisation and large-scale distribution are key factors for the next generation cortical visual prostheses. The whole research in this field aims to develop an array of thousands, free-floating, ultra-miniaturised and wirelessly powered CMOS-pixels to selectively stimulate the visual cortex of the human brain to restore vision. The idea is to replicate the common path of a safe visual system. First, the video camera records the images. Second, the external base station transmits simultaneously power and data to the neural implants. Third, once the single-pixel stimulates the brain, the phosphene perception is induced at a precise spatial location. To reach the goal, several sub-systems need to be investigated and developed to address the several technical issues along this pathway. This thesis proposes a novel radio-frequency simultaneous wireless information and power transfer system for Neural Dust application. The radio-frequency transmitter operates at 433.92 MHz of the industrial, scientific and medical band. The new proposed structure efficiently modulates the carrier exploiting an amplitude-shift keying modulation and reaching a data rate as high as 20 Mbps together with a variable modulation index as low as 8%. The complete system has been designed, manufactured and tested. Results highlight the feasibility to transmit a carrier signal at 433.92 MHz, combining power transfer with a novel amplitude-shift keying modulation structure. The final system has been compared with the current state-of-the-art showing one of the highest data rate while maintaining robustness and gain. In the future, this transmitter will be further optimised and integrated on a printed circuit board, ready to be used with the next generation cortical visual prostheses to revert blindness.

Keywords: Wireless Power Transfer; Inductive Power Transfer; RF Transmitter; ASK Modulator; SWIPT Systems; Implantable Medical Device; Neural Implants; Cortical Visual Prostheses; Miniaturisation.

Sommario

Col significativo l'impatto tecnologico, la diagnosi e il trattamento di alcune malattie rivestono un ruolo sempre più importante. Una soluzione innovativa è basata sul concetto di *Smart Dust*, introdotto per la prima volta all'Università di California «Berkeley». Oggigiorno, lo Smart Dust indaga sulla fattibilità di una medicina real-time per la diagnosi e la terapia, e si classifica in *Body Dust* e *Neural Dust*. La ricerca del Body Dust mira ad un nuovo concetto di elettronica miniaturizzata in grado di fluire nel sangue per un monitoraggio real-time. Invece, la ricerca del Neural Dust mira ad una nuova generazione di dispositivi miniaturizzati posizionati nel cervello alimentati in modalità wireless, mirati alla cura di disturbi mentali e di neuropatologie. La “polvere neurale” può essere sfruttata per combattere il morbo di Parkinson, l'epilessia, il morbo di Alzheimer e la cecità.

Oltre 32 milioni di persone in tutto il mondo necessitano di protesi visive per il recupero della funzione visiva. Soltanto alcuni di questi pazienti possono essere soggetti a cure o operazioni chirurgiche, in quanto la restante parte, rappresentata dal 35%, risulta affetta da malattie incurabili e non prevenibili. Negli ultimi anni sono stati proposti e discussi diversi nuovi approcci protesici. Le protesi retiniche hanno mostrato le migliori prestazioni nella sperimentazione clinica su pazienti affetti da distrofie dello strato retinico esterno, come la retinite pigmentosa o la degenerazione maculare secca legata all'età. Tuttavia, le malattie sopra menzionate colpiscono solo una piccola parte dei pazienti ciechi nel mondo, meno del 7%. Recentemente, le protesi visive corticali hanno mostrato un enorme impatto sul futuro degli impianti neurali poiché potrebbero affrontare qualsiasi forma di cecità.

La miniaturizzazione e la distribuzione su larga scala sono fattori chiave per le protesi visive corticali di prossima generazione. A tal proposito, una sfida tecnologica è lo sviluppo di chip miniaturizzati indipendenti, senza batterie e alimentati in modalità wireless. Questa ricerca mira a sviluppare una serie di migliaia di wireless pixel CMOS ultra-miniaturizzati per stimolare selettivamente la corteccia visiva del cervello umano. Innanzitutto, il modello necessita di una telecamera esterna in grado di registrare le immagini. Successivamente la stazione base esterna trasmetterà sia alimentazione sia dati agli impianti CMOS. Infine, una volta che il singolo pixel stimola il cervello, la percezione del foscene viene indotta.

Tra i tanti differenti sotto-blocchi necessari per raggiungere lo scopo, questa tesi propone un nuovo sistema innovativo di trasferimento simultaneo wireless di potenza e di informazioni a più chip miniaturizzati e alimentati induttivamente. È stato progettato, simulato, realizzato e testato un trasmettitore a radiofrequenza operante a 433,92 MHz della banda industriale, scientifica e medica. In particolare, viene proposto un innovativo sistema in grado di modulare in maniera efficiente il segnale portante, sfruttando una modulazione di tipo amplitude-shift keying in grado di raggiungere data rate fino a 20 Mbps con indice di modulazione variabile fino all'8%. Il sistema finale è stato confrontato con l'attuale stato dell'arte evidenziando i molteplici vantaggi di questo nuovo trasmettitore. Il sistema proposto fornisce uno dei data rate più elevati se confrontato ai precedentemente lavori pubblicati e presenti in letteratura, pur garantendo una buona robustezza e un alto guadagno. In futuro, il trasmettitore presentato sarà ulteriormente ottimizzato e integrato su un circuito stampato per le protesi visive corticali di futura generazione al fine di combattere la cecità.

Contents

List of Figures	XIII
List of Tables	XVI
Listings	XVII
List of Acronyms and Symbols	XVIII
1 Introduction: The Impact of Medical Technology on Healthcare	1
1.1 Visual Retinal Prostheses	2
1.2 Challenges in Neural Stimulation	4
1.3 Smart Neural Dust to Revert Blindness	4
1.3.1 Master Thesis Outline	5
2 Miniaturised Neural Implants: State-of-the-Art	6
2.1 StimDust	6
2.2 Microbead	7
2.3 ENGINI	8
2.4 Neurograins	8
2.5 Comparison with Akin Projects	9
3 Wireless Power Transfer and Data Communication in Neural Implants	11
3.1 Wireless Power Transfer	11
3.1.1 Far-field Radiation	13
3.1.2 Acoustic Power Transfer	13
3.1.3 Capacitive Power Transfer	14
3.1.4 Inductive Power Transfer	15
3.2 Wireless Data Transmission	19
3.2.1 Amplitude-Shift Keying	20
3.2.2 On-Off Keying	21
3.2.3 Frequency-Shift Keying	22
3.2.4 Phase-Shift Keying	22
3.2.5 Pulse Modulation Technique	22
4 System Concept: Considerations	24
4.1 WPT Method	26
4.1.1 Misalignment and Angular Rotation	26
4.2 Frequency Selection	27
4.2.1 Specific Absorption Rate	27
4.2.2 IEEE Standard for Safety Levels	27

4.2.3	Tissue Adsorption	29
4.2.4	Optimal Operating Frequency	31
4.3	Modulation Technique	32
4.3.1	Data Rate	32
4.4	SWIPT System Specifications: Summary	33
5	RF SWIPT Transmitter: System Design and Architecture	34
5.1	Low Frequency Pierce Oscillator	36
5.1.1	LF Pierce Oscillator Design Procedure	37
5.1.2	LF Pierce Oscillator Simulation and Implementation	38
5.2	Phase-Locked Loop	42
5.2.1	PLL Design and Simulation	42
5.2.2	PLL Implementation and Analysis	45
5.3	Amplitude-Shift Keying Modulator	46
5.3.1	ASK Modulator Design Procedure	47
5.3.2	ASK Modulator Simulation	50
5.3.3	ASK Modulator Implementation	53
5.4	Power Amplifier	55
5.4.1	PA Design Procedure	57
5.4.2	PA Implementation and Analysis	58
5.5	Transmitting Coil	64
5.5.1	Coil Design Procedure	64
5.5.2	Coils Design and Simulation	65
5.5.3	Coils Measurements	68
6	Results and Discussion	71
6.1	Commercial Integrated RF Transmitter Comparison	75
7	Conclusions	78
7.1	Future Works	79
A	Insights	80
A.1	Comma to Dot Conversion Function	80
A.2	Graph Code of Conductivity and Relative Permittivity	80
A.3	Graph Code of Gain and Efficiency of Power Amplifier	82
A.4	Design Equations Resolution of Amplitude-Shift Keying	83
A.5	Absolute Decibel: dBm to Watt Conversion	84
A.6	Graph Code of S11 vs Frequency	85
A.7	Graph Code of Absorbed Power	86
	References	87

List of Figures

1.1	Closed-loop responsive neurostimulation system. Reprinted from [12].	2
1.2	Simulation of the visual stimulus, the simulated responses of the Retinal Ganglion Cell (RGC) and the linear reconstruction in healthy retina. Reprinted from [15].	3
1.3	Simulation of the visual stimulus, the simulated responses and linear reconstruction with retinal prosthesis. Reprinted from [15].	3
2.1	State-of-the-art of sub-mm implantable neural systems. Diagram of StimDust wireless neural stimulator system with close up view of the Stim Dust mote. Reprinted from [17].	7
2.2	State-of-the-art of sub-mm implantable neural systems. (a) Three-dimensional drawings of Microbead in the human brain; (b) view of the transmitting coil; (c) the packaged Microbead with one couple of electrode for recording and other one for stimulating. Reprinted from [19].	7
2.3	State-of-the-art of sub-mm implantable neural systems. ENGINI platform concept with IPT neural microstimulator. Close up view of the single probe with approximate dimensions. Reprinted from [20].	8
2.4	State-of-the-art of sub-mm implantable neural systems. Neurograins platform concept with size scale of the chip. Reprinted from [21].	9
2.5	State-of-the-art of various powering schemes of sub-mm implantable neural systems. Reprinted from [16].	9
3.1	Qualitative comparison described through three-dimensional histogram for different methods for WPT. Reprinted from [37].	12
3.2	Graphical representation of IPT, CPT and APT with the qualitative optimal distances in the proper working condition. Reprinted from [37].	13
3.3	Equivalent circuit model for a generic ultrasonic wireless link. Reprinted from [37]. . .	14
3.4	Equivalent circuit model for a generic capacitive coupling wireless link. Reprinted from [37].	15
3.5	Equivalent circuit model for a generic inductive coupling. Reprinted from [37].	16
3.6	Lumped circuit models of a conventional 3-coils IPT links. Reprinted from [37].	17
3.7	Three-dimensional simulations of PTE and PDL in different IPT configurations in function of the coupling distance d_{xy} and coupling coefficient k_{xy} . (a) PTE and (b) PDL for 3-coils IPT link; (c) PTE and (d) PDL for 4-coils IPT link. Reprinted from [44]. . .	18
3.8	Comparison between the transfer power efficiency (PTE) and the delivered power (PDL) as a function of d_{23} for 2-, 3-, and 4-coils IPT method. Values extracted from [44]. . .	19
3.9	Graphical digital modulation schemes. (a) ASK; (b) OOK; (c) FSK; (d) PSK; (e) PWM-ASK. Reprinted from [51].	23
4.1	Main blocks of the planned Smart Micro Neural Dust.	25
4.2	Behaviour of conductivity σ (S/m) in function of Frequency (Hz) with step of 20 MHz.	29

4.3	Behaviour of relative permittivity ϵ_r in function of Frequency (Hz) with step of 20 MHz.	30
4.4	Choice of the optimal operating frequency of ENGINI's project in function of the PDL and under SAR restriction. Reprinted from [20].	31
5.1	General scheme for a 3-coils IPT link. In red, the RF SWIPT transmitter proposed in this work.	34
5.2	Main blocks of the external RF SWIPT transmitter: (A) LF Pierce oscillator; (B) PLL; (C) ASK modulator; (D) PA; (E) Transmitting coil.	35
5.3	Lumped circuit model of a quartz crystal. Reprinted from [78].	36
5.4	Crystal reactance vs. frequency. Reprinted from [78].	36
5.5	Pierce oscillator circuit implemented on LTspice with designed values.	38
5.6	LF Pierce oscillator simulations on LTspice. (a) Total view; (b) Close-up view around 10 ms.	39
5.7	Simulations of quartz crystal at (a) non-resonance frequency and (b) resonance frequency.	39
5.8	(a) Implementation of LF Pierce Oscillator on the breadboard. (b) Measurement of 13.56 MHz. Curves displayed on DSO with estimation of the frequency f_{ref} .	40
5.9	TB of LF Pierce oscillator.	41
5.10	Block diagram and functional units of PLL.	42
5.11	Main settings to determine the optimal choice of PLL defying: (a) Starting options; (b) Output frequency requirements; (c) Loop Filter Selection; (d) PLL chip selection. Settings extracted from <i>ADIsimPLL</i> software.	43
5.12	(a) Simulation software provides recommended values for setup registers. Settings extracted by <i>ADIsimPLL</i> software. Simulations of (b) PLL RF_i and (c) phase noise.	44
5.13	Schematic of LTC9648-1 of <i>Analog Devices</i> .	45
5.14	Measurement of the PLL output RF_i extracted from DSO.	45
5.15	The conceptual waveform for ASK modulation related to the input binary information. (a) The transmitted digital signal in input; (b) Waveform of ASK modulation corresponding binary information.	46
5.16	Schematic of a data and power transmission system with drain amplitude modulator and a class-E power amplifier.	47
5.17	ASK modulation circuit of a Darlington emitter-follower approach working at 10 MHz and with a data rate of 1 Mbps.	48
5.18	Basic waveforms simulation of the proposed topology. The red and blue sine waves are the carrier and the modulated signal, respectively. The green square wave simulates the input data.	48
5.19	Simulation of basic waveforms of the ASK modulator of the proposed topology working at 433.92 MHz and with a data rate of 10 Mbps. The red and blue sine waves are the carrier and the modulated signal, respectively. The green square wave simulates the input data.	50
5.20	Schematic of the new approach based on switch between two tuned modes.	50
5.21	(a) Conceptual idea of the new approach based on switch between two tuned modes described through block diagrams. (b) Simulation with the output of scope.	51
5.22	Circuit of the new approach based on switch between two tuned modes. Schematic realized on MultiSim software.	52
5.23	Simulation of the new approach based on the switch between two tuned modes.	53
5.24	Evaluation board and circuit of the M3SW-2-50DRA+ by Mini-Circuits'. Extracted from the datasheet.	54
5.25	ASK output with different MIs. Extracted from DSO.	54
5.26	Basic schematic of a class-E power amplifier driving an IPT link. Figure extracted from [91].	56

5.27	Description of the effects of adjusting load-network components C_1 , C_2 and L_2 on V_{DS} waveform. Reprinted from [92].	56
5.28	Detailed description of the effects of adjustment procedure of the C_1 and C_2 components on V_{DS} waveform. The vertical arrow represents the transistor M_1 turn-on. Reprinted from [92].	57
5.29	Evaluation board schematic at 900 MHz lumped element. The variations of passive component's values are reported in red colour in order to tune the Demo Board in the range 350 to 430 MHz, for $P_{in} = 0$ dBm, $P_{out} \geq 34$ dBm, $V_{CC} = 3.6$ V. Figure extracted from the datasheet provided by <i>Qorvo</i> company.	59
5.30	Typical test setup with evaluation board PCB information. Figure extracted from the datasheet provided by <i>Qorvo</i> company.	59
5.31	Implementation of the Evaluation Kit on breadboard with 3 dB attenuator on the left and the 6 dB attenuator on the right. Presence of jumper wires to power up the Demo Board with the two different voltages. The red wires are V_{DD} , the blue ones are V_{APC} and the black ones are ground.	60
5.32	Qualitative gain and PAE behaviour vs P_{out} at 430 MHz. Graphs derived from values declared in the <i>Qorvo</i> RF5110 PA's datasheet.	62
5.33	Testbench of PA.	62
5.34	Display of the Signal Analyzer instrument. Peak of frequency at 433.92 MHz when the input power P_{in} is fixed to -30 dBm.	63
5.35	Variants for the coil design. (a) squared PSC; (b) circular PSC; (c) solenoid WWC. Reprinted from [37].	65
5.36	Equivalent circuit for an inductive link with (a) series and (b) parallel-resonant cases. Reprinted from [99].	65
5.37	HFSS design model. (a) Transmitting coil. (b) Close up view.	66
5.38	Ansys HFSS project manager of the transmitting coil.	66
5.39	Ansys HFSS simulation. Quality factor Q of the Tx coil with $d_{Tx} = 40$ mm.	67
5.40	Ansys HFSS simulation of the Tx coil with $d_{Tx} = 40$ mm. (a) Series inductor L_s ; (b) Series resistance R_s	68
5.41	Coils implementation. (a) Conceptual front view of the coil, reprinted from [102]. (b) Tx and Rx coils realized on FR4 substrate.	69
5.42	VNA measurements of the Tx coil with $d_{Tx} = 40$ mm. Series inductor L_s (Trace 2); (b) Series resistance R_s (Trace 1).	69
5.43	S_{11} (dB) vs Frequency (Hz). VNA measurement in blue and Ansys HFSS in light blue.	70
6.1	Testbench of the RF ASK transmitter.	71
6.2	Measurement of the RF ASK transmitter.	72
6.3	Measurement of the RF ASK transmitter with random string of bits in input.	72
6.4	Measurements extracted with DSO with different design of MI and data rate.	73
6.5	Pie chart of $P_{absorbed}$ required by the main blocks of the RF SWIPT transmitter.	75
6.6	Schematic of the RF SWIPT transmitter for the PCB.	77
7.1	Complete system overview of Smart Micro Neural Dust for reverting blindness.	79
A.1	dBm to Watt Conversion. Example value of 34 dBm with its respective value converted in mW.	85

List of Tables

2.1	Comparison of state-of-the-art sub-mm free-floating neural IMDs. Reprinted from [16].	10
3.1	Bus Invert coding application. Reprinted from [52].	22
3.2	State-of-the-art of data telemetry methods for IMD applications. Reprinted from [47].	23
4.1	SAR limits in different countries. Reprinted from [66].	28
4.2	Maximum permissible exposure for controlled environments. Table extracted from [63] and edited.	28
4.3	Relative permittivity ϵ_r and electrical conductivity σ of the body tissues. Reprinted from [69].	30
4.4	System and design specs of the external SWIPT RF transmitting system.	33
5.1	Typical range values for feedback resistor R_f . Reprinted from [79].	37
5.2	Designed theoretical parameters and final chosen parameters based on available standard values. Reprinted from [86].	47
5.3	Key features and electrical specifications of the RF5110G power amplifier. Values extracted from the datasheet provided by <i>Qorvo</i> company.	58
5.4	Experimental values extracted in laboratory with evaluation board.	61
6.1	State-of-the-art comparison of RF transmitter on IPT link.	74
6.2	Absolute values of the absorbed power.	75
6.3	Comparison of fully integrated transmitters present on the market.	76

Listings

A.1	Matlab code: comma to dot conversion function.	80
A.2	Matlab code: plot of electrical conductivity σ and relative permittivity ϵ_r	80
A.3	Matlab code: plot of gain and efficiency of power amplifier.	82
A.4	Matlab code: design equations resolution of amplitude-shift keying.	83
A.5	Matlab code: dBm to Watts conversion function.	84
A.6	Matlab code: S_{11} (dB) vs frequency (Hz).	85
A.7	Matlab code: pie graph of absorbed power	86

List of Acronyms and Symbols

AD	Analog Devices
AMD	Age-related macular degeneration
APT	Acoustic power transfer
ASIC	Application specific integrated circuit
ASK	Amplitude-shift keying
BER	Bit error rate
BPSK	Binary phase shift keying
BTSL	Body tissue simulating liquid
BW	Bandwidth
CI	Cochlear implant
CMOS	Complimentary metal-oxide semiconductor
CSF	Cerebrospinal fluid
CVP	Cortical visual prostheses
CW	Continuous Wave
DR	Data rate
DSO	Digital signal oscillator
FCC	Federal Communication Commission
FoM	Figure of merit
FSK	Frequency-shift keying
HFSS	High frequency structural simulator
HTSL	Head tissue simulating liquid
IC	Integrated circuit
IEU	Implantable electronic unit
IMD	Implanted medical device
IPG	Implantable pulse generator
IPT	Inductive power transfer
ISM	Industrial scientific medical
kbps	Kilo-bit per second
LF	Low frequency
LP	Low power
LSK	Load-Shift Keying
Mbps	Mega-bit per second
MEA	Micro-electrode array
MI	Modulation index
MSB	Most significant bit
OOK	On-Off Keying
PA	Power amplifier
PCB	Printed circuit board
PD	Phase Detector
PDL	Power delivered to the load
PLL	Phase-locked loop

PMW	Pulse width modulation
PPM	Pulse position modulation
PSC	Printed spiral circuit
PSK	Phase-shift keying
PTE	Power transfer efficiency
PZT	Piezocrystal Zirconate Titanat
RF	Radio-frequency
RGC	Retinal ganglion cell
RP	Retinitis pigmentosa
RX	Receiver
SAR	Specific absorption rate
SMA	Sub-miniature version A
SNR	Signal-to-noise ratio
SPI	Serial peripheral interface
SRF	Self-resonant frequency
STM	STMicroelectronic
SWIPT	Simultaneous wireless information and power transfer
TB	Testbench
TDMA	Time Division Multiple Access
TSMC	Taiwan Semiconductor Manufacturing Company
TX	Transmitter
US	Ultrasound
VCO	Voltage controlled oscillator
VNA	Vector network analyzer
WPT	Wireless power transfer

Chapter 1

Introduction: The Impact of Medical Technology on Healthcare

The technological innovation is significantly changing modern medicine. Nowadays, the role of bio-engineering is crucial in diagnostic, prevention and therapy, inasmuch neurological diseases and mental disorders affect a large fraction of the human population.

Neurotechnology is a growing research area for treating neurological diseases and mental disorders, which affect a large fraction of the population. Inductive power links result the best with respect to transcutaneous connectors in Implantable Medical Devices (IMD) used to stable long-term operation such as retinal implants, deep brain stimulators and invasive brain-computer interfaces. The high risk of infections characterizes the latter, and the presence of implantable batteries occupy a substantial amount of volume [1], without considering that they have a limited lifetime [2]. Nowadays, a new class of wireless neural implantable devices is emerging to minimize the links between the Micro-Electrode Array (MEA) and the IMD. In this way, the μ motions of the μ electrode array in the brain are reduced, alleviating any inflammation and sheath formation responsible for chronic neural tissue damages. In engineering terms, these μ motions affect the measurements causing degradation in Signal-to-Noise Ratio (SNR) and resulting in low neuronal viability. Therefore, an implantable neural system requires bio-integration exploiting flexible and thin electronics, wireless power and data capability, bio-compatibility and chronic recording properties. A new technology that satisfies these requirements proposes an innovative solution for improving the neural monitoring and treatment exploiting μ electrode, called Neural Dust.

The Smart Dust concept has been introduced only over the last 20 years, and it has been recently defined as «well beyond the present concepts of wearable or implantable devices» [3]. Nowadays, the Dust research aims to investigate the feasibility of a future real-time development of diagnostic and treatment systems, exploiting safely powered devices on the order of tens of microns implanted in the body or in the brain [4]. However, the present target size is dramatically out of the order of magnitude with respect to the original aims. In fact, the feasibility mote's size achievable nowadays is cubic centimetres due to the microfabrication technology's limitations and due to the shrinking's restrictions of the technological node. Instead, the desirable one is about a cubic millimetre [5]. With respect to applications, mainly, the Smart Dust is classified in: i) Body Dust, which is a new concept of shrinkable and drinkable electronics which can flow through the human blood [6][7], and ii) Neural Dust, that is a new generation of ultra-miniaturised and wirelessly powered devices, freely distributed in the human brain, for neural applications [8]. The first published Neural Dust work appeared in literature in 2013 by proposing an ultra-small, ultrasound-based neural recording system [8]. On the other hand, Body Dust appeared in literature many years before. For instance, in 2005, Michael

Sailor and collaborators used the Smart Dust concept for biochemical sensing exploiting the Fourier transforms on spectra by Fabry–Pérot interference phenomenon. [9].

1.1 Visual Retinal Prostheses

Regarding a brief hint of the history of the visual retinal prostheses, their first notion came about in the second part of the 18th century, when Charles Le Roy reported a blind subject seeing light when he was applying an electric low-intensity current on the ocular surface. Two centuries later, Inoue and Potts demonstrated that electrical current elicited phosphenes, evoking responses from the electrodes located in the brain’s occipital area. In the last forty years, improvements in μ fabrication and bio-materials have carried developments on retinal surgery, allowing progress in the research of retinal prosthetics [10].

Blindness is associated with disease and degeneration of the retina, limiting the flow of visual information sent by the eye towards the brain. More precisely, the significant pathologies which lead to blindness are related to diseases and impairment of the photoreceptors, such as Retinitis Pigmentosa (RP) or degenerative conditions favoured also by Age-related Macular Degeneration (AMD) [11]. Photoreceptors are special cells present in the retina of the eyes responsible for converting light into signals accurately sent to the brain’s occipital area accountable for the visual part.

Cortical Visual Prostheses (CVP) have shown promising result in neurostimulation [12]. Nevertheless, CVPs are limited by their mechanical compliance, complex surgical approach due to the wiring from the neural interface to the Implantable Pulse Generator (IPG), and low resolution due to the limited number of electrodes that can be addressed with wires and implantable IPGs. This design principle has some critical limitations, thus imposing strict constraints on surgical procedures. Implantable Electronic Units (IEUs), connectors, and cables are weak points, often leading to the system’s failure since they exert tractions and mechanical stresses on tissues and the MEA. In particular, the transcranial or transcutaneous cables may lead to post-surgical complications (e.g. infections). IEUs are often limited by excessive heat generation, huge leakages due to the wet environment and power consumption. All these limitations hindered the development of devices like CVPs. In neurostimulation, the new challenge is to achieve a genuinely wireless array composed of freestanding electrodes, not relying on IEU and wired connections.

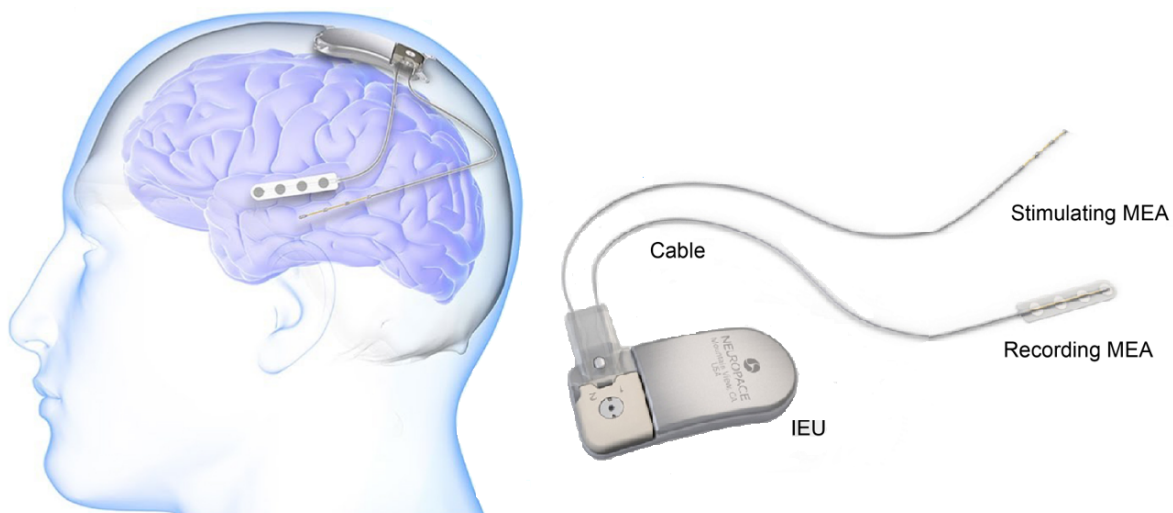


Figure 1.1: Closed-loop responsive neurostimulation system. Reprinted from [12].

These approaches range from optogenetics and gene therapy techniques [13] to cortical and retinal prosthesis [14], which uses stimulation of the retina cells to evoke neural responses to favour the visual pathway. Nevertheless, a suitable and focused restoring of the retina’s function does not necessarily imply that patients can come back to see again. The current perceptual experience of blind subjects with retinal prosthesis is still far from that of a patient with a healthy retina [15].

Visual retinal prosthesis requires the visual system’s capability downstream of transmitting optical signals on the transmitting side and elaborating them on the receiving side. These developments represent promising progress in the field of visual restorative medicine, providing hopes for blind subjects. Nevertheless, there are still tricky physical and engineering obstacles to face, some not easy to overcome. As a proof of what mentioned, Figures 1.2 and 1.3 show the simulations of the vision quality of patients with the retinal prosthesis and with a healthy retina.

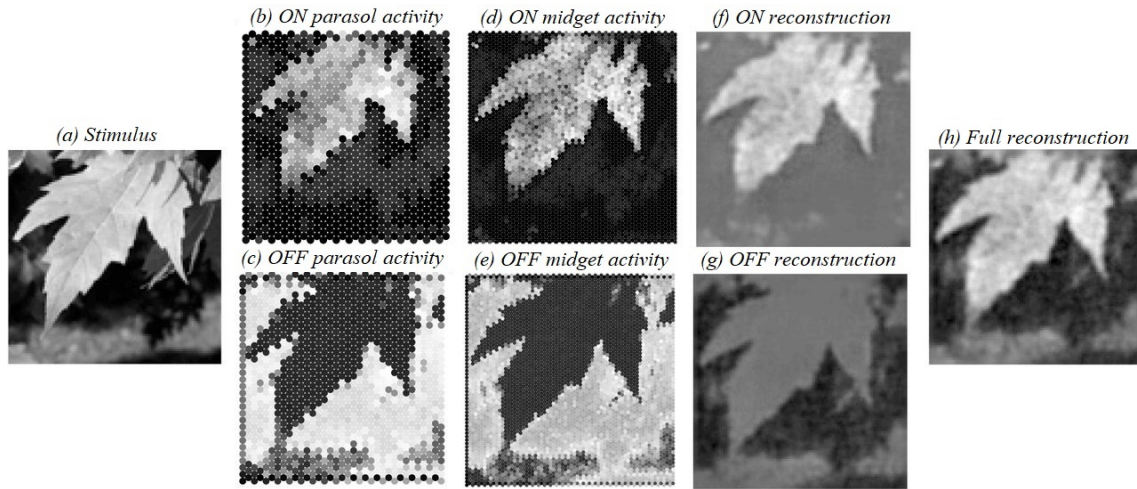


Figure 1.2: Simulation of the visual stimulus, the simulated responses of the Retinal Ganglion Cell (RGC) and the linear reconstruction in healthy retina. Reprinted from [15].

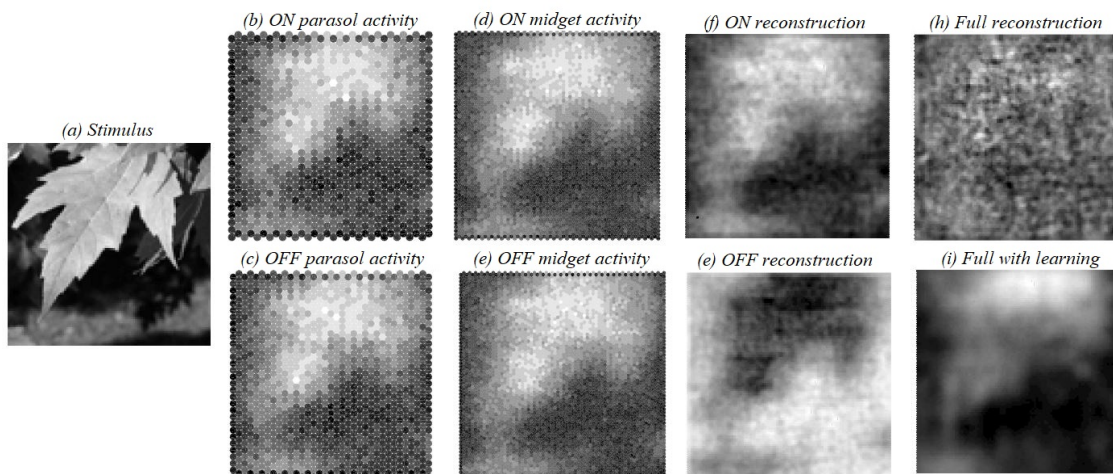


Figure 1.3: Simulation of the visual stimulus, the simulated responses and linear reconstruction with retinal prosthesis. Reprinted from [15].

1.2 Challenges in Neural Stimulation

Miniaturisation and large scale implant distribution are critical players in the next generation of neural implants. Miniaturised and free-floating implants can: i) record small signals emitted from a small population of neurons in different zones and ii) efficiently stimulate the brain with a very high spatial selectivity. Hence, Wireless Power Transfer (WPT) results in the key strategy to supply the next generation of extremely miniaturised and free-floating neural implants. The development of such type of new implants is accomplished by several challenges and critical issues, which are the following:

- **Miniaturisation.** The main physical limitation of the IMDs is the implanted electronics' size. Miniaturised implants guarantee long-term tolerability and safe surgical implantation. On the other hand, low-power and low-area design are extremely challenging with the present Complementary Metal-Oxide Semiconductor (CMOS) technology, especially regarding the analogue Integrated Circuit (IC) design. The bulkiness of capacitors is one of the main problems to face since bulky matching capacitors are required, occupying a large area.
- **Scalability and Reliability.** In order to stimulate the brain to increase spatial selectivity, multiple implants are usually needed to cover a large brain area. Therefore, high selectivity and precise calibration are necessary to ensure the single CMOS-mote's proper stimulation, not to compromise the reliability.
- **Wireless Power Transfer.** The elimination of batteries is crucial to miniaturise the implant further. Therefore, efficient WPT methods need to be adopted to supply such that CMOS chips in their operation.
- **Power Consumption.** Ultra-low-power CMOS design is essential in miniaturised and wirelessly powered implants. In particular, via WPT, only a small amount of power is achievable from the implant side. Therefore, this quantity of power has to be maximised, acting more and more on low-power designs aimed at reducing the power dissipations.
- **Data Transfer.** A large number of miniaturised, wirelessly powered and individually addressable implant means adopting an optimal downlink communication for data transfer. Performance, robustness and data rate are key elements in data transfer.
- **Misalignment and angular rotation.** The surface of the brain is not smooth: sulci and gyri make it very irregular. Therefore, the WPT needs to be optimised and well designed to maximise each implant's power transfer efficiency.
- **Safety.** WPT system needs to be carefully designed and agreed with the international guidelines and rules in terms of safety. The consumed power by the IMD may cause an increase in the temperature in the human tissues, causing irreversible damage to tissues. In the United States, the Federal Communications Commission (FCC) has set the Specific Absorption Rate (SAR) to prevent tissue heating.
- **Bio-compatible Packaging.** The packaging material has to satisfy bio-compatibility criteria to avoid any damage in the body.

1.3 Smart Neural Dust to Revert Blindness

The primary research in which this thesis takes part is developing a Smart Neural Dust to revert blindness. The whole project aims to stimulate the primary visual cortex exploiting the new concept of ultra-miniaturized, individually addressable, distributed and wirelessly powered implantable neurostimulators.

1.3.1 Master Thesis Outline

The thesis is organized as follow. In Chapter 2, the state-of-the-art of the akin implantable neural systems presents nowadays in the literature is reported.

In Chapter 3, the state-of-the-art of the WPT is explained, highlighting the need to have a stable power source. A detailed comparison between the different methods is reported with their advantages and drawbacks, focusing on an inductive link. In the same chapter, the state-of-the-art of wireless data communication among the external transmitting base station and the implanted neural device is explained. Different data communication approaches and their performances are presented. Instead, in Chapter 4, the system considerations are presented and discussed in detail. Among which, the choices of: i) the most suitable WPT method, ii) the optimal operating frequency with its trade-off, iii) the SAR limits imposed by the standards and iv) the optimal modulation technique. Goals and design specs are summarized. Afterwards, in Chapter 5, the novel RadioFrequency (RF) transmitter architecture is proposed. Theoretical considerations, steps for a proper design and, finally, simulations and laboratory implementations are described in detail. In Chapter 6 the results are discussed, analyzing the strengths and weaknesses of the present state-of-the-art. The conclusion chapter, Chapter 7, closes the work. Concrete conclusions and an ambitious perspective on future works and their possible applications are provided.

Chapter 2

Miniaturised Neural Implants: State-of-the-Art

Several wireless sub-mm implantable neural interfaces have been developed for both research purposes, monitoring, and clinical treatments [16]. One of the most therapeutic approaches requires the stimulation of neural activity. This project's idea borrows from the concept of a single wireless μ electrode stimulator known as *StimDust*, proposed and developed at UC Berkeley [17].

This Chapter presents the state-of-the-art of sub-mm neural IMDs. Generally, neural IMDs have stimulating and recording functionalities. For the following recent implantable neural systems is exploited WPT to solve the bulkiness of the batteries. Two modules are usually present: i) an external RF base station suitable for providing wireless power and data, ii) an internal implanted system liable for stimulating the target and/or for recording.

Nowadays, the main typologies of powering exploit electromagnetic waves and ultrasonic waves for data transmission and power. The μ -fabrication techniques are employed to improve the size resolution and improve Power Transfer Efficiency (PTE) and Power Delivered to the Load (PDL) values exploiting the 2-, 3-coils Inductive Power Transfer (IPT) links as described in Chapter 3. In the 3-coils IPT, an intermediate coil called resonator with a high-quality factor Q is placed at dura matter level to favour the power and data transmission.

2.1 StimDust

StimDust is an mm-sized wireless nerve stimulator powered up through UltraSound (US). It also exploits a customized US protocol to stimulate, therefore, without any presence of coils. Its system is based on an external electric transducer realized in Piezocrystal Zirconate Titanate (PZT) of the dimensions of $750 \times 750 \times 750 \mu\text{m}^3$ used for powering and for data telemetry. The wireless data communication is only to downlink [17].

The IC area is about 0.06 mm^2 , and the CMOS technology used is Taiwan Semiconductor Manufacturing Company (TSMC) $0.065 \mu\text{m}$. The final size is 6.5 mm^3 since it also contains an external capacitor used to store energy. The neural device was tested in vivo on the rat sciatic nerve. Therefore, the custom Stim IC is used to stimulate and communicate, but not to record [18].

The carrier frequency is 1.85 MHz, a compromise to: i) improve the storage of voltage, that requires a larger thickness of piezoceramic transducer and ii) decrease of high ultrasound attenuations, that occurs at higher frequencies. This system cannot be implemented in applications smaller than one mm^3 , and it can stimulate one site at a time. These are the main advantages. Figure 2.1 shows the central concept depicting the StimDust system for stimulation of the sciatic nerve of a rat.

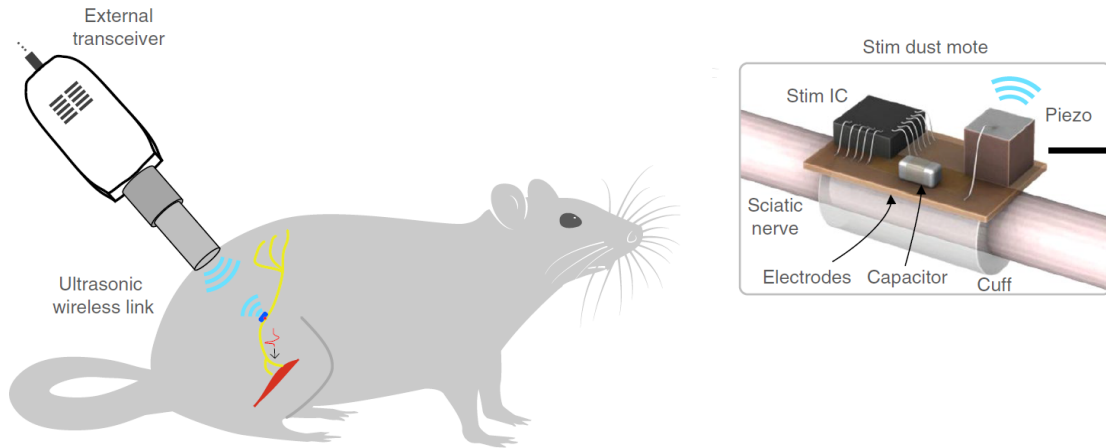


Figure 2.1: State-of-the-art of sub-mm implantable neural systems. Diagram of StimDust wireless neural stimulator system with close up view of the Stim Dust mote. Reprinted from [17].

2.2 Microbead

Microbead is a wirelessly powered miniaturized implant implemented in a 130 nm CMOS technology [19]. It exploits the 2-coils IPT link able to both record and to stimulate. A single-chip includes: i) the coil, ii) the proper circuitry for the signal processing and iii) electrodes. Each *Microbead* contains an entirely analogue circuit and four electrodes, one couple for recording and another for stimulating. Each of them is implanted into the human brain through syringes with a 22G needle, rendering the process minimally invasive. The receiving coil is a Printed Spiral Coil (PSC) of $300 \times 300 \mu\text{m}^2$ with an octagonal shape. The operating distance is 6 mm, and it is characterized by a PDL and PTE of 55.5 μW and 0.0019% respectively, at 1.18 GHz. The small declared transmission efficiency is caused by the presence of the rectifier, which reduces the system efficiency. Figure 2.2 shows the three-dimensional drawings of *Microbead* with a close-up view of the transmitting coil and electrodes in the human brain.

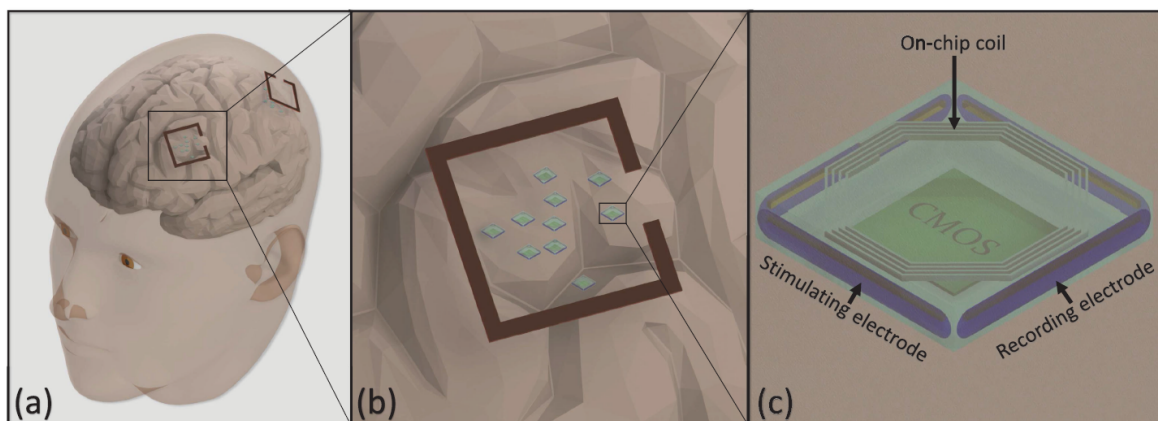


Figure 2.2: State-of-the-art of sub-mm implantable neural systems. (a) Three-dimensional drawings of *Microbead* in the human brain; (b) view of the transmitting coil; (c) the packaged *Microbead* with one couple of electrode for recording and other one for stimulating. Reprinted from [19].

2.3 ENGINI

ENGINI is the acronym of «Empowering Next Generation Implantable Neural Interface», composed by an external processor, a cranial transponder located at dura matter level, and intracortical probes [20]. Regarding wireless architecture, probes contain an integrated wireless recording system able to amplify the signal, transmit data information, and manage power.

The carrier band falls in the Industrial, Scientific and Medical (ISM) radio band around 433 MHz with a Load-Shift Keying (LSK) modulation and a data rate of 205 kbps. Their positioning is challenging since the probe electrode is strongly flexible. Therefore, robotic surgical operation and implantation mechanism are required. The same research’s team introduced an electromagnetic lens to enhanced IPT links, improving both the PTE and the covering distance. Figure 2.3 shows the ENGINI platform concept with a close-up view of the probe positioned in the human cortex.

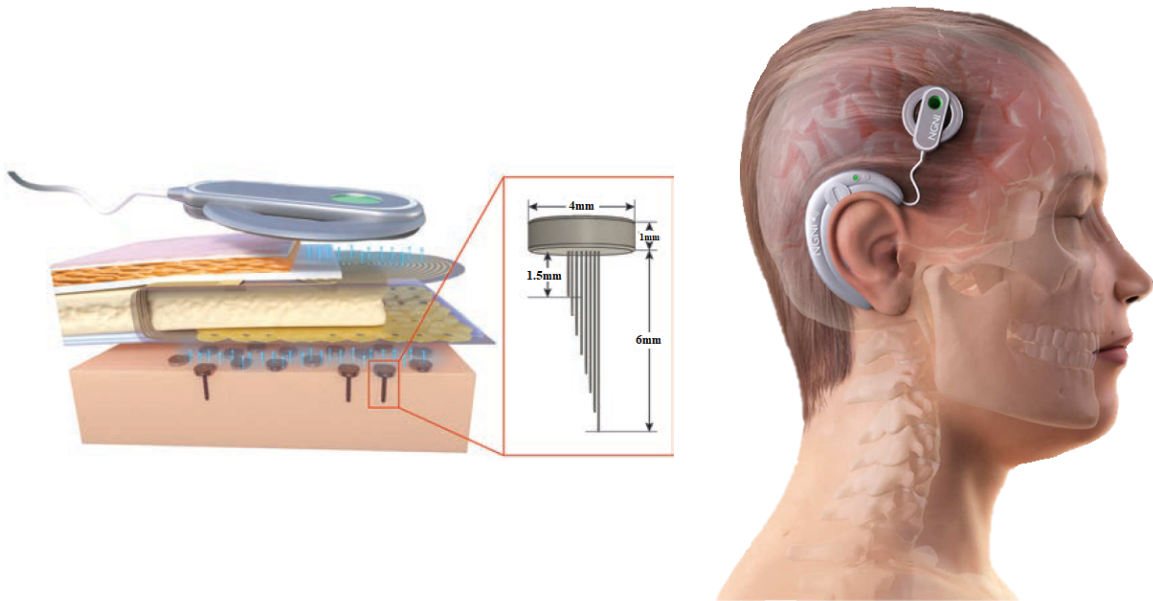


Figure 2.3: State-of-the-art of sub-mm implantable neural systems. ENGINI platform concept with IPT neural microstimulator. Close up view of the single probe with approximate dimensions. Reprinted from [20].

2.4 Neurograins

Neurograins is based on an Application Specific Integrated Circuit (ASIC) chip developed for recording or stimulating. Each microchip of the dimensions $650 \times 650 \times 250 \mu\text{m}^3$, called Neurograin, are distributed in a network containing thousand of grains that perform neural sensing, or electrical stimulation [21].

The data telemetry is bi-directionally synchronized, exploiting uplink and downlink operating with Time Division Multiple Access (TDMA) communication network at 1 GHz IPT link. The uplink data transmission can achieve up to 10 Mbps [22].

In Neurograins, a thick coil in copper (Cu) realized in CMOS technology $0.065 \mu\text{m}$ by TSMC Foundry is present. The systems exploit the IPT with a 3-coils configuration of which its receiver is a PSC of $500 \times 500 \mu\text{m}^2$ operating at a distance of 8 mm between transmitting coil and receiving one. The operating frequency is 915 MHz. Neurograins is characterized by a PDL and PTE of $235 \mu\text{W}$ and 0.047%, respectively. This neural IMD is used for recording and stimulating, and, recently, it is tested

in vitro on animals.

Figure 2.4 shows the central concept of a transcutaneous RF transmission of power and data exploiting the WPT via IPT.

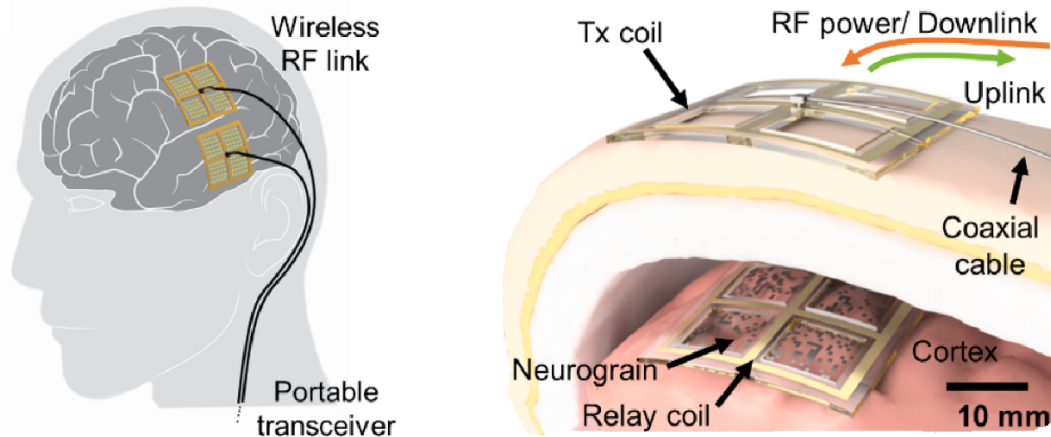


Figure 2.4: State-of-the-art of sub-mm implantable neural systems. Neurograins platform concept with size scale of the chip. Reprinted from [21].

2.5 Comparison with Akin Projects

Numerous sub-mm neural IMDs have been developed, targeted for clinical and research purposes and equipped with neural recording and/or stimulating functionalities.

Table 2.1 summarises the previous described state-of-the-art sub-mm implantable neural systems with their performances, characteristics and functionalities. Others akin projects are not reported in Table 2.1 and not described in details. Among the others: Neural Dust [4], Michigan/ETH [23], Stanford [24] and ENIAC [25].

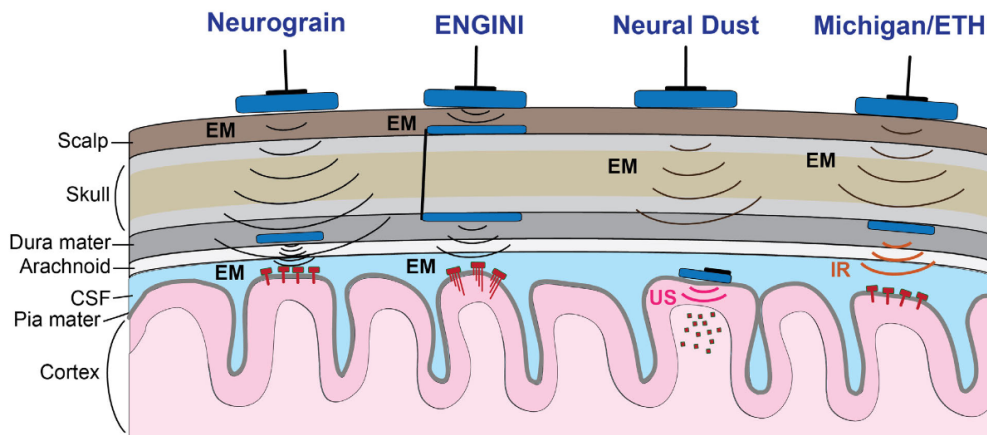


Figure 2.5: State-of-the-art of various powering schemes of sub-mm implantable neural systems. Reprinted from [16].

		ENGINE [20]	Neurograins [21]	StimDust [17]	Microbead [19]
General	Brain Activity	Recording	Recording or Stimulation	Stimulation	Recording and Stimulation
	Neural Implant Volume (mm ³)	12.56	0.00675	6.5	0.009
	IC Area (mm ²)	2.1	0.42	0.06	NA
	Size (μm ³)	650×650×250	3500×3500×NA	750×750×750	340×330×80
Extra Components Implanted	Number of Channels	Cranial Transponder 8	Relay Coil 1	Piezocrystal 1	None 1
	CMOS Technology (μm)	0.35 AMS AG	TSMC 0.065 MS/RF LP	TSMC 0.065 LPCMOS	0.13 RF
	Power Supply (V)	1.5	0.6-1	2.5	1
	Total Power Consumption (mV)	0.092	0.03	0.035	NA
Powering	Number of Chip Testing	10-100	1000	1	10
	Scheme	-	in vivo, in vitro	in vivo, in vitro	in vivo
	Frequency (Hz)	EM 433M	EM 915M	US 1.85M	EM 1.18G
	Rx Coil Size (mm ²)	12.25	0.25	-	0.09
Communication Uplink/Downlink	Distance (mm)	8	12	21.5	4.6
	Number of Coils	3-coils	3-coils	-	2-coils
	Number of Turns Tx/Rx	NA	1/3	-	1/7
	Number of Turns Resonator	NA	NA	-	-
	Trace Width Tx/Rx (mm)	NA	NA	-	-
	Trace Thickness Tx/Rx (μm)	NA	NA	-	3/0.007
	Diameter Tx/Rx (mm)	-/0.0025	-/0.0034	-	35.6/4
	Material Tx/Rx	-/3.5	0.5/-	-	10/
	PDL (μW)	Au	-/Cu	-	Cu/Al
		NA	0.095 ÷ 0.235	-	55.5
Recording	Modulation	-/LSK	ASK-PWM/ BPSK (TDMA)	NA	FDMA
	Frequency (Hz)	-/433	1G/1G	2k	1.25G/1.5G
Stimulation	Data rate (bps)	-/205k	1M/10M	NA	NA
	Input Noise (μV)	1.8	2.2	-	NA
Stimulation	ADC Resolution (bits)	11	8	-	NA
	Max Current (μA)	-	25	400	46
Notes		-	-	-	Current
		-	-	-	Antenna integrated on chip

Table 2.1: Comparison of state-of-the-art sub-mm free-floating neural IMDs. Reprinted from [16].

Chapter 3

Wireless Power Transfer and Data Communication in Neural Implants

The power source is the key factor in IMDs, as well as in neural implants. Different approaches have been exploited, among the others:

- Implanted batteries, generally in Zn-air and Li-ion compositions.
- Body energy harvesters.
- Wireless power transfer.

There are several advantages as many as shortcomings for the presented approaches. Therefore, every situation has to be evaluated to offer the optimal solution, which is dictated by the appropriate balance between trade-off and constrains imposed by the intended-use.

As first approach proposed, the batteries have higher energy capacity regarding the ambient energy harvesters method but suffer from bulkiness problem in the implanted system. The battery capacities are still limited. Their reduced endurance requires steps of follow-up surgery for the replacement of the battery. Therefore, to sum up, implanted batteries are excluded due to their bulky size, cost, and lifetime constrains [26].

The second proposed method is energy harvesting, in which the energy comes from external sources. It converts the different form of available energy present in nature into electrical power after to be captured and stored for small, wireless autonomous devices. This approach provides a tiny quantity of energy for low-power electronics, and the instantaneously available source defines its efficiency. For the sake of simplicity, different kinds of body energy harvesters can be pressure variations, vibrations, and temperature. Therefore, according to these instances, possible implementations are: piezoelectric [27], light [28], infrared light [29] and thermal [30].

The energy harvesting method is not commonly exploited due to the low availability of the sources and the reduced space which implants require.

3.1 Wireless Power Transfer

WPT has several advantages regarding other power sources since it is a method for delivering energy, not an energy source itself, such as batteries and ambient energy harvesters. Therefore, WPT provides a higher available power budget. The main aspects of WPT are the transmission distance, the supplied power and the efficiency of the delivered power. WPT requires a Tx outside the body and an Rx inside the body. The transmitting side transforms the electrical energy into a carrier wave. On the other hand, the receiving side exploits the carrier wave converting it back into electrical energy.

Several WPT methods are compared: radio-frequency radiation in the far-field [31], mid-field [32], near-field [33], Inductive Power Transfer (IPT) [34], Capacitive Power Transfer (CPT) [35] and Acoustic Power Transfer (APT) [36].

The distinction between RF radiation in the far-field with respect to the near-field is defined by the distance between the external transmitting unit and the implanted receiving one. The parameter that distinguishes the two categories is the Fraunhofer distance d , defined in (3.1):

$$d = \frac{2D^2}{\lambda} \quad (3.1)$$

where D is the diameter of the Tx, and λ is the wavelength of the radio-wave. If the distance between the coils is smaller than the Fraunhofer distance d , the magnetic coupling ensures a more efficient system. The control on the distance has to be carried out carefully since, in far-field, the influences and the formulas would require a much more complex numerical model.

Figure 3.1 shows a qualitative three-dimensional histogram, which aims to compare the methodologies for WPT [37]. The graph is described in function of penetration depth on x -axis, receiver lateral size on y -axis and link efficiency placed on z -axis. The reported link efficiency is the ratio of the transmitted power and the PDL. The location and the area of every single coloured box represent the optimal trade-off between penetration depth, link efficiency and penetration depth.

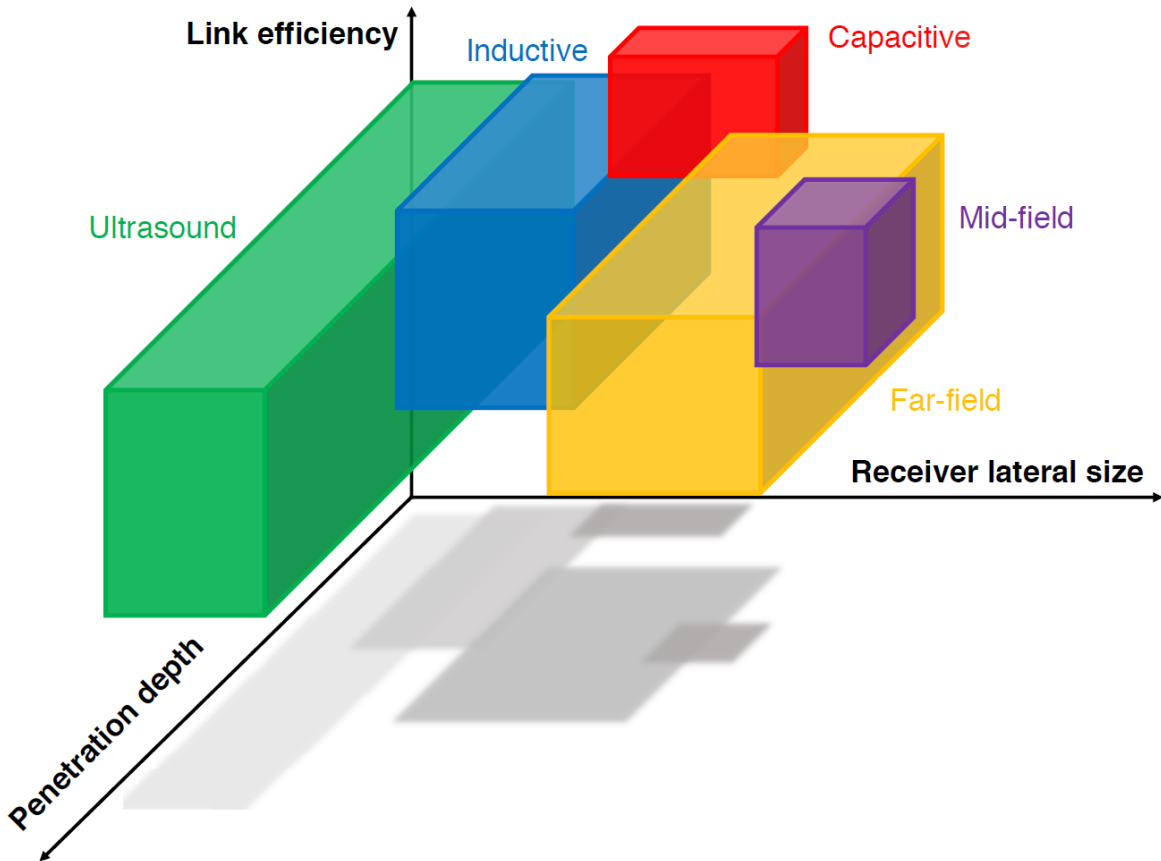


Figure 3.1: Qualitative comparison described through three-dimensional histogram for different methods for WPT. Reprinted from [37].

This comparison has highlighted that for implant in the centimetre scale, such as an implantable

pacemaker, the most appropriate WPT are the RF radiation in the far-field and mid-field. These methods guarantee the best performance at large distances between Tx and Rx. Instead, miniaturized implants, such as neural stimulator, IPT, CPT and APT are the most proper. Figure 3.2 is a graphical representation of these three methods, reporting the qualitative optimal distance in the proper working condition for the neural stimulator qualitatively.

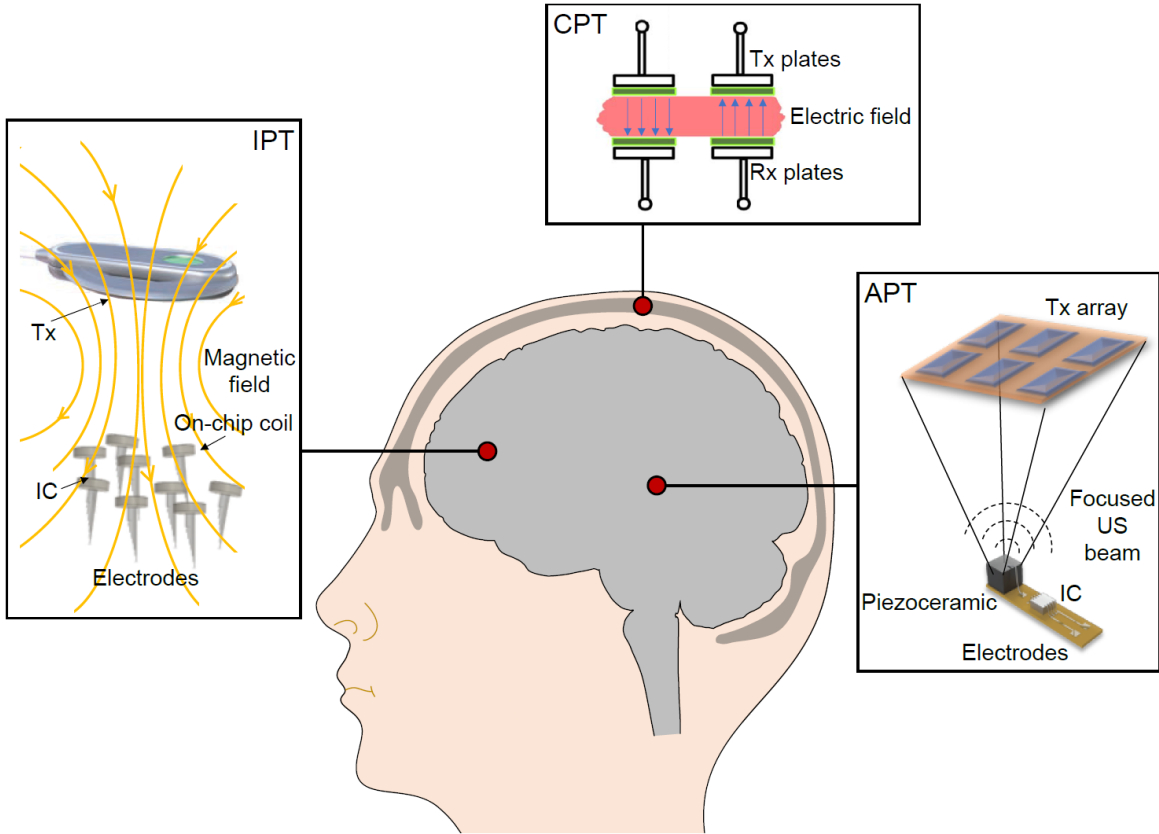


Figure 3.2: Graphical representation of IPT, CPT and APT with the qualitative optimal distances in the proper working condition. Reprinted from [37].

3.1.1 Far-field Radiation

The far-field radiation has wavelengths comparable to the dimensions of the implantable system. Therefore, the required frequency values would be of the order of magnitude of GHz, up to THz to reach sizes of μm . The latter values would not be possible in biomedical applications since the absorption curve in human tissues grows exponentially with the increase of frequency, causing a substantial reduction in efficiency.

3.1.2 Acoustic Power Transfer

The APT method is commonly used for IMDs because the acoustic waves are much less attenuated through body tissue with respect to the radio-frequency ones. Thus, this WPT allows having long-distance between Tx and Rx. Therefore, it will enable high penetration depth. Another advantage of the APT method is the limit of power density, which is two orders of magnitude lower than RF

power density one. Figure 3.3 shows the equivalent circuit model for a generic APT link. The acoustic wave is generated by the external piezoelectric transducer supplied by the external energy source on the transmitting side. On the receiving side, the receiving piezoelectric causes a voltage difference proportional to the related mechanical deformation. The potential difference is delivered to the IC.

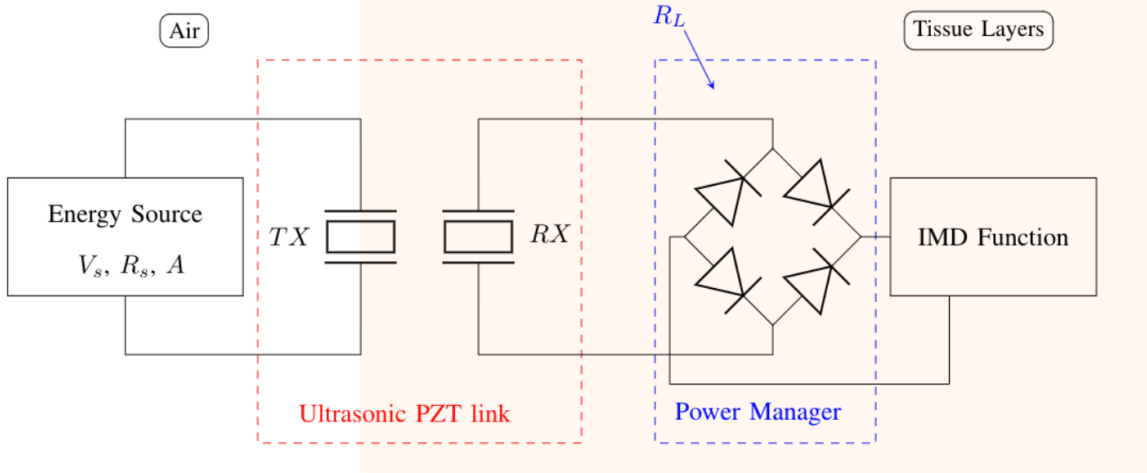


Figure 3.3: Equivalent circuit model for a generic ultrasonic wireless link. Reprinted from [37].

Although APT has numerous advantages, it suffers from many limitations. The main issues are: i) beamforming problem, ii) high attenuation, iii) low selective stimulation. The presence of reflections causes the high attenuation of the beam intensity [38] and by the highest absorption loss of the skull tissues. The tissue absorption is described by Lambert-Beer defined in (3.2):

$$I_d = I_0 e^{-2\alpha d} \quad (3.2)$$

where I_0 is the initial beam intensity, I_d is the beam intensity after the tissue's thickness d , and α is the absorption coefficient.

Finally, the low selective and precise stimulation - caused by effects of linear and angular misalignment [39] - makes particularly difficult the beam's focus. Therefore, the physical separation in multi-site stimulation applications is a substantial limitation.

In neural applications, APT needs at least one piezoelectric receiver to generate a focused UltraSound (US) beam. The piezoelectric Rx is an off-chip component which needs to be bonded to IC, leading to an increase in this latter's implant volume (Figure 3.2). An instance of implantable neural interface with the APT method is the StimDust described in section 2.1.

3.1.3 Capacitive Power Transfer

The CPT method is a low-cost technology, less affected by linear and angular misalignment and high integration capability. This approach depends on the plates' area A , the dielectric material placed between the two plates ϵ , and the distance between the latter d . A proper CPT design's key parameters are the distance of the two parallel plates and their overlapping area. CPT results more efficient than IPT and less susceptible to interference, allowing high data rate communication.

Figure 3.4 shows the equivalent circuit model for a generic CPT link.

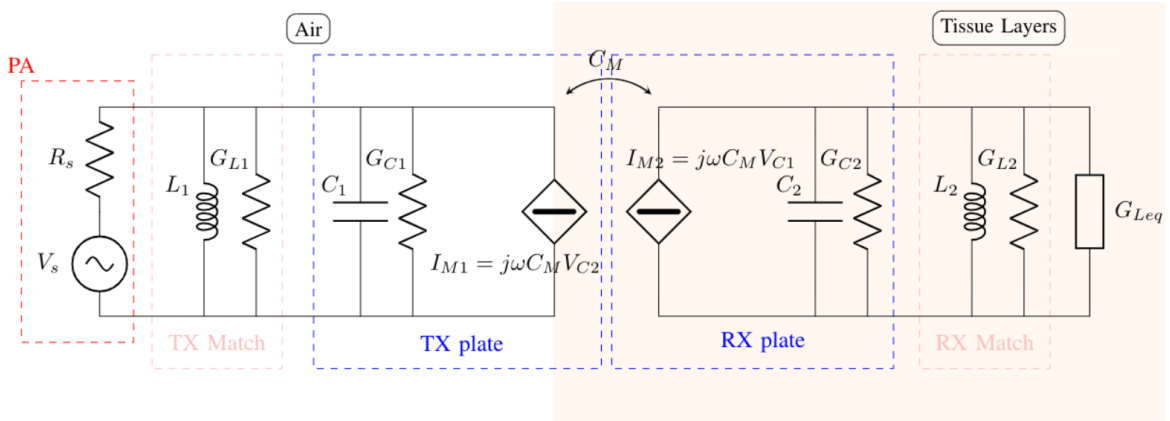


Figure 3.4: Equivalent circuit model for a generic capacitive coupling wireless link. Reprinted from [37].

C_1 and C_2 are the two self-capacitors; G_{C1} and G_{C2} are the physical losses of the capacitive plates; L_1 and L_2 are the inductive resonance networks with their losses G_{L1} and G_{L2} . Finally, C_M is the mutual capacitance represented by two voltage-controlled current sources I_{M1} and I_{M2} defined in (3.3) as:

$$I_{M1} = j\omega C_M V_{C2} \quad I_{M2} = j\omega C_M V_{C1} \quad (3.3)$$

where, V_C is the capacitance-voltage and ω is the operating frequency.

CPT has a substantial limitation in terms of application distance since it can be exploited for only short-range distances, up to a few millimetres, for both data telemetry and power transfer. In fact, this approach is exploited sub-skin in literature, such as 5 mm [40]. In neural applications, CPT presents two couples of parallel plates: one for transmitting and one for receiving, separated by the human tissue (Figure 3.2).

3.1.4 Inductive Power Transfer

WPT via IPT emerged as the most appropriate method towards multiple miniaturised chips (i.e. lateral size in the mm or sub-mm range) with a medium penetration depth (i.e. 10 ÷ 20 mm). In neural applications, IPT needs one Tx coil and one Rx coil, working with magnetic coupling (Figure 3.2). It is a useful method for large amounts of power (i.e. a few hundreds of mW). Its performance depends on the operating frequency due to the human tissue's absorption, which occurs strongly at high frequency.

Figure 3.5 shows the lumped circuit model for a generic IPT link. L is the coil's self-inductance value; R_S and R_P are the parasitic resistances; C_P is the parasitic capacitance. The parasitic effects are related to the geometries of the fabricated coils and to physical parameters of the tissues, such as conductivity σ and relative permittivity ϵ_r . Finally, C_2 and C_{S1} are the matching elements to maximise PTE and ensure the same frequency on the two sides. M_{12} is the mutual inductance between the two coils, related to their geometry and distance. For these reasons, design, geometrical optimisations and analysis of coils are often the subjects of study.

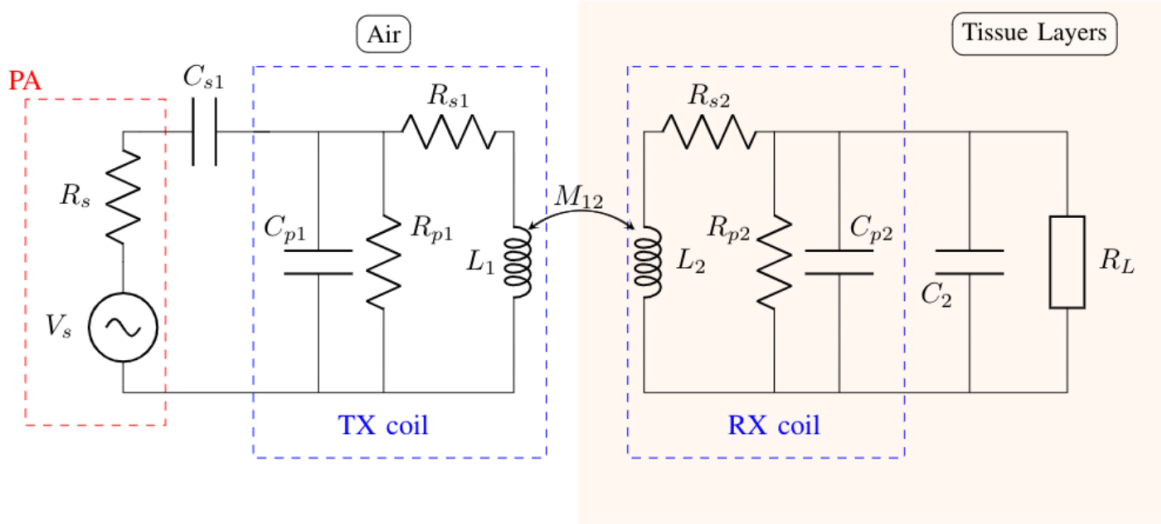


Figure 3.5: Equivalent circuit model for a generic inductive coupling. Reprinted from [37].

From the equivalent circuit model, the equivalent impedance Z is extracted as (3.4):

$$Z = \frac{R_S + j\omega L}{(R_S + j\omega L)(G_P + j\omega C) + 1} \quad (3.4)$$

The equivalent impedance Z is needed to calculate the quality factor Q , as $Q = \Im(Z) / \Re(Z)$. The quality factor represents the coil's capability to induce a strong or weak magnetic field \mathcal{H} , therefore the ability to transfer energy. Finally, PTE (η) and PDL (P_L) are two key parameters in IPT link defined by (3.5) and (3.6) [41], expressed in percent and mW, respectively:

$$\eta = \frac{k_{12}^2 Q_1 Q_{2L}}{1 + k_{12}^2 Q_1 Q_{2L}} \cdot \frac{Q_{2L}}{Q_L} \quad (3.5)$$

$$P_L = \frac{V_s^2}{2R_1} \cdot \frac{k_{12}^2 Q_1 Q_{2L}}{(1 + k_{12}^2 Q_1 Q_{2L})^2} \cdot \frac{Q_{2L}}{Q_L} \quad (3.6)$$

with,

$$k_{12} = \frac{M_{12}}{\sqrt{L_1 L_2}} \quad Q_L = \frac{R_L}{\omega L_2} \quad Q_{2L} = \frac{Q_2 Q_L}{Q_2 + Q_L} \quad (3.7)$$

where k_{12} is the coupling coefficient, Q_L is the load quality factor, and R_L is the load resistance. High PTE favours the reduction of heat dissipation in the coils and the tissue exposure to the magnetic field \mathcal{H} .

Multiple Coils Configurations

The most straightforward IPT system requires 2-coils [42], characterized by an only pair of coils, so one only interface. More recently, new implementations with 3-coils and 4-coils IPT have been implemented [43].

Figure 3.6 reports the lumped circuit model of a conventional 3-coils IPT link. The 3-coils configuration is characterized by the insertion of a resonator coil L_2 placed between the Tx and Rx.

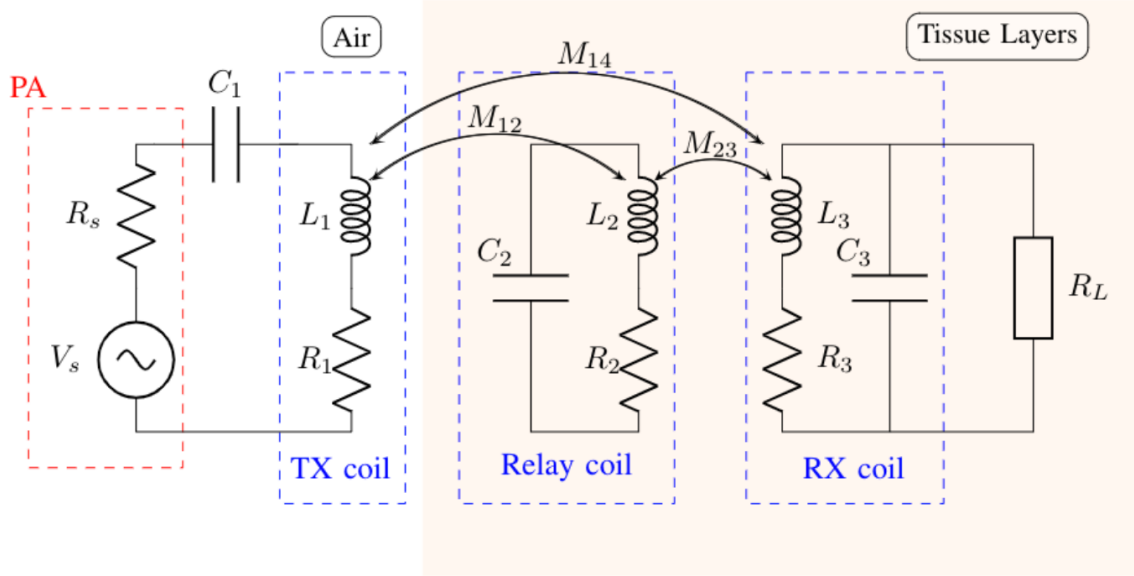


Figure 3.6: Lumped circuit models of a conventional 3-coils IPT links. Reprinted from [37].

IPT with multiple coils shows PTE increment, even at sizeable operating distance d . Atluri and Ghovanloo proposed the use of multiple coils in 2005. M. Ghovanloo and collaborators compared IPT links with 2-, 3- and 4-coils [44]. They proposed a design and optimisation procedure to improve both PTE and PDL in multiple coils configurations, as the best solution to overcome the misalignment.

Figure 3.7 reports the three-dimensional simulations of PTE and PDL realized in function of the coupling distance between the two reference coils d , and the coupling coefficient k . In particular, d_{12} and k_{23} for the 3-coils IPT link, and d_{23} and k_{12} for the 4-coils IPT link. Generalizing with x and y subscripts, k_{xy} is defined in (3.8):

$$k_{xy} = \frac{M_{xy}}{\sqrt{L_x L_y}} \quad (3.8)$$

where M_{xy} is the mutual inductance and L_x and L_y are the inductances of the coils.

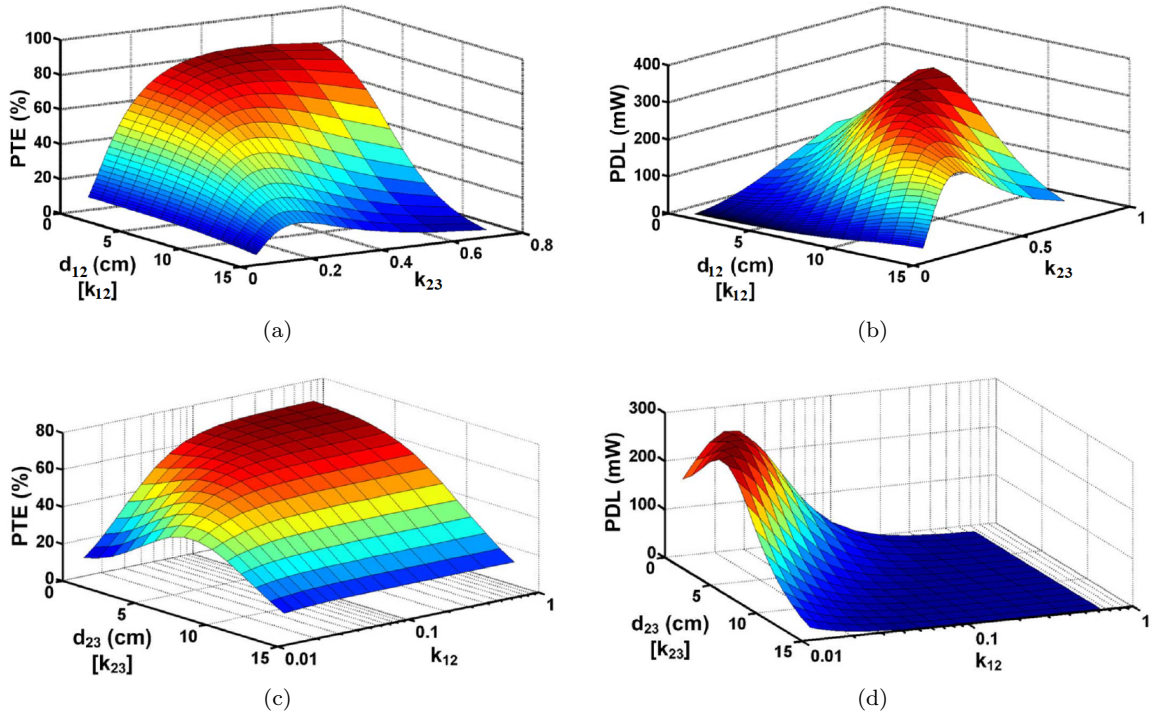


Figure 3.7: Three-dimensional simulations of PTE and PDL in different IPT configurations in function of the coupling distance d_{xy} and coupling coefficient k_{xy} . (a) PTE and (b) PDL for 3-coils IPT link; (c) PTE and (d) PDL for 4-coils IPT link. Reprinted from [44].

In the 3-coils configuration, from the comparison of Figure 3.7-a and 3.7-b emerges that a simultaneous high PTE as well as high PDL is possible to obtain with proper design choices of the coil and their geometries. On the other hand, from the comparison of Figure 3.7-c and 3.7-d emerges that high transmission efficiency and delivered power areas do not ever overlap in the 4-coils configuration, imposing the presence of a trade-off between PTE and PDL. Therefore, M. Ghovanloo and collaborators demonstrated that 4-coils IPT links do not achieve a high delivered power, despite a high transmission efficiency. The power delivered to the load cannot surpass a safe voltage limit V_S since a high value causes safety issues in biomedical applications. Moreover, they proved that a 3-coils configuration diminishes the SAR with respect to 2-coils one [45].

Instead, Figure 3.8 analyzes the behaviours of the transmission efficiency and delivered power in function of the coupling distance d_{23} in 2-, 3-, and 4-coils configuration. The graph highlights that wireless power transfer via IPT can be exploited for medium penetration depth, ensuring high delivered power for 2- and 3-coils IPT links.

More precisely, the 2-coils configuration allows to obtain: i) higher delivered power than one in 4-coils configuration at the expense of a lower transmission efficiency, and ii) the highest transmission efficiency across link having both LC tanks tuned at the same resonance frequency f_0 . The resonance frequency f_0 is defined in (3.9) as:

$$f_0 = \frac{1}{2\pi\sqrt{L_1 C_1}} = \frac{1}{2\pi\sqrt{L_2 C_2}} \quad (3.9)$$

Moreover, the trend emerges that, as coupling distance increases, PTE decreases regardless of the configuration. The 4-coils IPT is more appropriate for short penetration depth (i.e. 2-3 mm).

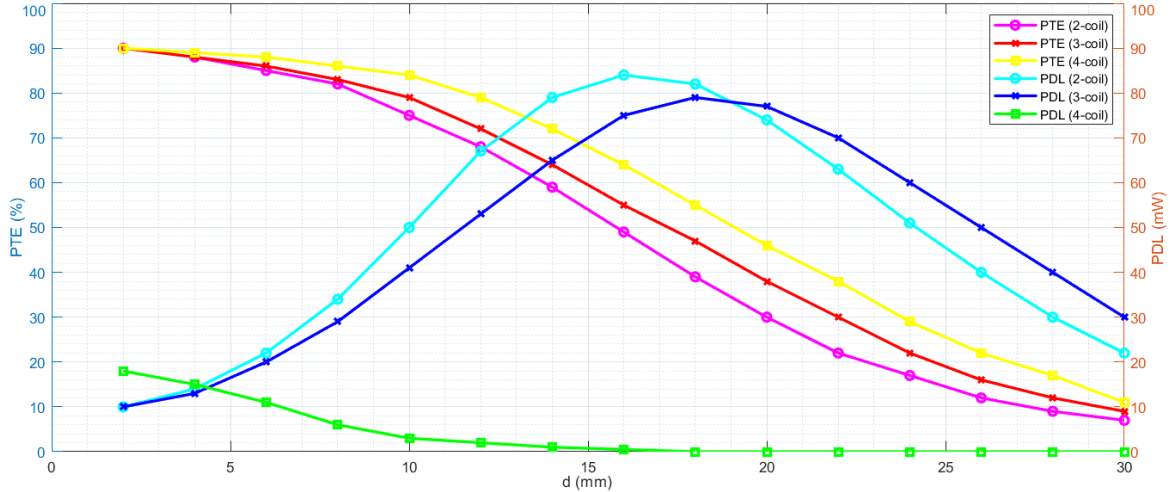


Figure 3.8: Comparison between the transfer power efficiency (PTE) and the delivered power (PDL) as a function of d_{23} for 2-, 3-, and 4-coils IPT method. Values extracted from [44].

To sum up, WPT via IPT in 3-coils configuration shows the best performance in PTE, tolerance to misalignment and SAR-constrained PDL. The efficiency of the driver is negligible for 3-coils IPT systems. The main advantages are the following:

- Additional degree of freedom provided by d_{23} . It allows optimizing the quality factor Q , favouring a better immunity to the misalignment's problem.
- The highest value of PTE simultaneously to the maximum value of PDL, exploiting a proper choice of geometries of the coil values.
- Better PTE at more considerable distances.
- Absence of inefficiency between the primary coil and driver.

Therefore, the 3-coils configuration is typically used for neurostimulation since it shows advantages for large distances and the receiver's small size.

On the other hand, the WPT via IPT in 4-coils configuration presents a high PTE as high as 3-coils IPT systems, also ensured at large distances. 4-coils configuration suffers from some issues. Among which: i) very difficult to reach high PDL, ii) non-overlap of the PDL and PTE area, iii) safety issues in medical applications when a high delivered power is required. Therefore, the involved voltages are required lower than a strict safe voltage limit V_S .

3.2 Wireless Data Transmission

Data transfer is another key element in RF transmitters' design for several distributed and miniaturised implants requiring large data transmission. Wireless data transmission is used to control an implantable neural system. In the literature, different data communication methods are proposed. The best candidate depends on the required data rate, design constraints, distance, size constraints and power budget. Other factors related to the application and the medical intended-use are also essential to be considered. As for power, data are transferred from an external transmitting base station to the neural IMD.

Data communication requires to be designed, ensuring strong robustness against interference, thus

maintaining an optimal BandWidth (BW). The suitable data telemetry choice is linked to key aspects. Some of these considerations about data telemetry are:

- **Carrier Frequency.** Operating frequency depends on medical intended-use, system architecture and application. An increase in carrier frequency maximises the BW, but at the same time, the SAR in the human tissue, that causes an increase in heat dissipation. The choice of carrier frequency has to respect the FCC to prevent safety issues and to reduce interference.
- **Data Rate.** Neural applications involving many free-standing and individually addressable implanted chips usually require a high data rate (i.e. up to tens of Mbps) [46]. Nevertheless, the high data rate is not always possible to reach for downlink communication due to the strong limitations in terms of reliability and robustness.
- **Robustness.** Some approaches ensure a high data rate at the expense of high susceptibility to noise and artefacts. Interference may compromise transmitted data causing errors in transmission with severe consequences for patients, leading to increased Bit Error Rate (BER).
- **Area.** The area is a key parameter for neural applications. Some demodulation circuit placed in the implanted device may occupy a not available area due to their complex circuitry or bulkiness. The demodulator has to be low-power for IMDs, and with simple and not bulky circuitry. Therefore, the area has a strong influence on the choice of data telemetry.
- **Maximum Transmitted Power.** The transmitted power, expressed in Joules per bit (J/bit), has to be maximised to guarantee enough supply to the implanted system.

Single-carrier data telemetry is beneficial in terms of robustness of coupling, ensuring a more reliable data transfer. The two branches are downlink and uplink communication. Wireless data transmission for downlink communication means from the external base station to the neural implanted system. On the other hand, for uplink communication, a carrier in the implantable system is generated to transmit data out of the body. Generally, the downlink data rate in neural applications is lower than the uplink data rate, as in [47]:

«Tens of megabits per second uplink might be essential for neural recording with a large number of channels, where the downlink data rate requirement is considerably lower. In contrast, tens of megabits per second in downlink is required for neural stimulation applications, such as artificial vision in the form of retinal implants with a high number of stimulating channels that need to be refreshed at 30 Hz, or more.»

[Byunghun and Ghovanloo, «*An overview of data telemetry in inductively powered implantable biomedical devices*», IEEE Communications Magazine, 2019]

Several modulation techniques for RF data transmission have been proposed over the last years. Among other, Amplitude-Shift Keying (ASK), On-Off Keying (OOK), Frequency-Shift Keying (FSK), Phase-Shift Keying (PSK) and Pulse Position Modulation (PPM). Possible data telemetry methods will be now presented, analyzing their strengths and weaknesses.

3.2.1 Amplitude-Shift Keying

Amplitude-shift keying is one of the most popular modulation schemes. The carrier amplitude is shifted between "low" and "high" values in function of the digital data in the input. Therefore, the amplitude of the powering signal is modulated: lower amplitude usually means bit "zero" while high amplitude means bit "one" [48]. The key parameter in ASK modulation is the Modulation Index (MI), which considers the amplitude difference between "high" and "low" logical states [49]. MI is defined as in (3.10):

$$MI = \frac{V_{max} - V_{min}}{V_{max} + V_{min}} \quad (3.10)$$

where V_{max} and V_{min} are respectively the peak amplitude of the voltages for the logical "high" and "low" states. Indirectly, MI influences the BER and, therefore, its reliability. On the one side, high MI means a big difference between the two voltages $V_{max} - V_{min}$ and, therefore, low BER, since detection between logical "high" and "low" states is simplified. ASK modulation is one of the most straightforward modulation techniques in complexity, characterized by a simple circuitry for both modulation and demodulation. Therefore, it is advantageous in terms of both area and power dissipation. Nevertheless, it suffers from poor synchronization between data and clock signals and a high sensitivity to noise and inductive coupling variations. Figure 3.9-a shows the typical waveform of the ASK.

3.2.2 On-Off Keying

One of the most straightforward implementations of ASK is the on-off keying. In particular, OOK modulation is performed for $MI = 1$, and it is commonly used for Continuous Wave (CW) operation in the ISM bands [50]. This modulation technique describes the presence or absence of a carrier wave signal following the input bits. Therefore, no carrier is transmitted when the input is "zero". For this reason, an oscillator characterised by fast switching speeds is required, making it very sensitive to noise [51]. Figure 3.9-b shows the typical waveform of the OOK.

Data Encoding: Hints

In the case of miniaturised implant, the energy storing elements are significantly minimised. As a consequence, if the signal is turned off, the chip is no more powered. Therefore, a sophisticated OOK communication protocol needs to be adopted, controlling the maximum number of subsequent "low" logical transmitted data to maintain the transistor in their normal working condition. The basic idea requires an information code level aimed at reducing commutations. In this way, the switching activity results lower than the initial situation, favouring the transmission of "one" and maintaining a sufficient supply level to power up the IMD. Some decoding and encoding techniques require one or more extra control bits. The latter are not sometimes tolerated due to: i) the requirement of hardware changes and ii) incompatibility with standard bus interfaces. For instance, an application of encoding technique is the *Bus Invert*. The algorithm checks the Hamming distance between the two consecutive data [52]. The Hamming distance represents the number of bits switching from one state to another. Suppose two consecutive data differ by a greater or equal number of bits equal to $N_{BIT}/2$. In that case, the algorithm sends the inverted data, followed by an additional control bit (INV), generally placed in the Most Significant Bit (MSB) position. By convention, $INV = 0$ the bus is equal to the original data. On the other hand, the bus is the inverted data when $INV = 1$ [53]. The bus invert commutations depend on the variations, which take place between one datum and the next one. The disadvantage is the encoding redundancy, leading to an incompatibility with some systems. Table 3.1 reports an instance of bus invert encoding, highlighting how this technique can drastically reduce the transitions.

Binary Encoding		Bus Invert Encoding		
Datum	$d_{Hamming}$	Datum	INV	$d_{Hamming}$
00101010	-	00101010	0	-
00111011	2	00111011	0	2
11010100	7	00101011	1	1
11110100	1	00001011	1	1
00001101	6	00001101	0	2
01110110	6	10001001	1	2
00010001	5	00010001	0	3
10000100	4	10000100	0	4
31 transitions		19 transitions		

Table 3.1: Bus Invert coding application. Reprinted from [52].

3.2.3 Frequency-Shift Keying

Frequency-shift keying is a modulation technique where the carrier frequency is modulated following the digital input signal. Therefore, the amplitude remains constant, while the frequency varies, embedding the information. FSK is rarely used for digital modulation systems at high performance due to its lower spectral efficiency. A large BW characterizes it, but it becomes a problem with high- Q coils. Finally, its implementation requires a Power Amplifier (PA) with high power efficiency on the transmitting side and more complex and power-hungry circuitry on the receiving one. FSK limits the data rate since the latter is limited by the lowest frequency of the modulation technique. Figure 3.9-c shows the typical waveform of the FSK.

3.2.4 Phase-Shift Keying

Phase-shift keying is another common modulation technique where carrier phase information is modulated to transmit the digital input signal. Therefore, an advance or delay of the carrier phase is exploited. It has better performance than FSK and ASK, at the expense of a more complex signal detection [54]. In PSK: i) the bit error rate is lower than ASK for a given signal-to-noise ratio [55], ii) susceptibility to noise is insufficient with respect to ASK and, iii) a good synchronization in terms of frequency and phase is required at the expense of a more complexity of transmitter and receiving's circuits [56]. Figure 3.9-d shows the typical waveform of the PSK.

3.2.5 Pulse Modulation Technique

Pulse position modulation is an impulsive modulation technique where the information is encoded by: i) its information content and ii) the position of the pulse with duration τ within the sampling period. In other words, PPM is a sort of phase modulation for the pulse with constant amplitude and width. PPM is employed to solve the poor synchronization caused by the ASK modulation and recover the clock. An implementation that mixes the previous method is the Pulse-Width Modulated coded ASK (PWM-ASK) [57], able to improve BER and SNR. PWM-ASK is a power-efficient and robust scheme. Although it ensures a better sensitivity, it suffers from a low data rate because PPM and PWM-ASK require more time to represent each data bit with respect to the ASK implementation. Figure 3.9-e shows the typical waveform of the PWM-ASK.

To conclude, a comparison of the previously cited modulation technique is reported. Figure 3.9 shows graphically the exemplar waveforms. Instead, Table 3.2 highlights the main parameters of the data telemetry methods.

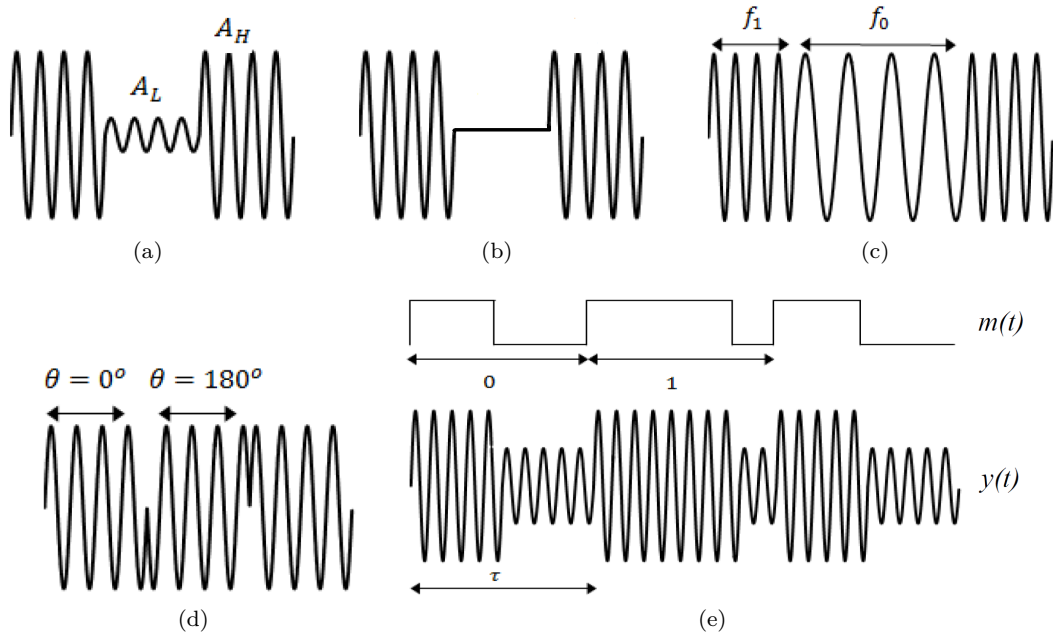


Figure 3.9: Graphical digital modulation schemes. (a) ASK; (b) OOK; (c) FSK; (d) PSK; (e) PWM-ASK. Reprinted from [51].

Modulation	ASK [58]	OOK [50]	FSK [59]	PSK [54]	PWM-ASK [57]
Distance (mm)	-	35	10	-	10
Power Carrier (MHz)	5	13.56	5/10	2	5
Data Carrier (MHz)	5	13.56	5/10	20	5
Data Rate (Mbps)	0.5	6.78	2.5	2	0.1
Tx/Rx Power (pJ/bit)	-/34	9.5/-	-/152	-	-
Technology (mm)	0.18	0.065	1.5	0.18	-
Tx/Rx Area (mm ²)	-/0.001	0.92	-/0.29	-	-
Supply Voltage (V)	1.8	1.2	5	1.8	5
Bit Error Rate	10 ⁻⁴	9.9x10 ⁻⁸	10 ⁻⁵	2x10 ⁻⁷	10 ⁻⁴

Table 3.2: State-of-the-art of data telemetry methods for IMD applications. Reprinted from [47].

Chapter 4

System Concept: Considerations

The experimental work of the present thesis has been carried out at the Integrated Circuit Laboratory (ICLAB) at École polytechnique fédérale de Lausanne (EPFL) in Neuchâtel, Switzerland. This master thesis aims to present a novel external transmitting base station for power transfer and downlink data communication toward multiple, miniaturised, and wirelessly-powered neural implant, as Neural Dust, for reverting blindness. More precisely, it is demonstrated the possibility to design and realise an RF transmitter able to operate at ISM band at 433.92 MHz. A new Simultaneous Wireless Information and Power Transfer (SWIPT) system is proposed here to efficiently modulate the carrier, exploiting an ASK modulation able to reach a data rate as high as 20 Mbps with a variable MI as low as 8%.

During the dissertation, the system overview will be described in details with the challenges and implementation of the circuits to achieve the goals. The description is enriched by simulations and testing for each stage of the transmission chain. The main design constrains of this research's study is summarised into the following items:

- **Frequency.** The choice of the frequency is a good trade-off to satisfy SAR-constrains and match the Self-Resonant Frequency (SRF) of the transmitting coil and receiving coil. The ISM band at 433.92 MHz is the first design constrain of the project.
- **Wireless Power Transfer.** The design of an optimal WPT focus on the improvement of delivered power and transmission efficiency in respect of the constrains imposed by SAR. The providing of energy to the implanted electronic systems exploiting the 3-coils IPT method is the second design constrain.
- **Wireless Data Communication.** Detailed analysis of different kinds of wireless data transmission regarding the constrains in terms of the power to transmit, and the demodulator's area required in the implanted device. The third design constrain is a high data rate.
- **Distance.** For this application, the distance between the external RF SWIPT transmitting unit and the neural implant is around $18 \div 20$ mm. Therefore, the fourth and last design constrains is the distance, which affects the wireless power transfer methods' choices in terms of delivered power and transmission efficiency.

Instead, for the realisation of an efficient SWIPT system, the main topics and goals can be summarised into the following items:

- **Power.** The external RF transmitting base station has to transmit enough power to supply the implanted device. Since the neural system does not have any internal power source, such as a battery, the implanted device requires a continuous power supply.

- **Modulation Technique.** The external RF transmitting base station requires using a simple modulation to favour the receiving side design due to its small available area (i.e. $200 \times 200 \mu\text{m}^2$).
- **Data Rate.** The external RF transmitting base station needs to maximise the data rate, ensuring a high resolution for visual prosthesis systems to stimulate a thousand CMOS-pixels.

Smart Micro Neural Dust is composed of a SWIPT base station, a 3-coils inductive power transfer link, and a thousand ultra-miniaturised CMOS chips. Each implant is free-standing and individually addressable from the external SWIPT system, providing a high selectivity brain stimulation. The project's main design constrains are: i) the strict dimensions of the implanted size, which nowadays result in a strong challenge in literature, and ii) location of powering and receiving system in the human head. The design choices and the implementation of the external RF transmitting base station are the objects of this thesis.

Figure 4.1 depicts the main blocks of Smart Micro Neural Dust. First, the video camera integrated into a pair of glasses records the images (i.e. Capturing Images step). Second, the images are processed (i.e. Signal Processing step). Third, the external simultaneous wireless information and power transfer base station transmits power and data simultaneously to the neural implants via the 3-coils IPT method. Finally, the phosphene perception is induced at a precise spatial location once the single-pixel stimulates the brain. The external base station requires a battery proving 5 V, while the implanted system is battery-less due to the strict constraints in terms of dimensions.

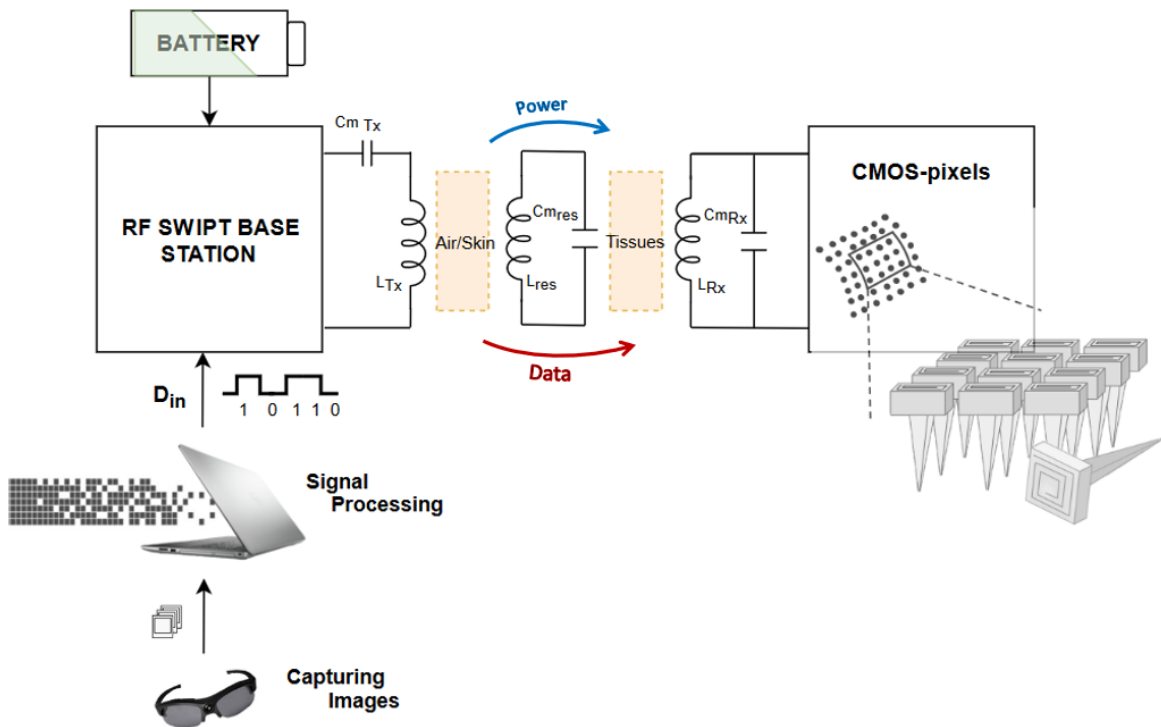


Figure 4.1: Main blocks of the planned Smart Micro Neural Dust.

The intended neural IMD imposes constrains in terms of physical limits that affect the size choice and the system's power budget. A particular focus is on SAR and the temperature rise of tissue close to the system, affecting cells' natural behaviour near the neural implant or, in the worst case, leading to cells' death.

4.1 WPT Method

One of the fundamental challenges for an IMD for continuous stimulation always remains the powering choice. The target system needs to a significant amount of energy to be powered due to the presence of a high number of μ electrode to ensure: i) the fulfilment of the tasks that the device must perform to obtain a proper stimulation of the cells, and ii) the best resolution, transmitting the respective image to the blind patient.

First of all, batteries are bulky and cannot be used in this case of distributed and ultra miniaturised neural implants. Therefore, WPT methodologies are key players to supply extremely miniaturised and free-floating neural implants.

For this neural application, far-field, APT and CPT has resulted in the least optimal choices among the different WPT methods for the following reasons:

- **Far-Field.** Signals at high frequency are required when far-field is used for neural IMDs. Therefore, the efficiency is reduced due to losses in the human tissues that dominate at high frequency.
- **Acoustic Power Transfer.** APT suffers from beamforming problems, high attenuation, and low selective stimulation.
- **Capacitive Power Transfer.** CPT presents reduced efficiency due to the low distance between the receiving plates (i.e. 200 μ m). Lower is the distance, lower is the efficiency. Moreover, the main limitation is the short penetration depth (e.g. few millimetres).

As described in Chapter 3, among WPT methods, 3-coils IPT emerges as the most appropriate method to supply multiple miniaturised chips with a medium penetration depth (i.e. 1-2 cm) [37]. WPT via inductive power transfer to miniaturised receiving coil is mainly limited by low Rx quality factor Q , low magnetic coupling at high distances and SAR. 3-coils IPT systems showed the best performance in terms of transmission efficiency, tolerance to misalignment and SAR-constrained delivered power. The efficiency of the driver is also negligible for 3-coils systems. IPT with multiple coils showed PTE increments even at considerable operating distance compared to 2-coils IPT systems [44].

4.1.1 Misalignment and Angular Rotation

Tx-Rx misalignment mainly limits the PTE and PDL of the link caused by a reduced mutual inductance M . M is inversely proportional to d^3 , that is the space between the centres of Tx and Rx. Therefore, an optimal alignment and positioning in parallel planes are required [60].

In this application, a slight misalignment probably will be present since the CMOS-pixels are located in a conformable mesh placed on the human brain's surface. The brain's surface is not smooth: bumps and protrusions, called *gyri* and *sulci*, makes it very irregular. The kinds of misalignment, affecting the measurements is lateral Δ and angular α . The angular misalignment [49] affects the mutual inductance M derived by (4.1):

$$M = \frac{M_0}{\sqrt{\cos\alpha}} \quad (4.1)$$

where M_0 is the mutual inductance between the two coils assuming a perfect alignment and α is the angular misalignment. Misalignment and angular rotation are critical factors in selecting the optimal powering method. In particular, the 3-coils IPT choice minimizes the PTE reduction caused by misalignment [61].

4.2 Frequency Selection

The operating frequency is one of the most significant design parameters in WPT via IPT. Optimal operating frequency is always a trade-off between: penetration depth, implant size constrains, tissue adsorption, and SAR limits. As a rule of thumb:

- Low operating frequency means less attenuation of human tissues, therefore low SAR for at specified input transmitted power. On the other side, PTE is maximized for big receiver sizes.
- High operating frequency means high attenuation of human tissue and higher SAR. Nevertheless, PTE is maximized for the small on-chip antenna on the implanted side system.

4.2.1 Specific Absorption Rate

The specific absorption rate of electromagnetic energy in human tissue is the object of many discussions due to the possible health risks. In any way, tissues represent a substantial dielectric and lossy material distribution in the near-field. The electric \mathcal{E} and magnetic \mathcal{H} fields do not have a plane-wave character in the near field. Still, they vary considerably from point to point. Therefore, all variables, such as radiation efficiency and impedance, are affected by the human tissue's physical, electrical, and magnetic properties.

The SAR is the most crucial metric to determine an RF source's electromagnetic energy exposure in a near-field, quoted over a volume of either 1 g or 10 g of human body tissue. It is defined in (4.2) as the time derivative of the absorbed energy dW in a mass dm :

$$SAR = \frac{d}{dt} \left(\frac{dW}{dm} \right) = \frac{d}{dt} \left(\frac{dW}{\rho dV} \right) \quad (4.2)$$

Ortherwise, more specifically:

$$SAR = \frac{\sigma_E}{2\rho} |\mathcal{E}^2| = c \frac{dT}{dt} \quad (4.3)$$

where c is the specific heat capacity, σ_E is the electric conductivity, ρ , instead, is the mass density of the tissue subject of examination, \mathcal{E} is the induced electric field and, finally, dT/dt is the increase of temperature in the tissue. SAR is defined in Watts per kilogram (W/kg). The induced electric field \mathcal{E} is extracted from the magnetic induction \mathcal{B} expressed in term of Weber per square meter (Wb/m²) following the Maxwell-Faraday's equation defined in the differential form in (4.4):

$$\nabla \times \mathcal{E} = -\frac{\partial \mathcal{B}}{\partial t} \propto \omega_0 I_1 \quad (4.4)$$

where I_1 is current which flows and ω_0 is equal to $2\pi f_0$ with f_0 the operating frequency. In some conditions, the SAR is assumed to be proportional to $(\omega_0 I_1)^2$ [62]. Therefore, keeping constant the SAR, a high request in terms of current for the stimulation tasks, I , implies to reduce the operating frequency, f_0 , since the induced electric field \mathcal{E} is proportional to the frequency and to the current.

4.2.2 IEEE Standard for Safety Levels

As regarding some standards, the Institute of Electrical and Electronics Engineers (IEEE) in the «Standard for Safety Levels with Respect to Human Exposure to Radio Frequency Electromagnetic Fields, 3 kHz to 300 GHz» stated the most crucial safety limits of exposure and levels of SAR [63], citing:

«The exposure conditions can be shown by appropriate techniques to produce SAR below 0.08 W/kg, as averaged over the whole body, and spatial peak SAR values not exceeding 1.6 W/kg, as averaged over any 1 g of tissue defined as a tissue volume in the shape of a cube, except for the hands, wrists, feet, and ankles where the spatial peak SAR shall not exceed 4 W/kg, as averaged over any 10 g of tissue, defined as a tissue volume in the shape of a cube.»

[IEEE Std C95.1, 1999 Edition]

Moreover, IEEE published for computations of RF electromagnetic fields [64] and for SAR test methods [65]. In the latter, simulation techniques, finite difference time domain numerical method, TestBench (TB) for testing and numerical models of the human body are described in detail. In general, SAR testing involves head's exposure. Table 4.1 summarizes the SAR limits in different countries and regions defining the respective membership organization/body [66]:

	USA	Europe	Australia	Japan
Organization/Body	EEE/ANSI/FCC	ICNIRP	ASA	TTC/MPTC
Measurement method	C95.1	EN50360	ARPANSA	ARIB
Whole body averaged SAR	0.08 W/kg	0.08 W/kg	0.08 W/kg	0.04 W/kg
Spatial-peak SAR in head	1.6 W/kg	2 W/kg	2 W/kg	2 W/kg
Averaging mass	1 g	10 g	10 g	10 g
Spatial-peak SAR in limbs	4 W/kg	4 W/kg	4 W/kg	4 W/kg
Averaging mass	10 g	10 g	10 g	10 g
Averaging time	30 min	6 min	6 min	6 min

Table 4.1: SAR limits in different countries. Reprinted from [66].

Table 4.1 highlights that the limit is 2 W/kg evaluated in 10 g of averaging mass for Europe, Australia and Japan. Instead, the limit is fixed to 1.6 W/kg for 1 g of averaging mass for USA and other countries, such as Canada, Bolivia and South Korea. The lower United States limit is more severe because it is evaluated in a smaller amount of tissue. Table 4.2 reports instead the maximum permissible exposure for controlled environments, defined as the space where exposure may be incurred in persons aware of the potential and risks or as the incidental result of transient passage through those locations [63].

Frequency Range (MHz)	Electric field strength \mathcal{E} (V/m)	Magnetic field strength \mathcal{H} (A/m)	Power density \mathcal{S} \mathcal{E}-field, \mathcal{H}-field (mW/cm²)	Averaging time $\mathcal{E} ^2$, $\mathcal{H} ^2$ or \mathcal{S} (min)
0.003 - 0.1	614	163	(100, 1 000 000)	6
0.1 - 3.0	614	16.3 / f	(100, 10 000/f ²)	6
3 - 30	1842 / f	16.3 / f	(900/f ² , 10 000/f ²)	6
30 - 100	61.4	16.3 / f	(1.0, 10 000/f ²)	6
100 - 300	61.4	0.163	1.0	6
300 - 3000	-	-	f/300	6

Table 4.2: Maximum permissible exposure for controlled environments. Table extracted from [63] and edited.

For the application described in this thesis, the frequency range is 300 ÷ 3000 MHz. Hence, the power density f , the electric \mathcal{E} , and magnetic \mathcal{H} fields have to be lower than $f/300$.

4.2.3 Tissue Adsorption

Tissue adsorption is significant in neural implants. The tissue composition in the human brain is characterized by a layered structure composed by: skin, fat, muscle, skull, and dura matter, CerebroSpinal Fluid (CSF), grey matter, and white brain matter. Each layer has a different effect and behaviour. Hence effects on impedance matching and standing waves result in different in terms of tissue absorption. [67].

In particular, electrical conductivity σ and relative permittivity ϵ_r of the human head tissues are key parameters for the adsorption mechanism. Electrical conductivity is influenced by measurement condition and environment, type of tissue, frequency, age, and possible pathologies of the patient [68]. The investigated variations in relative permittivity and electrical conductivity are conducted on layered head tissues, which change the content of water and tissue composition present in each analyzed biological level. The age accelerates the variations of these parameters, and they depend on the tissue types [69].

In fat tissue, a strong attenuation of standing-waves occurs if the water content is underestimated. Instead, in homogeneous tissue where the water content is higher, the effect of attenuation is smaller due to the fact that an increase of relative permittivity value relatively compensates a high electrical conductivity value. In Figure 4.2 and Figure 4.3 is shown the behaviour of these parameters. To better appreciate these parameters' behaviour, the conductivity is reported on the linear scale of the frequency axis, while relative permittivity on the logarithmic scale of the frequency axis. Their Matlab codes are reported in Appendix A.2.

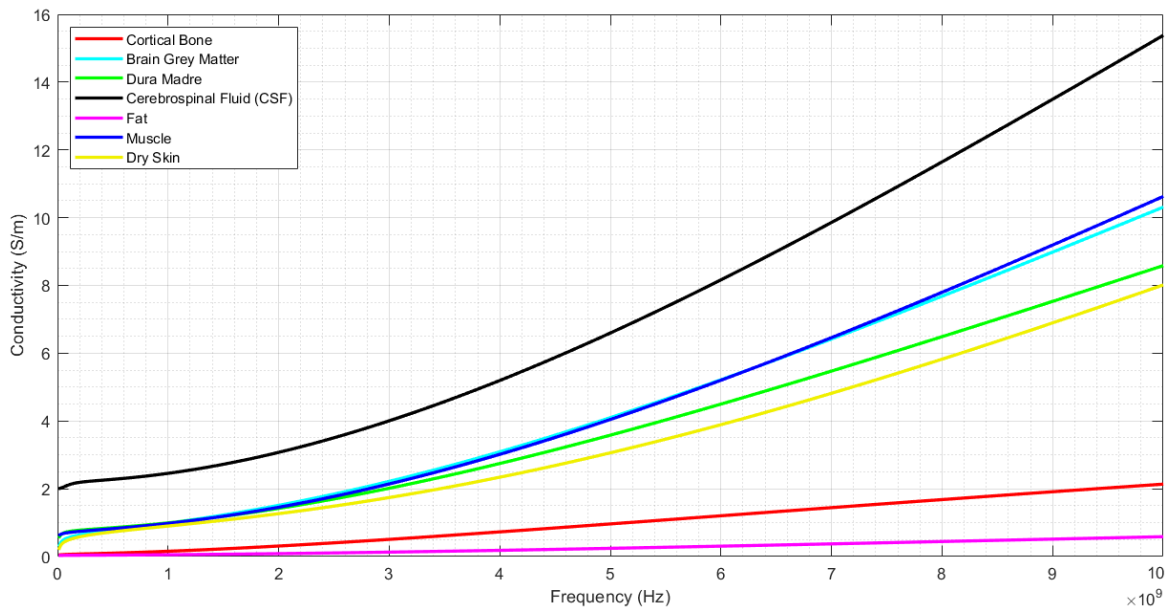


Figure 4.2: Behaviour of conductivity σ (S/m) in function of Frequency (Hz) with step of 20 MHz.

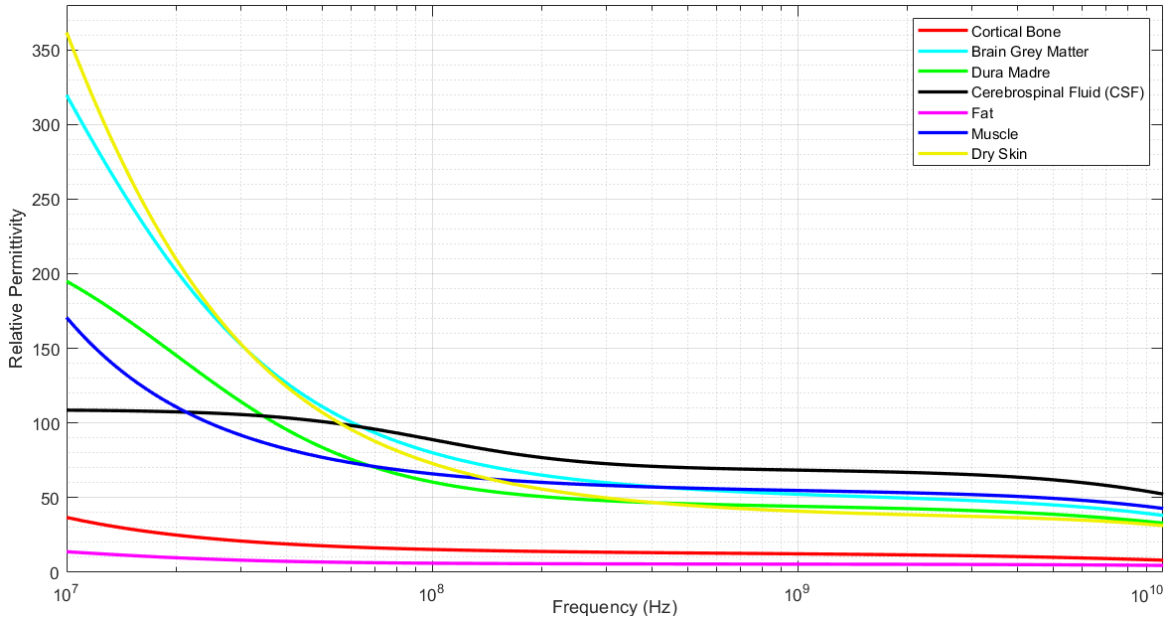


Figure 4.3: Behaviour of relative permittivity ϵ_r in function of Frequency (Hz) with step of 20 MHz.

Electrical conductivity increases as the incident field's frequency increases because of the excitation of the charge carriers increases. In other words, the higher the electrical conductivity, the higher the losses. For this reason, it is necessary to minimise the tissue losses operating at low frequencies. Instead, the relative permittivity decreases with increasing frequency due to the progressive decrease of the polarisation mechanisms [70].

These values of electrical conductivity and relative permittivity as a function of frequency for different human head tissues are extracted from «*Istituto di Fisica Applicata Nello Carrara*» (IFAC) website [71]. The latter allows calculating the body tissues' dielectric properties in the wide frequency range from 10 Hz to 100 GHz.

A brief extract of electrical conductivity and relative permittivity parameters are reported in Table 4.3, extracted from FCC, Table of Frequency Allocations for skin, muscle, skull, CSF, head tissue simulating liquid (HTSL), and body tissue simulating liquid (BTSL).

Frequency (MHz)	Parameters	Skin	Muscle	Skull	CSF	HTSL	BTSL
236	ϵ_r	53.0	59.3	13.7	74.9	48.3	59.8
	σ	0.61	0.75	0.08	2.2	0.82	0.85
450	ϵ_r	45.8	56.8	13.0	70.5	43.5	56.7
	σ	0.71	0.81	0.1	2.26	0.87	0.94
900	ϵ_r	41.4	55.0	12.5	68.6	41.5	55.0
	σ	0.87	0.94	0.14	2.41	0.97	1.05
1500	ϵ_r	39.4	54.0	12.0	67.6	40.5	54.0
	σ	1.07	1.19	0.23	2.72	1.2	1.33
1800	ϵ_r	38.9	53.6	11.8	67.2	40.0	53.3
	σ	1.18	1.34	0.28	2.97	1.40	1.52
2450	ϵ_r	38.0	52.7	11.4	66.2	39.2	52.7
	σ	1.46	1.74	0.39	3.46	1.80	1.95

Table 4.3: Relative permittivity ϵ_r and electrical conductivity σ of the body tissues. Reprinted from [69].

Neural IMDs operate in the MHz range of frequencies to reduce the dielectric losses in biological tissues. Nevertheless, operating at low frequencies, large capacitors are required, which increases the systems' bulkiness. Since the main strict constrains are the size in this application, it is necessary to avoid low range values of frequency.

4.2.4 Optimal Operating Frequency

As a rule of thumb, the optimal operating frequency in the case of miniaturised neural implant should be: higher than 250 MHz to permit miniaturisation and lower than 2.5 GHz to limit tissue adsorption and respect the safety restrictions [72]. Since the implanted neural devices shrink more and more, passing by centimetre to millimetre sizes, the operating frequency increases from a few dozen MHz to a few hundreds of MHz. The optimal operating frequency of the WPT system falls in the ISM radio band. The chosen value is 433.92 MHz, inasmuch at this value is possible to ensure the optimal amount of PDL and PTE in respect of the specific absorption rate limits.

Finally, the choice of operating frequency considers the inductors' sizes since low frequencies allow obtaining a lower power dissipation and limiting the heating of the tissues. Generally, larger inductors are necessary to favour high efficiency, but this is not possible due to the implanted side's constrains. Therefore, the chosen frequency value of 433.92 MHz is a good trade-off between the considerations presented in this section.

As proof of what mentioned regarding the choice of frequency and SAR limits, Figure 4.4 shows that the frequency range from 300 MHz to 500 MHz ensures the highest delivered power for the WPT method while respecting the limits of SAR fixed to 1.6 W/Kg represented by a straight red line. The most suitable ISM band is highlighted in orange colour. The values of PDL expressed in μW are referred to the ENGINI's project described in Section 2.3. It is given as an instance because the technical specs are similar to those of the proposed application in this thesis. Instead, in yellow colour are represented other available ISM bands but, at the lower frequency, these ensure low specific absorption rate values at the expense of reduced delivered power. On the other hand, at the higher frequency, the SAR exceeds the limits imposed by the Standards with the risk of not having a high PDL since a trend with a maximum peak characterizes the latter. Notice that the frequency axis is expressed in a logarithmic scale.

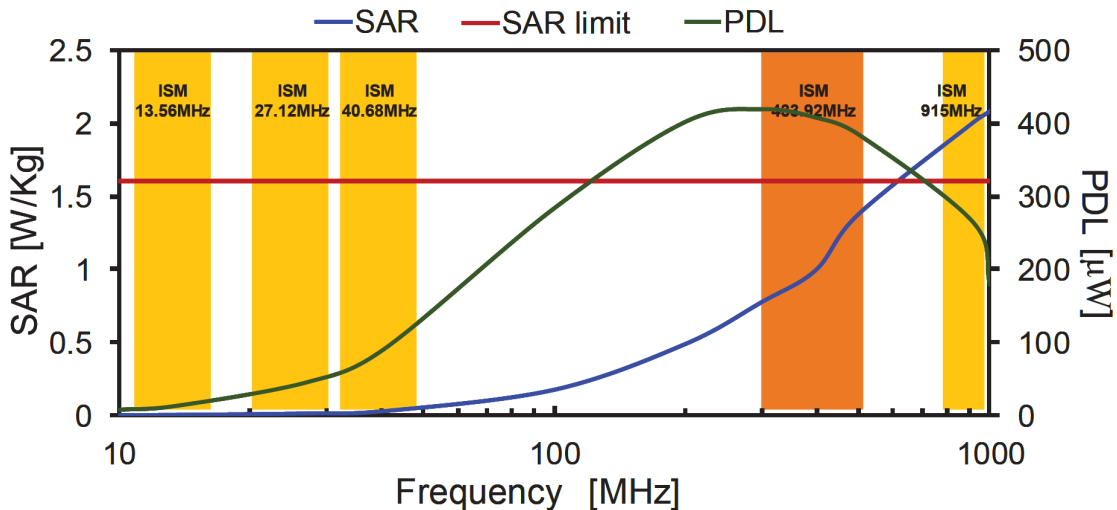


Figure 4.4: Choice of the optimal operating frequency of ENGINI's project in function of the PDL and under SAR restriction. Reprinted from [20].

4.3 Modulation Technique

Data transfer is another key element in designing RF SWIPT transmitters for several distributed and extremely miniaturised implants requiring large data transmission. Data communication needs to be robust enough against interference to keep an optimal BW. The choice of the type of modulation affects - and in certain case limits - the data rate. The optimal modulation technique is a trade-off between carrier frequency, data rate, sensitivity, circuit complexity, distance, area, and power consumption for both the transmitting and receiving side [47].

This master thesis has been discussed the multiple approaches of data telemetry, choosing ASK modulation. ASK results in the most suitable for: i) the coil-coupling method, and ii) its circuit simplicity, low area and Low Power (LP) consumption (considerations also valid for the demodulation block at the implant side). The other modulation techniques result the least optimal choices. The reasons are summarised in the following items:

- **On-Off Keying.** The SWIPT signal is the only source of energy for the implanted neural system. As a consequence, if the signal is turned off, the chip is no more supplied.
- **Frequency and Phase-Shift Keying.** FSK and PSK modulation suffer from a more complex circuit system and a low achievable data rate. A larger frequency BW is critical with high- Q coils. Moreover, in 3-coils IPT systems, the high- Q resonator inhibits frequency, and phase variations of the transferred signal [73].
- **Pulse Position Modulation.** PPM and PWM-ASK suffer from a low data rate. Therefore, as already downlink data telemetry has a strong limitation in achieving high data rate, PPM and PWM-ASK are excluded.

To conclude, the most suitable modulation technique for this application is ASK at the expense of slight inaccurate sensitivity to noise and variations and a lower data rate. Its design and implementation are described in Section 5.3.

4.3.1 Data Rate

Some neural IMDs, such as visual retinal prostheses and Cochlear Implants (CI), require a considerable quantity of data to be transmitted. Generally, for retinal prostheses, the optical data are transmitted with high data rates, up to a few tens of Mbps [46]. The IPT link is used to transfer not only power but also data. An increase in the carrier frequency carries an increase in the data transmission rate. Still, its maximum is limited to a few hundreds of MHz due to power losses in the biological tissues, which arise at higher frequencies [74].

The high data rate in LP condition is one of the key challenges of the proposed work. Data rate depends on the data typology to send in the neural IMD but substituting large electrodes with μ electrodes, the covered area naturally decreases. Therefore, the monitored region increases as the number of electrodes increases, consequently increasing the generated data that needs to be transmitted wirelessly. However, higher data communication of the RF transmitter causes high power consumption.

Considering the high number of channels (i.e. a thousand of CMOS-pixels) and the sampling rate, the minimum data rate limit for the downlink transmitter is set in the order of magnitude of Mbps. More precisely, the range of $6 \div 10$ Mbps is decided to send necessary stimulations to the neural system to ensure high resolution for visual prosthesis systems.

4.4 SWIPT System Specifications: Summary

Table 4.4 summarizes the system specifications and the design choices justified in this chapter.

General	Power Supply (V) SWIPT System	5 Yes
Powering	Method Frequency (MHz) Trasmitting Power (W) Trasmitter Size (mm) Trasmitter Material Trasmitting Distance (mm)	WPT via 3-coils IPT 433.92 $\simeq 1$ 10 Cu $18 \div 20$
Communication	Type Modulation Modulation Index Frequency (MHz) Data rate (Mbps)	Downlink ASK $\geq 8\%$ 433.92 ≥ 10
Notes	Antenna integrated on PCB	

Table 4.4: System and design specs of the external SWIPT RF transmitting system.

Chapter 5

RF SWIPT Transmitter: System Design and Architecture

The proposed external RF SWIPT transmitting base station comprises several electronic blocks to transfer power and data towards the implanted CMOS-chips. This chapter described the novel transmitter architecture realised and measured for simultaneous WPT and downlink data communication. Theoretical considerations, design procedures, simulations and laboratory implementations are reported.

The simplified chain of the proposed system's whole project is depicted in Figure 5.1. Instead, Figure 5.2 shows the RF transmitter architecture. It is composed of quartz, a Low Frequency (LF) Pierce oscillator, a Phase-Locked Loop (PLL), an ASK modulator, a class-AB power amplifier and a transmitting coil.

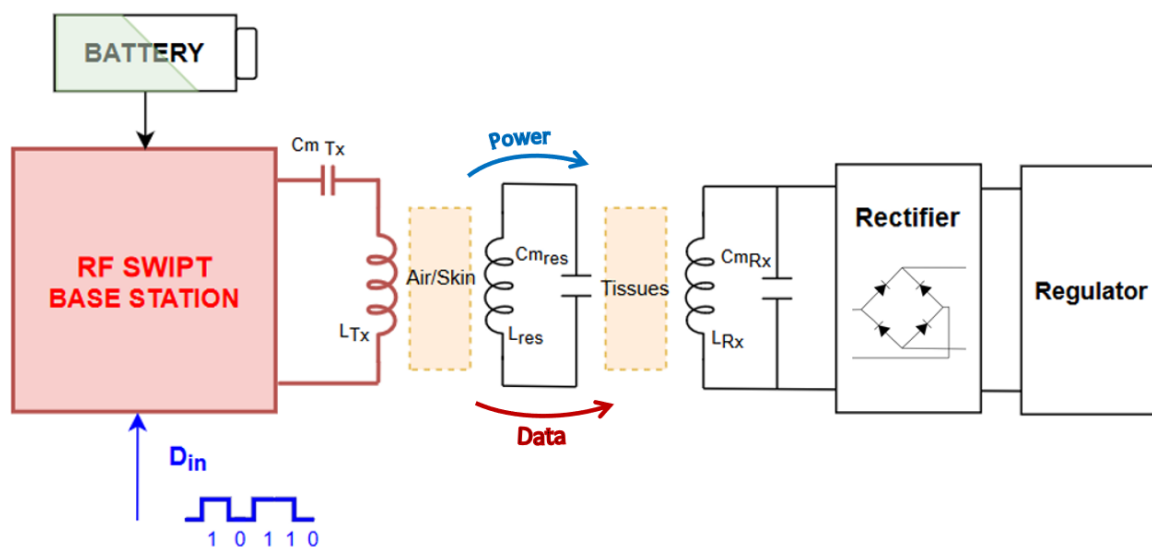


Figure 5.1: General scheme for a 3-coils IPT link. In red, the RF SWIPT transmitter proposed in this work.

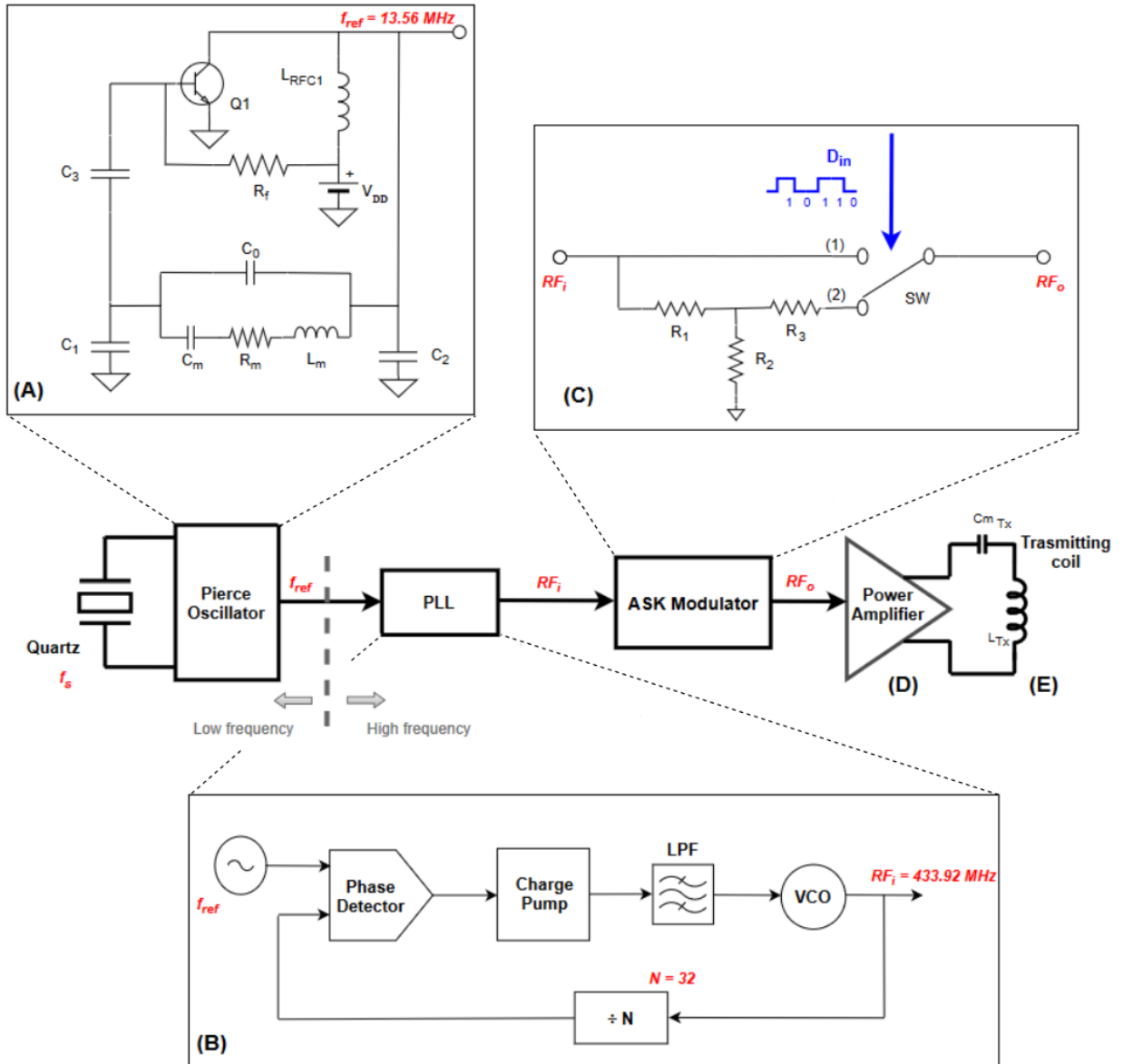


Figure 5.2: Main blocks of the external RF SWIPT transmitter: (A) LF Pierce oscillator; (B) PLL; (C) ASK modulator; (D) PA; (E) Transmitting coil.

5.1 Low Frequency Pierce Oscillator

The first electronic block of the designed external RF SWIPT transmitting base station is the reference LF oscillator in Pierce configuration (Figure 5.2-A). In general, crystal-based Pierce configuration is used with quartz oscillating in the range $9.735 \div 14.0625$ MHz, being advantageous in cost, size, and power consumption [75].

Crystal oscillators require quartz crystals with exemplary resonator to ensure frequency stability. In general, good quality factors Q assume values of the order of some hundreds of thousands [76]. Figure 5.3 reports the lumped circuit model of the quartz crystal described with the motional resistance R_m , the motional capacitance C_m , the motional inductance L_m and the package capacitance C_0 . The motional impedance represents the friction, inertia, and stiffness of the quartz crystal, while the package capacitance represents the plates' parallel capacity. In general, C_0 is in the pF-range, C_m is in the fF-range, and the resistor assumes small values of resistance as the quartz crystal's quality factor Q increases [77].

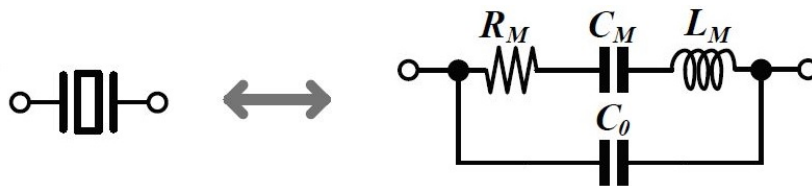


Figure 5.3: Lumped circuit model of a quartz crystal. Reprinted from [78].

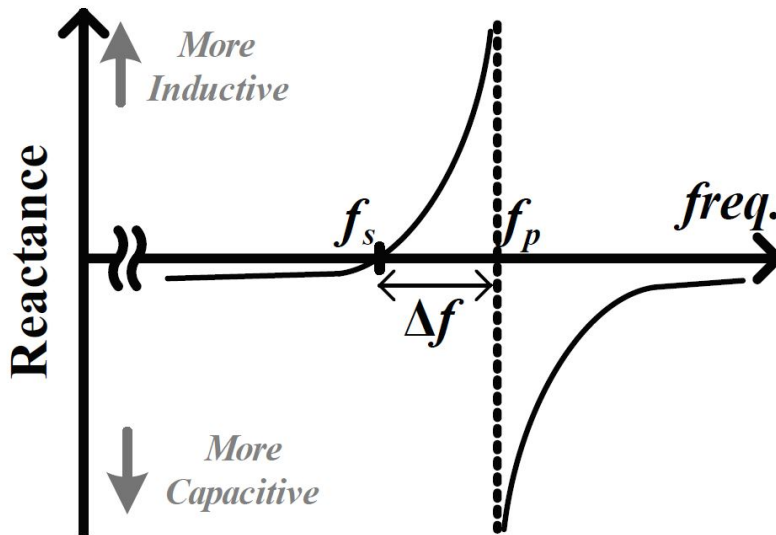


Figure 5.4: Crystal reactance vs. frequency. Reprinted from [78].

Quartz crystals have two frequencies with zero phases: series resonant frequency f_s and parallel resonant frequency f_p , also known as anti-resonant frequency. The series resonant frequency is calculated by (5.1):

$$f_s = \frac{1}{2\pi\sqrt{L_m C_m}} \quad (5.1)$$

f_s and f_p both appear as resistive behaviour in an oscillator circuit. More precisely, at f_s , the resistance is minimal, and consequently, the current flow is maximal. On the other hand, at f_p , the resistance is maximal, and the current flow is marginal. Therefore, f_p must never be used for an oscillator circuit. More precisely, a quartz crystal can oscillate at any point in the f_s and f_p interval, defined as the Δf range. Figure 5.4 reports an instance of the quartz crystal reactance curve as a function of frequency. It describes the variations of the quartz crystal's impedance as the applied frequency varies.

5.1.1 LF Pierce Oscillator Design Procedure

The Pierce oscillator's implementation requires a low number of components such as a quartz crystal, a transistor and resistors, capacitors and inductors. Its design implementation is characterized by large inductors values and small capacitors values.

The resonating frequency f_{ref} of the quartz crystal is 13.56 MHz and the lumped elements are determined accordingly (i.e. $R_m = 60 \Omega$, $C_m = 0.012003 \text{ pF}$, $L_m = 11.477 \text{ mH}$ and $C_0 = 2.949 \text{ pF}$). The Pierce oscillator's parameters showed in Figure 5.2-A (e.g. R_f , C_1 , C_2 , C_3 , L_{RFC1}) have been sized following the design procedure described in [78]. In particular, the feedback resistance R_f is inversely proportional to the frequency and it has been chosen equal to 1 M Ω , thus preventing physical damages of the crystal [79]. Table 5.1 reports typical range of its values:

Frequency	R_f Range
32.768 kHz	10 to 15 M Ω
1 MHz	5 to 10 M Ω
10 MHz	1 to 5 M Ω
20 MHz	470 k Ω to 5 M Ω

Table 5.1: Typical range values for feedback resistor R_f . Reprinted from [79].

R_f has to be within 470 k Ω and 5 M Ω at the operating frequency f_{ref} of 13.56 MHz. Assuming a lossless oscillator, f_{ref} is given as in (5.2):

$$f_{ref} = f_s \cdot (1 + \rho_c) = \frac{1}{2\pi\sqrt{L_m C_m}} \cdot \left(1 + \frac{C_m}{2C_L}\right) \quad (5.2)$$

where f_s is the series resonant frequency of the crystal, ρ_c is the pulling factor and C_L is the load capacitance (i.e. 20 pF, [80]). Hence, C_L is described as in (5.3):

$$C_L = \frac{C_1 C_2}{C_1 + C_2} + PCB_{strays} \quad (5.3)$$

where PCB_{strays} is the stray capacitance of the printed circuit board (i.e. 3 pF, [79]). In general, the transistor Q_1 (i.e. npn BJT) have a small parasitic capacitances and they have been neglected in (5.3). Therefore, solving (5.3) and supposing equal capacitance values, C_1 and C_2 both are equal to 27 pF [80]. The transistor has to be characterized by a higher transition frequency f_T than the required one for the oscillation frequency. In general, it is five times higher than the operating frequency f_{ref} to ensure a phase shift closes to 180°, satisfying in this way the Barkhausen criterion [76]. Last, L_{RFC1} represents the inductor choke, used to provide a constant current from the voltage supply V_{DD} provided from an external battery (i.e. $L_{RFC1} = 4.7 \text{ mH}$ for a $V_{DD} = 3.3 \text{ V}$).

Once the design was completed, the quality factor Q is verified. Its acceptable range of values is $[10000 \div 100000]$. In general, the quality factor is derived from the Figure of Merit (FoM) M . This parameter is used to compare the quality of quartz crystals and is defined as (5.4):

$$M = \frac{1}{\omega_0 C_0 R_m} = \frac{Q C_m}{C_0} \quad (5.4)$$

Therefore, Q is calculated as in (5.5):

$$Q = \frac{1}{\omega_0 C_m R_m} = \frac{1}{2\pi f_{ref} \cdot C_m R_m} \quad (5.5)$$

Replacing the numerical values, Q is equal to 16300 approximately, falling in the permitted range of values.

5.1.2 LF Pierce Oscillator Simulation and Implementation

This subsection reports the simulations realized on LTspice and its physical implementation on the breadboard. Figure 5.5 shows the circuit with values of the components following the design procedure described in the previous subsection.

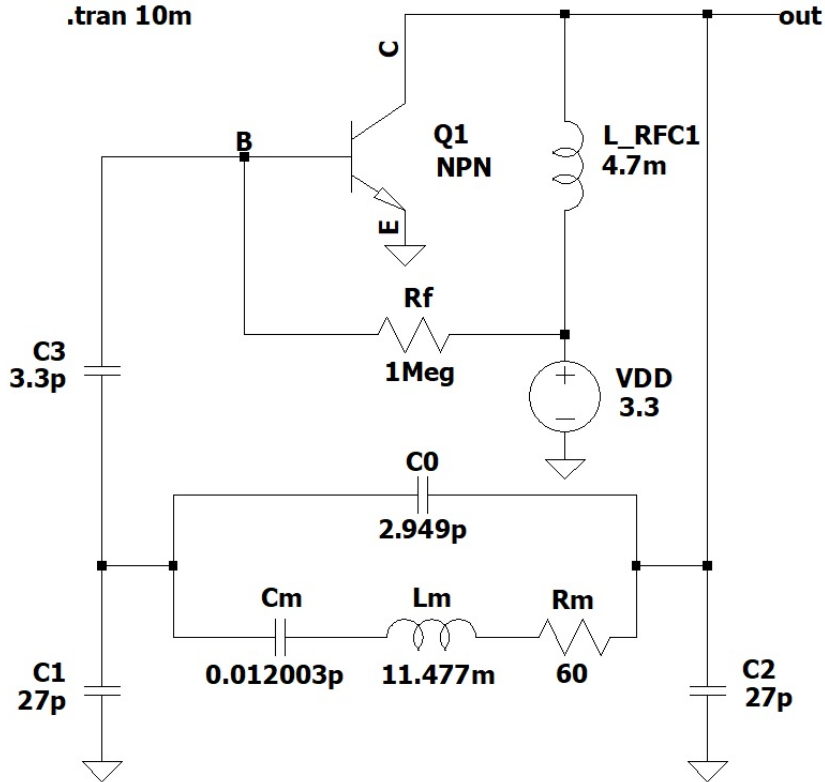
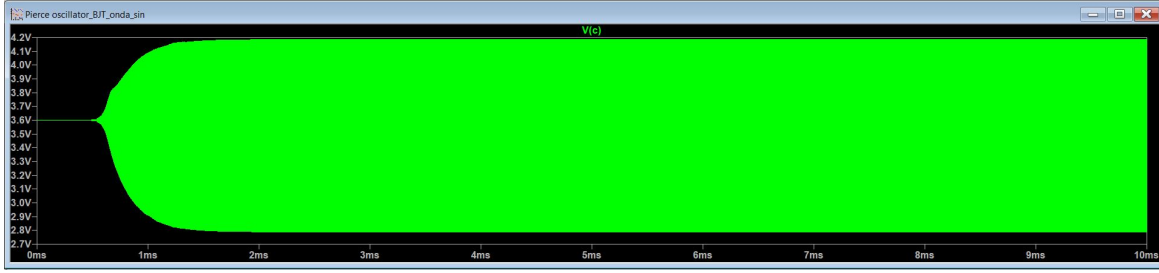
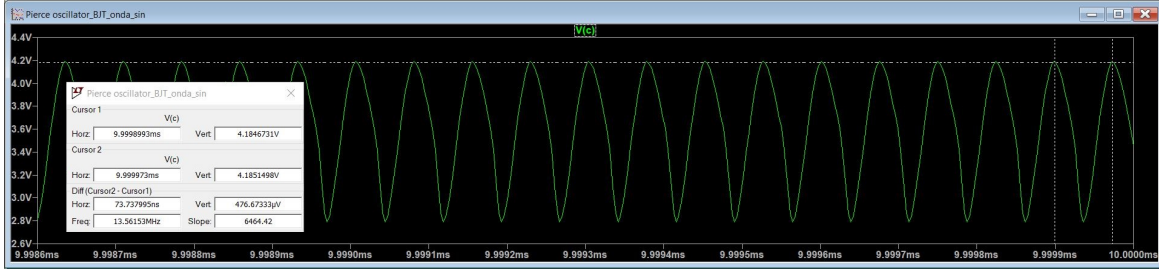


Figure 5.5: Pierce oscillator circuit implemented on LTspice with designed values .

Instead, Figure 5.6 reports its simulation where it is possible to appreciate the frequency f_{ref} . At 433.92 MHz, the ISM band is very narrow. Its width is 1.74 MHz. Therefore its permitted range of values is $[433.05 \div 434.79]$ MHz. Thus, the quartz crystal has to be very precise. A simulation transient of at least 10 ms is required to estimate the frequency exploiting the cursors, placed between peaks of two adjacent sinusoidal waves.



(a)



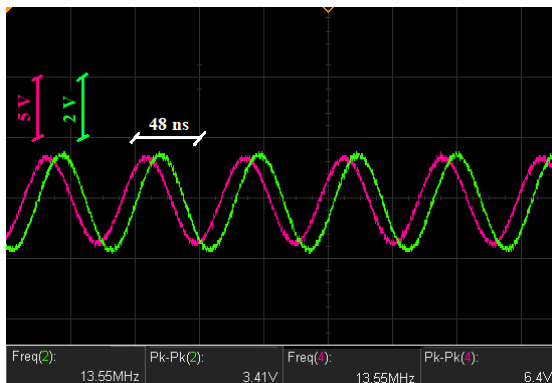
(b)

Figure 5.6: LF Pierce oscillator simulations on LTSpice. (a) Total view; (b) Close-up view around 10 ms.

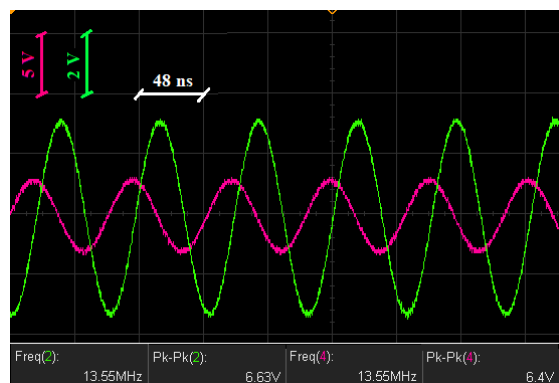
In the laboratory, the quartz crystal is tested to estimate the exact value of resonance frequency, where an increase of amplitude is expected. At resonance frequency f_{ref} , the driving force and the oscillator's velocity are entirely in phase. Therefore, the power transfer is maximised. The following relation explains this:

$$x = \frac{F_0}{m(\omega_0^2 - \omega^2)} \cdot \cos(\omega t) \quad (5.6)$$

Therefore, the amplitude becomes maximum when driven frequency equals the natural frequency, therefore $\omega = \omega_0$. Figure 5.7 shows the quartz crystal measurements at the non-resonance frequency and resonance frequency displayed on Digital Signal Oscilloscope (DSO).



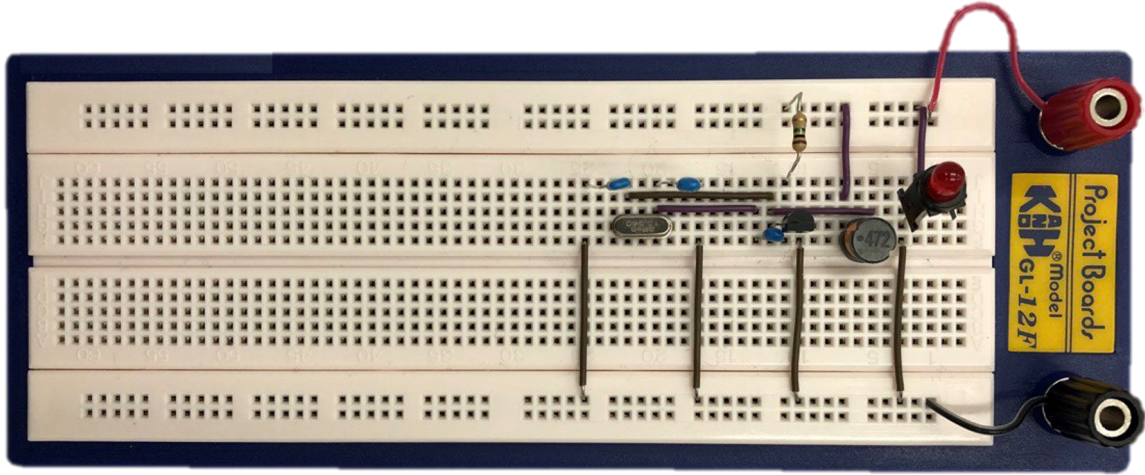
(a)



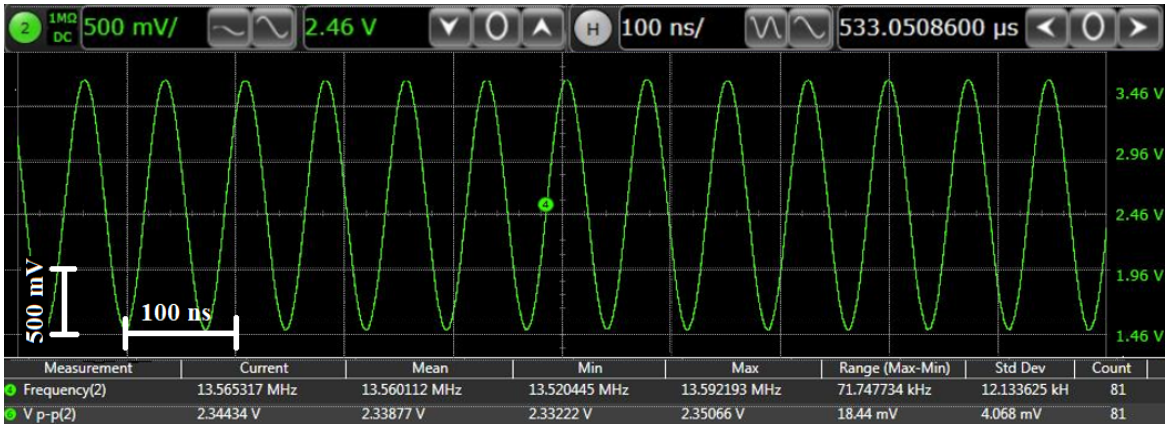
(b)

Figure 5.7: Simulations of quartz crystal at (a) non-resonance frequency and (b) resonance frequency.

The green sine wave is the quartz's output, while the pink sine wave is the reference signal, therefore, the output of the waveform generator. As expected, at f_{ref} , the amplitude increases from 3.41 V to 6.63 V. This value of the bought quartz crystal is 13.56312 MHz. Finally, Figure 5.8-a shows the Pierce oscillator's implementation realized on breadboard. On the other hand, Figure 5.8-b reports the measurement of the 13.56 MHz LF Pierce oscillator. A sinusoidal wave is appreciated. Pierce oscillator's working respects faithfully the simulation (Figure 5.6).



(a)



(b)

Figure 5.8: (a) Implementation of LF Pierce Oscillator on the breadboard. (b) Measurement of 13.56 MHz. Curves displayed on DSO with estimation of the frequency f_{ref} .

For the testing and the characterization, the designed LF Pierce Oscillator requires a matching network. The matching circuit is used to favour the maximum transfer in terms of power from one stage to another one. Its design is implemented by a parallel RC circuit (i.e. $R_{match} = 22\text{ k}\Omega$ and $C_{match} = 56\text{ pF}$).

Figure 5.9 reports the TB to extract the main electrical parameters for its characterization.

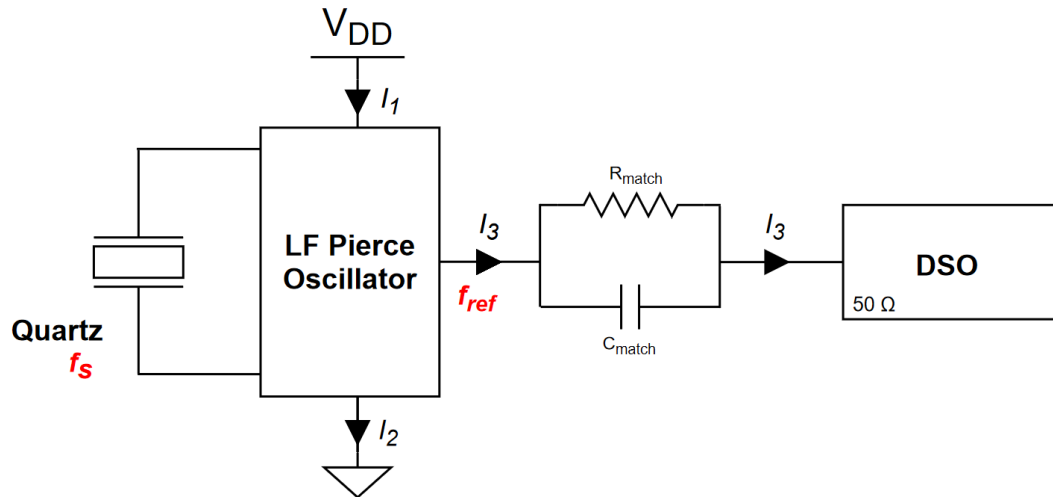


Figure 5.9: TB of LF Pierce oscillator.

Applying $V_{DD} = 3.3 \text{ V}$, the extracted values are: $I_1 = 0.93 \text{ mA}$, $I_3 = 0.15 \text{ mA}$, $I_{2\text{calculated}} = (I_1 - I_3) = 0.78 \text{ mA}$, $I_{2\text{measured}} = 0.79 \text{ mA}$. Instead, in terms of power, $P_{in} = 3.069 \text{ mW}$ and $P_{out} = 10.83 \text{ } \mu\text{W}$. Therefore, the estimated dissipated power is $P_{diss} = 3.058 \text{ mW}$.

5.2 Phase-Locked Loop

The phase-locked loop is commonly used to generate a multitude of frequencies from a single reference frequency provided by a crystal oscillator. Nowadays, PLL is used in a wide variety of high-frequency applications, mostly in radio communication at high performances and transceivers, ensuring a precise and stable output frequency RF_i starting with an input reference frequency f_{ref} [81]. It is used to generate, synchronize and demodulate any signal. In particular, it generates a signal V_o characterized by a specified phase and frequency related to the input signal V_i . Since the input signal is generally affected by noise or modulation, the signal can be rebuilt through the PLL defining phase, frequency and amplitude parameters properly. Therefore, in other words, this block can be seen as a narrow-band filter, able to remove noise, distortions and unwanted signal modulations. Regarding its block diagram reported in Figure 5.10, it is possible to define the phase error as the difference between the input θ_i and output phase θ_o . Supposing a linear Phase-Frequency Detector (PFD), the output voltage V_d is multiplied by the transfer function of the loop filter $F(s)$, which generates the control voltage at the input V_c of Voltage Control Oscillator (VCO). Finally, the VCO generates a local signal V_o with a frequency related to the control voltage V_c , without behaviour that it can be considered linear with some approximation [82].

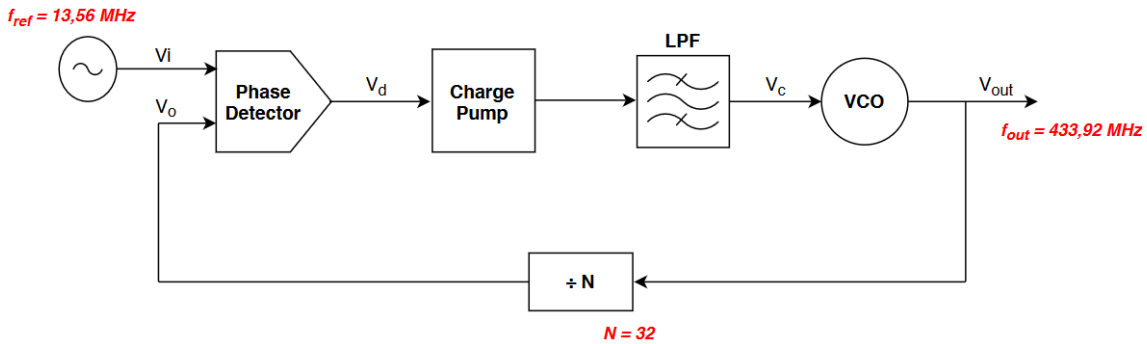


Figure 5.10: Block diagram and functional units of PLL.

Two typical different PLLs exist. First, in integer-N PLL, RF_i is equal to f_{ref} , which is the PFD, divided by the reference divider $1/N$, obtaining an RF_i N times higher than f_{ref} . Second, in fractional-N PLL, RF_i is a fraction of f_{ref} . An integer-N PLL has been designed selecting $N = 32$, calculated as the ratio between RF_i (i.e. 433.92 MHz) and f_{ref} (i.e. 13.56 MHz).

$$N = \frac{RF_i}{f_{ref}} = \frac{433.92 \text{ MHz}}{13.56 \text{ MHz}} = 32 \quad (5.7)$$

5.2.1 PLL Design and Simulation

PLL design (Figure 5.2-B) is a trade-off between reference frequency, operating frequency range, phase noise and frequency spur limitations. The author Ray Sun presents a simplified design approach solving the possible debug difficulties [83]. Its design has been developed through *ADIsimPLL*, as in Figure 5.11.

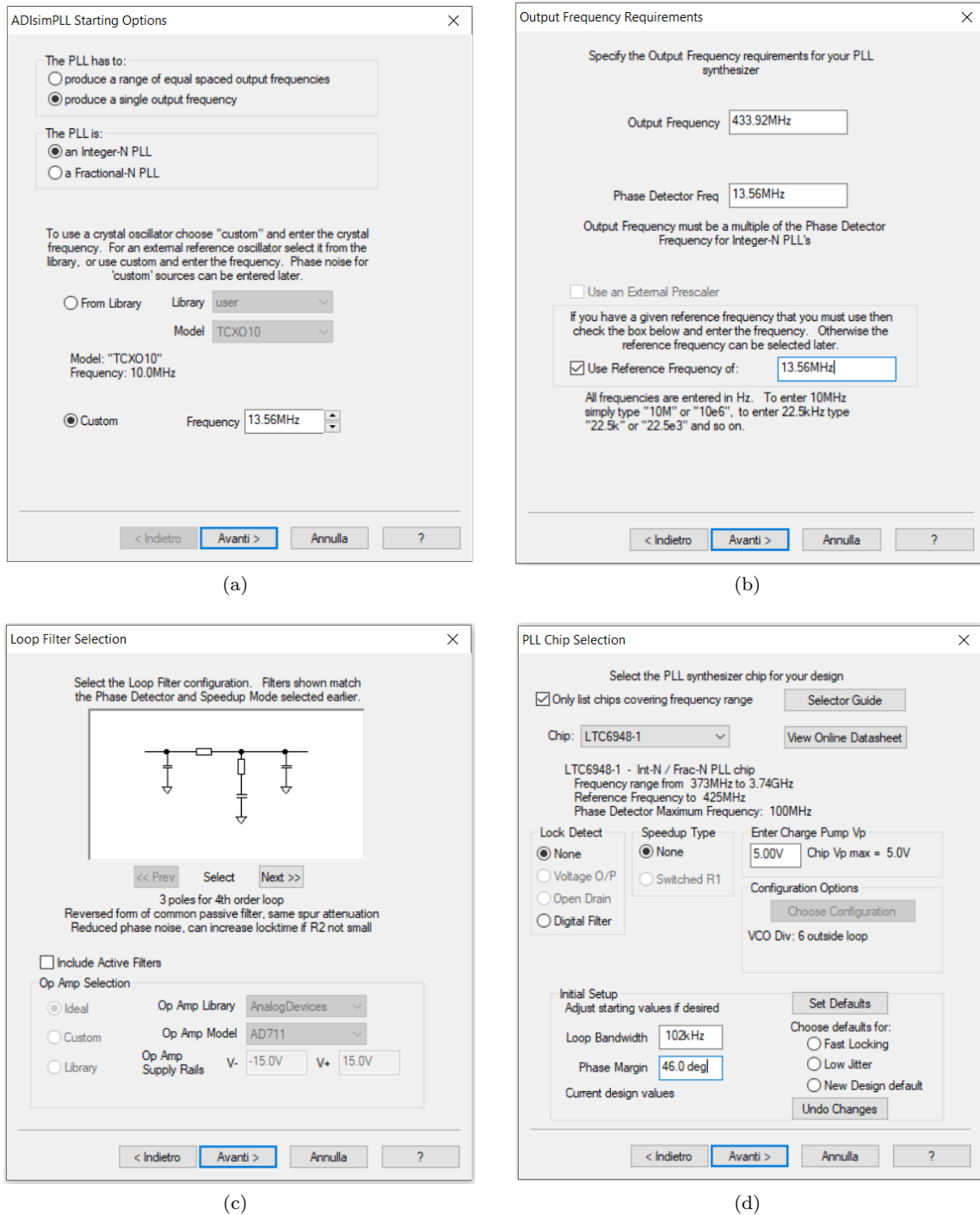


Figure 5.11: Main settings to determine the optimal choice of PLL defying: (a) Starting options; (b) Output frequency requirements; (c) Loop Filter Selection; (d) PLL chip selection. Settings extracted from *ADIsimPLL* software.

After defining the requirements mentioned above, such as an integer-N PLL with an output frequency RF_i of 433.92 MHz starting from a f_{ref} of 13.56 MHz and a 4th order loop filter, a proper choice of the PLL is made. The chosen one for this application is LTC6948-1 of *Analog Devices* characterized by an integrated VCO to facilitate the design.

PLL's schematic with the proper design of electrical components. As a rule of thumb, to minimize reflections, the PLL input impedance needs to be matched. Therefore, the input parallel capacitance should be small enough to avoid input noise that can arise in the loop.

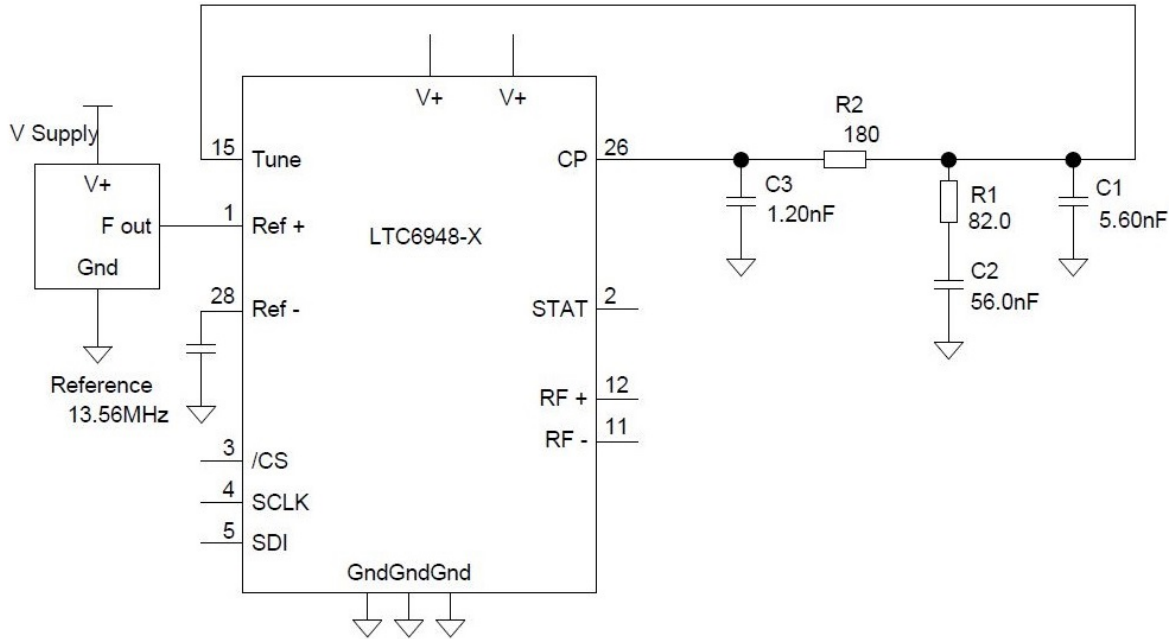


Figure 5.13: Schematic of LTC9648-1 of *Analog Devices*.

5.2.2 PLL Implementation and Analysis

The LTC6948-1 of Analog Devices is placed in the Demo Board DC1959B. A DC590 USB serial controller board characterized by Serial Peripheral Interface (SPI) communication is required to communicate, and the FracNWizard™ software controls it.

Figure 5.14 reports the measurement of PLL. The outputs of the PLL is connected to the matching network, characterized by a RC network (i.e. $R_{match} = 22\text{ k}\Omega$ and $C_{match} = 56\text{ pF}$).

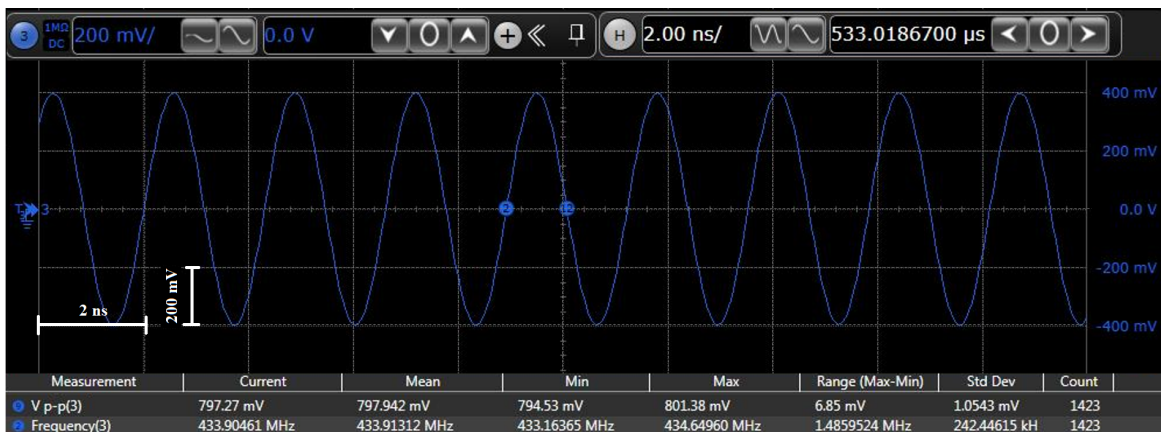


Figure 5.14: Measurement of the PLL output RF_i extracted from DSO.

5.3 Amplitude-Shift Keying Modulator

The modulation approach performs data transmission and power from the external transmitter base station to the neural implant. As described in Section 4.3, the choice of data telemetry typology is fundamental. Following the considerations described in Chapter 3, the optimal modulation scheme is the amplitude-shift keying. ASK modulation minimizes complexity, bulkiness and power dissipation in both the transmitting and receiving side. It is particularly suitable for data communication and widely used for the inductive-coupling approach. Moreover, an ultra-low MI (i.e. as low as 8%) ensures a functional powering of the implanted system exploiting WPT via IPT, avoiding driving the receiving side's transistors in a sub-threshold condition. Even if a low MI ASK transmitter is very challenging to achieve, it is the most optimal candidate for this application. The demodulators placed in the implanted neural system sometimes requires large values of capacitors. The latter occupies a significant area on the chip, becoming physically unacceptable for the imposed constraints [84]. This is the critical point for this application given the implanted side's limited availability area (i.e. $200 \times 200 \mu\text{m}^2$). For instance, modern CMOS technologies' capacitance density is in the range $1\text{-}2 \text{ fF}/\mu\text{m}^2$ [85], being size a critical point to be considered. In general, exploiting the ASK modulation technique, a capacitor-less demodulator can be implemented, allowing area saving.

To summarize, the ASK modulation technique presents the following characteristics:

- Suitable for the inductive-coupling approach in biomedical applications;
- Simplicity regarding modulation and demodulation design circuitry;
- Lower power consumption than the frequency and phase modulations;
- Simplicity of clock and data recovery algorithm;
- Poor synchronization between clock and data signals, inaccurate sensitivity to noise and inductive coupling variations.

Figure 5.15 reports an instance of the waveform for ASK modulation data transmission method implemented on Matlab software supposing to receive in input the following data "1101101".

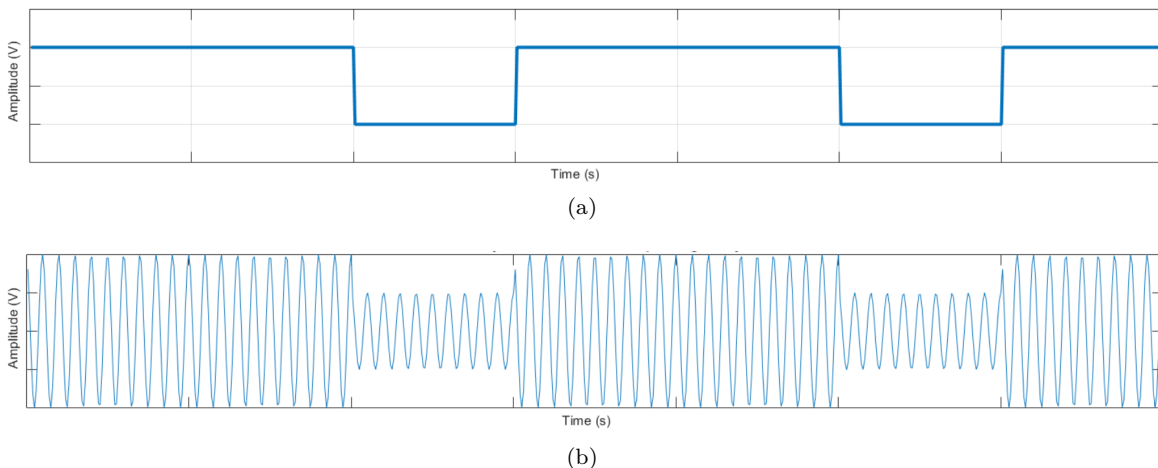


Figure 5.15: The conceptual waveform for ASK modulation related to the input binary information. (a) The transmitted digital signal in input; (b) Waveform of ASK modulation corresponding binary information.

5.3.1 ASK Modulator Design Procedure

In some cases, the carrier modulation is performed operating directly on the PA circuitry. For instance, Navaii and collaborators proposed a Darlington emitter-follower, which changes the supply voltage of a class-E PA, which is connected to the transistor's drain, performing the amplitude modulation, guarantying an optimal PTE [86]. Figure 5.16 shows their proposed modulation technique.

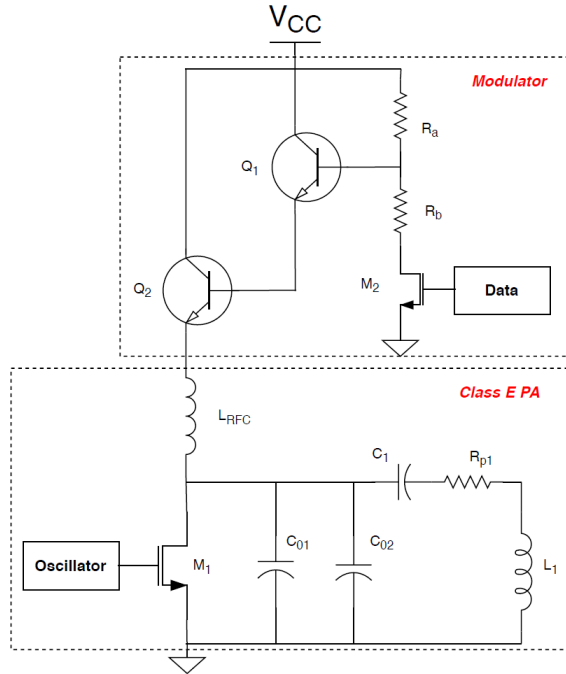


Figure 5.16: Schematic of a data and power transmission system with drain amplitude modulator and a class-E power amplifier.

This technique is suitable in biomedical applications: a class-E power amplifier switches between two tuned modes in the input data signal function. In particular, they implemented a 2-coils IPT-based RF transmitter exploiting the ASK modulation using a carrier frequency fixed at 10 MHz with a MI of 0.1, transmitting information at a data rate of 1 Mbps. The same design has been implemented on MultiSim software using the parameters annotated in Table 5.2, as described in [86].

Parameters	Designed Values	Standard Values
Supply Voltage	$V_{CC} = 3.4 \text{ V}$	$V_{CC} = 3.6 \text{ V}$
Shunt Capacitors	$C_0 = 31.62 \text{ pF}$	$C_0 = 20 \text{ pF} + 10 \text{ pF}$
Tuned Capacitors	$C_1 = 162.85 \text{ pF}$	$C_1 = 100 \text{ pF} + 82 \text{ pF}$
	$C_2 = 99.33 \text{ pF}$	$C_2 = 100 \text{ pF}$
Modulator RC	$R_a/R_b = 0.14$	$R_a = 33 \Omega$
		$R_b = 510 \Omega$
RF choke inductor	$L_{RFC} = 47 \text{ nH}$	$L_{RFC} = 47 \text{ nH}$
Darlington transistor	MMBTA13	MMBTA13

Table 5.2: Designed theoretical parameters and final chosen parameters based on available standard values. Reprinted from [86].

The obtained simulation results respectively for a 10 MHz carrier frequency and a data rate of 1 Mbps.

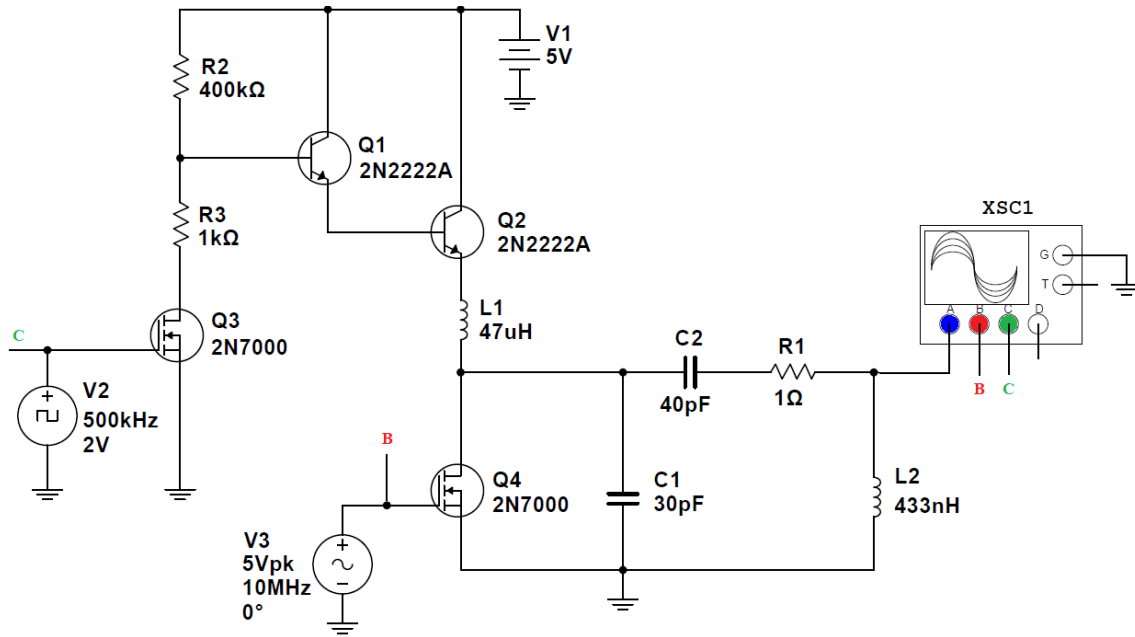


Figure 5.17: ASK modulation circuit of a Darlington emitter-follower approach working at 10 MHz and with a data rate of 1 Mbps.

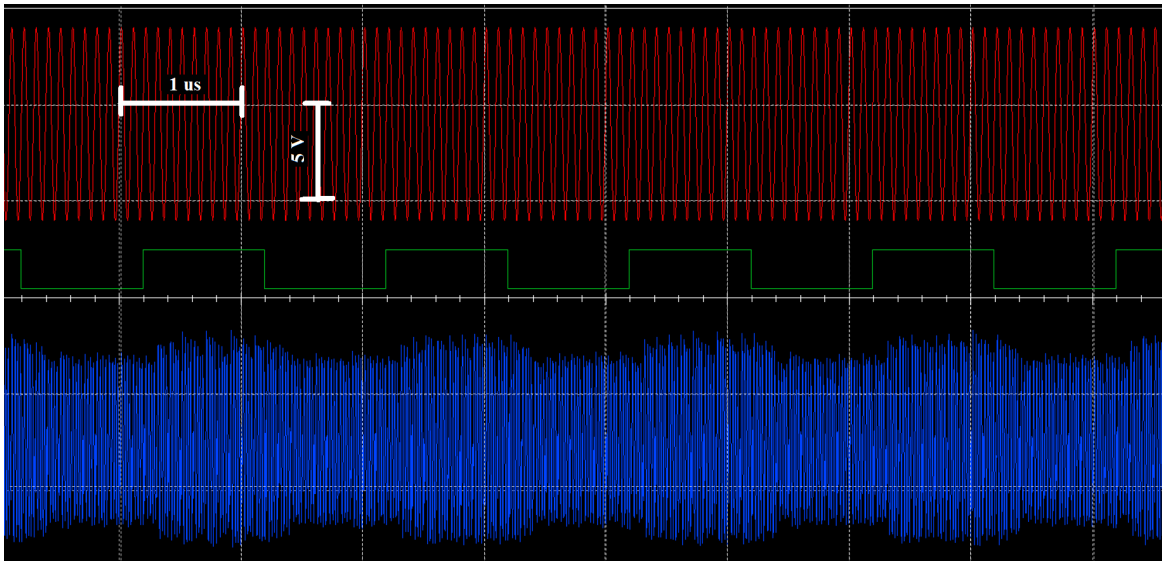


Figure 5.18: Basic waveforms simulation of the proposed topology. The red and blue sine waves are the carrier and the modulated signal, respectively. The green square wave simulates the input data.

The high noise transition, caused by the high sensitivity of the class-E power amplifier, emerges from the simulation. This results in a high BER.

Then, using the same design strategy, the modulator working at 433.92 MHz and at a data rate of 10 Mbps has been designed. In particular, the modulation index has been calculated as (5.8):

$$MI = \frac{V_{CC} R_a}{(R_a + 2R_b) \cdot V_{CC} - 4(R_a + R_b) \cdot V_{BE}} \quad (5.8)$$

where, the MI is application dependent (i.e. $MI = 0.1$ for this work), the supply voltage V_{CC} is equal to 3.4 V, the base-emitter voltage V_{BE} for a npn transistor is generally about 0.6 V. To obtain the total equivalent resistance on the primary side R_{eq} , R_a is fixed 300 Ω to get R_b .

$$R_{eq} = R_{p1} + R_{ref12} \quad R_{ref12} = \frac{(M_{12} \omega_c)^2}{R_{p2} + \frac{(L_2 \omega_c)^2}{R_L}} \quad (5.9)$$

where, R_{p1} and R_{p2} are the parasitic resistance of coils L_1 and L_2 , and considered negligible since lower of 0.5 Ω . The load resistor R_L is fixed to 50 Ω , even if more truthful values approach entities of a few unit of k Ω .

To calculate R_{ref12} , the mutual inductance M_{12} and the resonant frequency of the secondary side ω_c are required. Therefore, M_{12} is extracted by the coupling coefficient k_{12} between the coils L_1 and L_2 (5.10). k_{12} is evaluated in the worst condition at 0.3. On the other hand, ω_c is derived by (5.11):

$$k_{12} = \frac{M_{12}}{\sqrt{L_1 L_2}} \quad (5.10)$$

$$\omega_c = \frac{1}{\sqrt{L_1 L_2}} \quad (5.11)$$

The admitted values of C_2 are a few unit of pF, while of L_2 are a few hundreds of nH. To conclude the design, the capacitances C_1 and C_0 are estimated by (5.12) and (5.13):

$$C_1 = \frac{1}{\omega_c^2 (L_1 - \frac{X_c}{\omega_c})} \quad X_1 = 1.1552 R_{eq} \quad (5.12)$$

$$C_0 = \frac{1}{5.4466 \omega_c R_{eq}} \quad (5.13)$$

where, X_1 is reactance of the load network obtained by the impedance of C_1 and L_1 at resonant frequency ω_c . Finally, the inductance choke minimum L_{RFC} is derived by (5.14), given the C_0 and ω_c .

$$L_{RFCmin} = \frac{1}{0.36 \omega_c^2 C_0} \quad (5.14)$$

To facilitate the design making it computational, the previous relations have been reported on Matlab. The implemented code based on resolution of systems of equations is reported in Appendix A.4. The obtained values in respect of the design choices are: R_b equal to 270 Ω ; M_{12} equal to $1.27 \cdot 10^{-8}$; L_1 and L_2 equal to 40 nH and 45 nH, respectively. Finally, C_0 and C_1 equal to 20 pF and 3 pF imposing L_{RFCmin} to 47 nH. These values are inserted in the design shown in Figure 5.17.

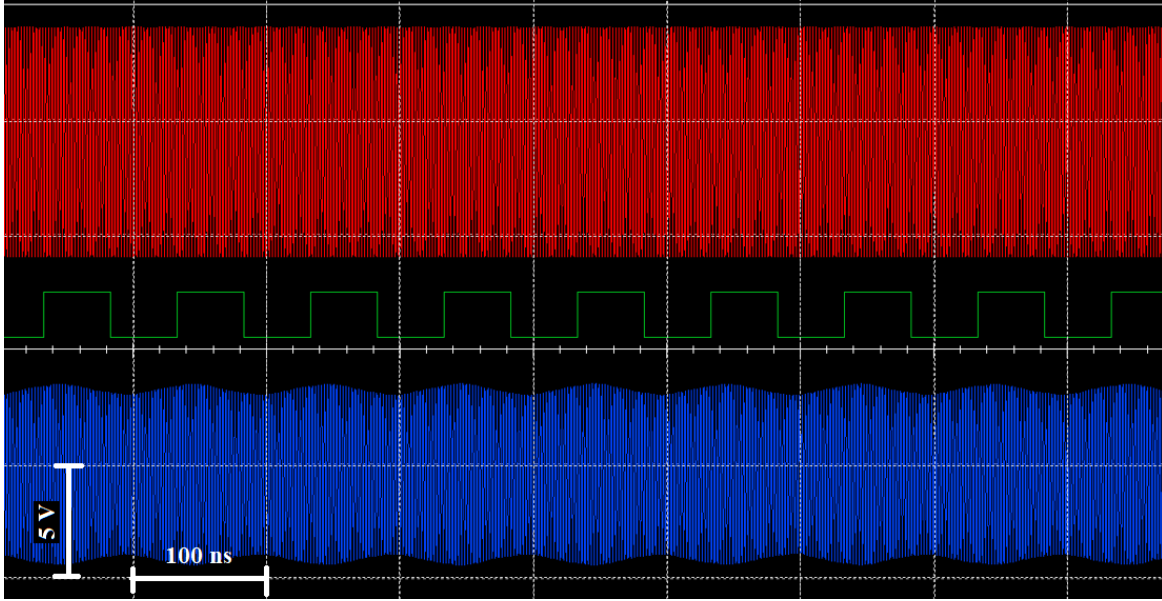


Figure 5.19: Simulation of basic waveforms of the ASK modulator of the proposed topology working at 433.92 MHz and with a data rate of 10 Mbps. The red and blue sine waves are the carrier and the modulated signal, respectively. The green square wave simulates the input data.

Figure 5.19 reports the simulation result. The noise on transition is even more present than the previous results (Figure 5.18). In particular, the simulation shows the complete absence of vertical edges, leading to a non-optimal working of the ASK modulator since the BER is expected to be particularly high. Therefore, the proposed model [86] is not efficient under the conditions and constrains defined in this thesis.

5.3.2 ASK Modulator Simulation

The novel modulation approach is based on a switch and a voltage divider, as shown in Figure 5.20. The voltage divider attenuates the amplitude of the carrier signal RF_i . The symmetrical T-pad voltage divider's resistances are designed to obtain a modulation index MI equal to 0.1.

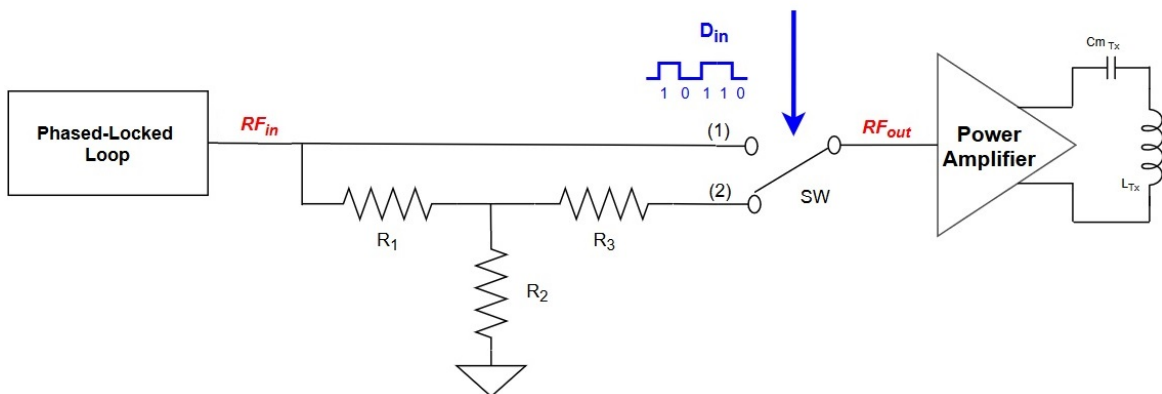
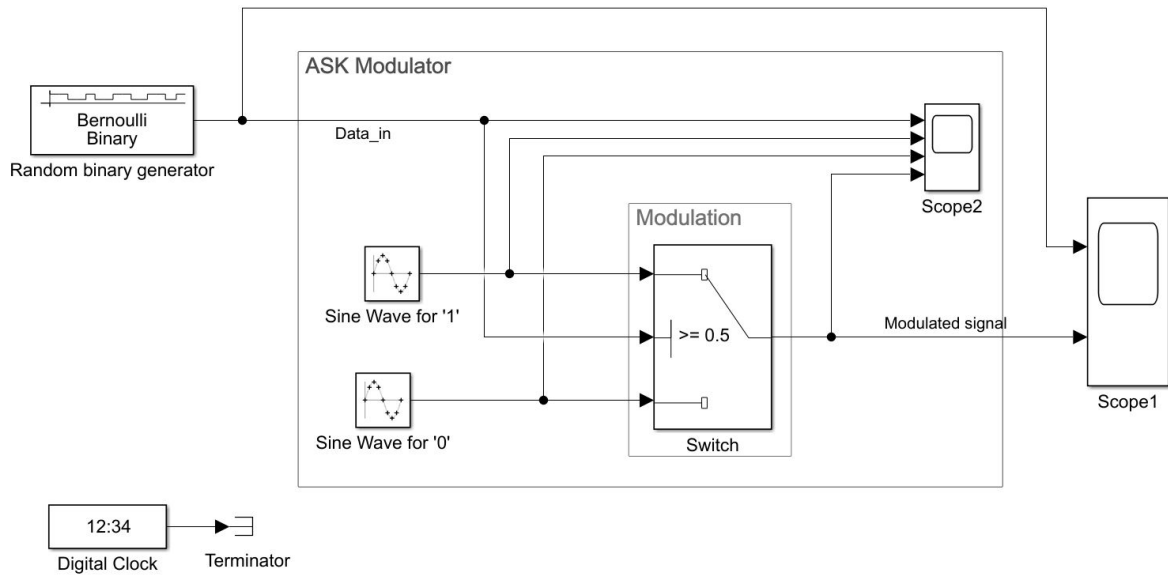
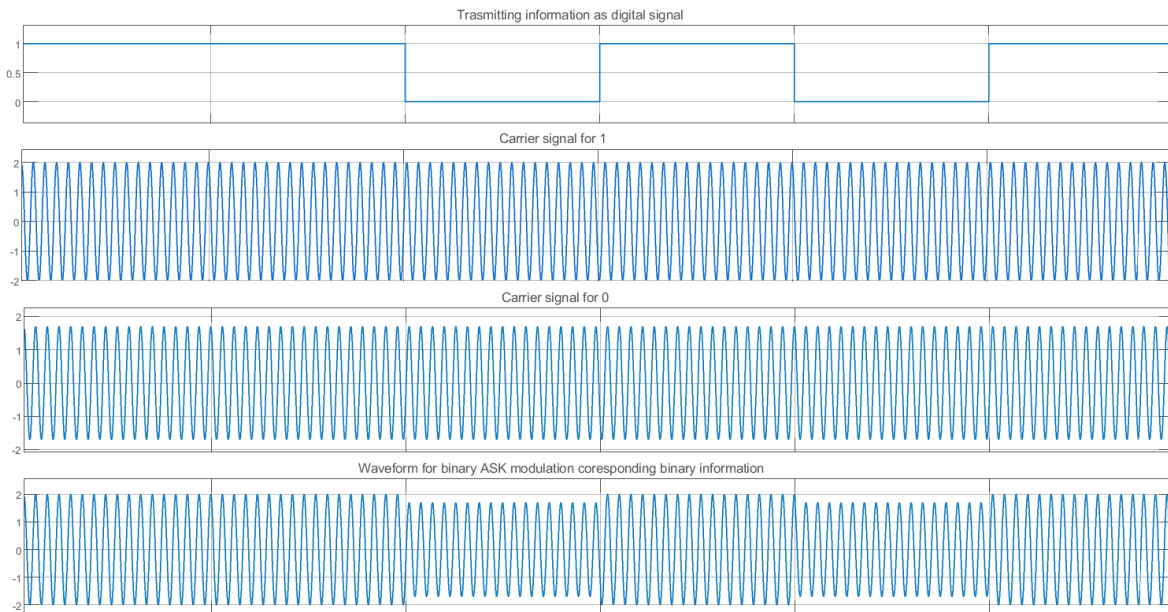


Figure 5.20: Schematic of the new approach based on switch between two tuned modes.

The conceptual idea of this novel approach is reported in Figure 5.21-a.



(a)



(b)

Figure 5.21: (a) Conceptual idea of the new approach based on switch between two tuned modes described through block diagrams. (b) Simulation with the output of scope.

The Simulink scheme is characterized by: i) a random binary generator based on the Bernoulli algorithm, ii) a three-ports switch that implements the ASK modulator, and iii) two sine wave generator blocks to simulate the sine wave for logical "high" and "low" states. The main parameters for the sine waves are the output signal and the sample per period derived by (5.15) and (5.16):

$$Output(t) = Amplitude \cdot \sin(Frequency \cdot t + Phase) + Bias \quad (5.15)$$

$$Samples\ per\ period = \frac{2\pi}{Frequency * Sample\ time} \quad (5.16)$$

The first sine wave generator simulates the logical "high" state characterized by an amplitude of 2 unit, while the second sine wave generator simulates the logical "low" state characterized by an amplitude of 1.7 unit. Finally, the results are extracted from the scope. Figure 5.21-b reports the output of the Scope2.

In Figure 5.20, the schematic presents the symmetrical T-pad voltage attenuator that works as in (5.17):

$$\begin{cases} RF_o = RF_i & \text{if } SW = 1 \\ RF_o = RF_i \cdot \frac{R_2 \parallel R_3}{R_1 + R_2 \parallel R_3} = RF_i \cdot (1 - MI) & \text{if } SW = 2 \end{cases} \quad (5.17)$$

where RF_o and RF_i are respectively the signals before and after the modulation block, R_1 , R_2 and R_3 are the three resistances of the T-pad attenuator. In particular, R_2 may be modified to obtain a system with a variable MI (i.e. for $MI = 0.1$, $R_1 = R_3 = 10 \Omega$, $R_2 = 470 \Omega$). The Multisim implementation and simulation are reported in Figure 5.22 and Figure 5.23, respectively.

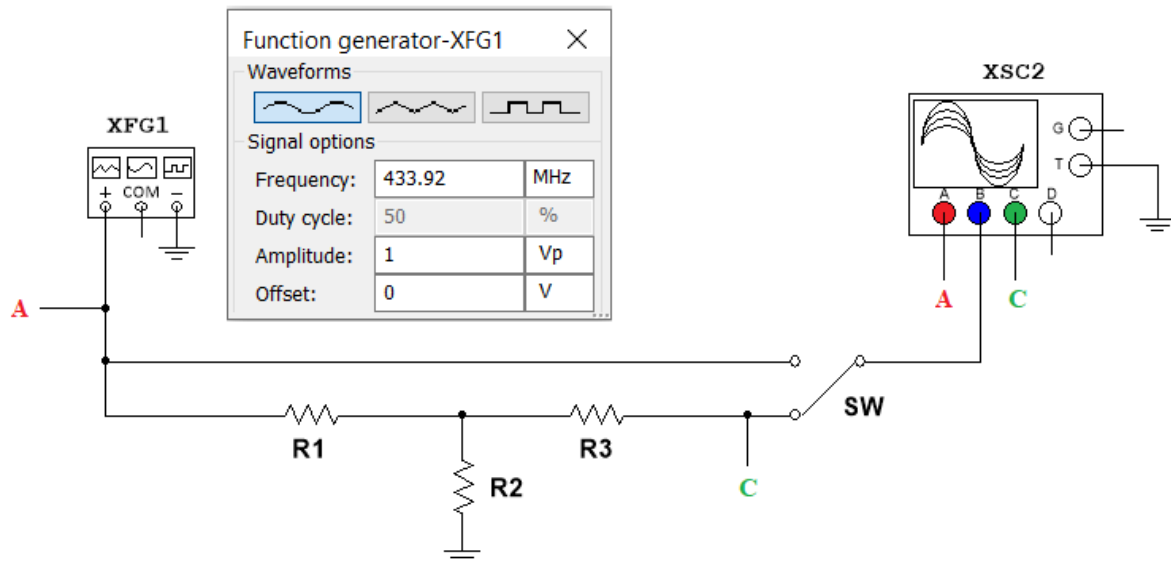


Figure 5.22: Circuit of the new approach based on switch between two tuned modes. Schematic realized on MultiSim software.

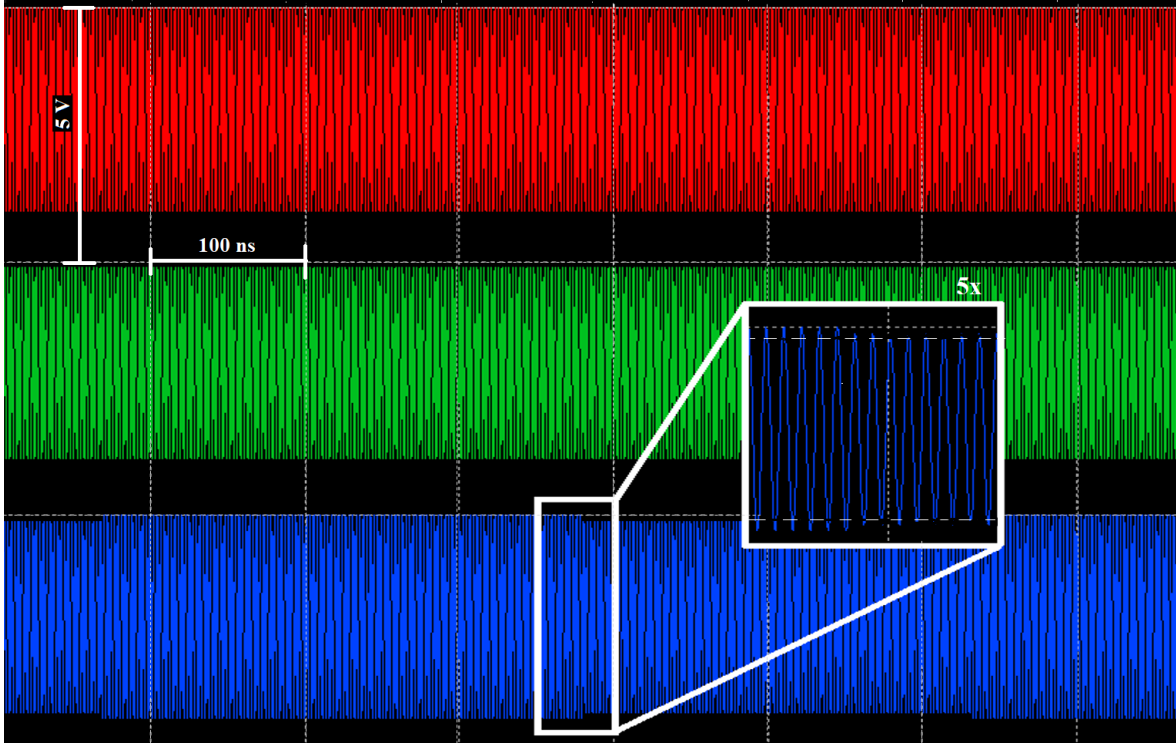


Figure 5.23: Simulation of the new approach based on the switch between two tuned modes.

The red sine wave is the carrier at 433.92 MHz, the green sine wave is the carrier attenuated in amplitude by the symmetrical T-pad, and the blue sine wave is the output modulated signal.

5.3.3 ASK Modulator Implementation

For the ASK modulator's implementation, a potentiometer of the same range of values substitutes the resistance R_2 to obtain a more versatile circuit.

The switch SW is characterized by an internal driver designed for wide-band applications (i.e. M3SW-2-50DRA+ by Mini-Circuits'). Accordingly with a data rate as high as 20 Mbps, the switching times needs to be smaller than 50 ns because:

$$t_{sw_{min}} = \frac{1}{Data\ rate_{max}} = \frac{1}{20 \cdot 10^6} = 50\ ns \quad (5.18)$$

For this reason, the RF switch is chosen in function of the values of rising and falling times. The chosen RF switch has $t_{rise} = 3.3\ ns$ and falling time $t_{fall} = 4.6\ ns$. Figure 5.24 shows the schematic of the evaluation kit.

To conclude, different MIs can be obtained by modifying the design of the symmetrical T-pad voltage attenuator. In particular, Figure 5.25 reports three different designs with 3 dB, 2 dB and 1 dB, obtaining MI equal to 0.2, 0.17 and 0.08, respectively.

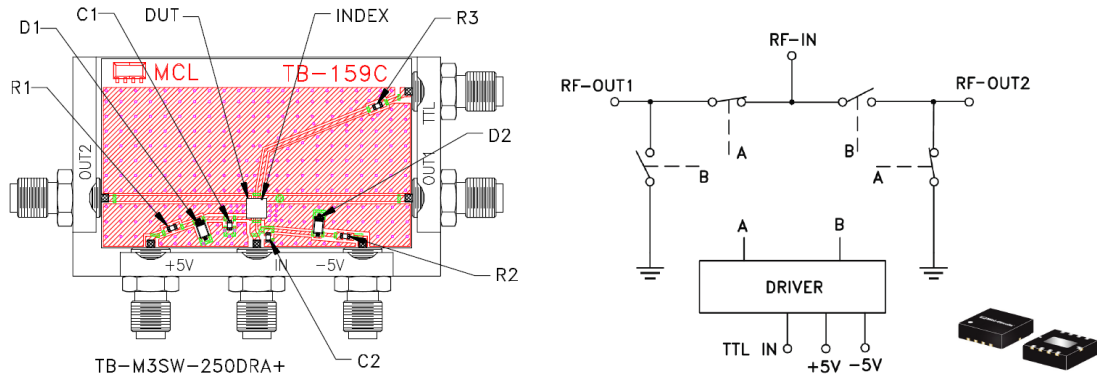
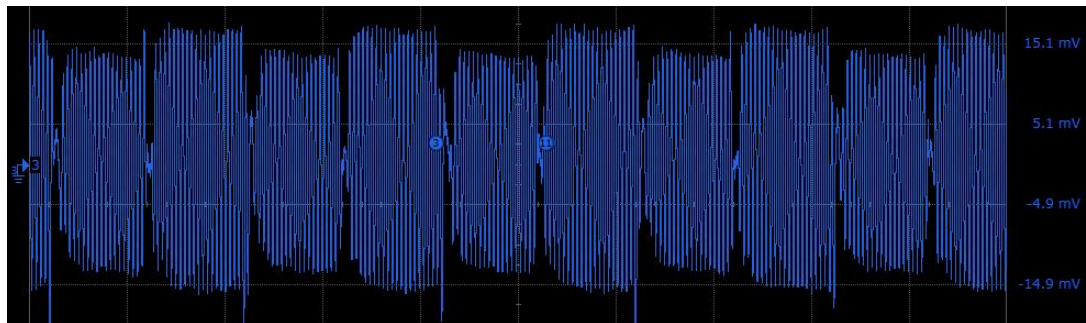
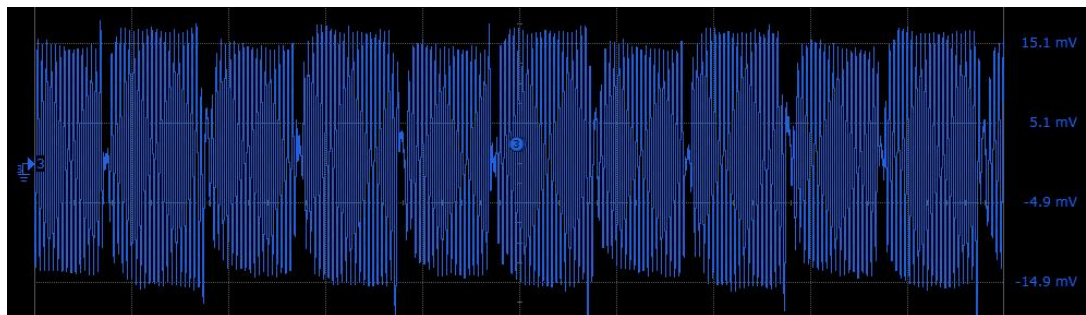


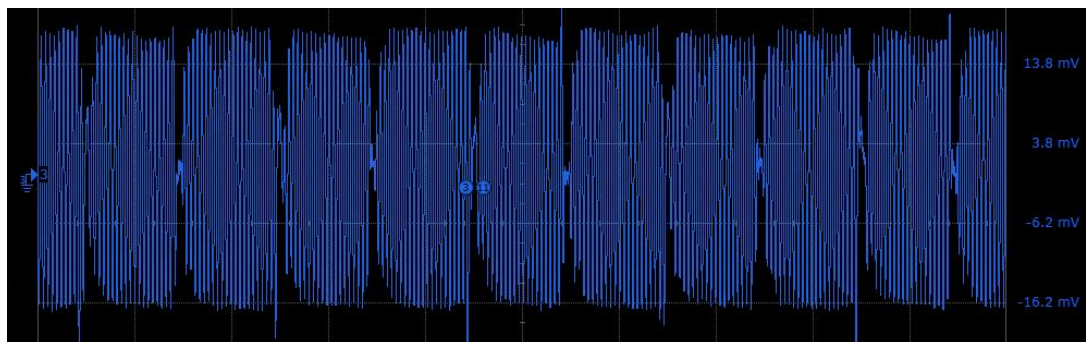
Figure 5.24: Evaluation board and circuit of the M3SW-2-50DRA+ by Mini-Circuits'. Extracted from the datasheet.



(a) 3 dB attenuator. $Amp_1 = 33$ mV, $Amp_2 = 26$ mV, hence MI = 20%.



(b) 2 dB attenuator. $Amp_1 = 33$ mV, $Amp_2 = 28$ mV, hence MI = 17%.



(c) 1 dB attenuator. $Amp_1 = 33$ mV, $Amp_2 = 31$ mV, hence MI = 8%.

Figure 5.25: ASK output with different MIs. Extracted from DSO.

5.4 Power Amplifier

The power amplifier is necessary to enforce the robustness of the RF signal. More precisely, the power amplifier serves: i) to buffer the VCO of the PLL from external elements, and ii) to amplify the phase-locked signal. Important aspects of the PA are related to:

- **Interference.** The power amplifier has to be as linear as possible in both amplitude and phase, to avoid channel interference.
- **Maximum Power.** To maximize the power transfer, the power amplifier is designed to deliver a specific amount of power into the load, ensuring the highest efficiency.
- **Power consumption.** The power amplifier has to be as efficient as possible to minimize the power consumption.
- **Gain.** The gain has to be as much as possible independent of input level and the environment influences.

The possible combinations of these characteristics and the bias condition distinguish primarily the different classes of PAs. The bias condition Q is the specific point - defined by voltage and current - to set the appropriate operating point's PA. The traditional classes are:

- **Class-A.** It is mostly used since it is considered quasi-linear and always ON. It is characterized by optimum linearity and a high gain but low efficiency.
- **Class-B.** It is the least used, and the device is ON exactly 50% of the time. Furthermore, it is good for variable envelop signal at the expense of 6 dB gain penalty and poor linearity.
- **Class-C.** It is ON less than 50% of the time, characterized by a good efficiency but large gain penalty.

The bias point Q varies, moving from one class configuration to another. In particular, moving from a higher class to a lower one, the bias point Q decreases, reducing the power statically dissipated P_{DC} and increasing the efficiency η at the expense of a worsening of linearity and a reduction of gain.

In the case of IMDs, the class-E power transmitter is widely used ensuring the highest efficiency and power transfer. It amplifies the input signal to a proper power level. Key parameters in PA design are the power efficiency η , and the optimization of Power-Added Efficiency (PAE) [87] defined as (5.19) and (5.20):

$$\eta \triangleq \frac{P_{OUT}(f_0)}{P_{DC}} \quad (5.19)$$

$$PAE = \frac{P_{OUT}(f_0) - P_{IN}(f_0)}{P_{DC}} \quad (5.20)$$

where P_{OUT} is the PA's output power evaluated at the operating frequency f_0 .

The class-E power amplifier is mostly used in biomedical telemetry systems, such as brain implant and neural signals detection, due to its simple design, high power transmission [88], and its reduction of power consumption because it substitutes the presence of a mixer [89]. It is optimized for power signals [90].

Figure 5.26 shows the class-E power amplifier's circuit. The transistor M_1 acts as a switch, piloted by the sine wave signal from the oscillator followed by the PLL. The circuit presents the inductor choke L_{RFC} , which behaves like a constant current source in DC characterized by a large impedance at f_0 . Therefore, when the transistor M_1 is turned on, the L_{RFC} is shorted between supply voltage and

ground. This ensures gain in energy from V_{DD} . On the other hand, L_{RFC} injects the gained energy in the previous phase into the load network when it is turned off [91].

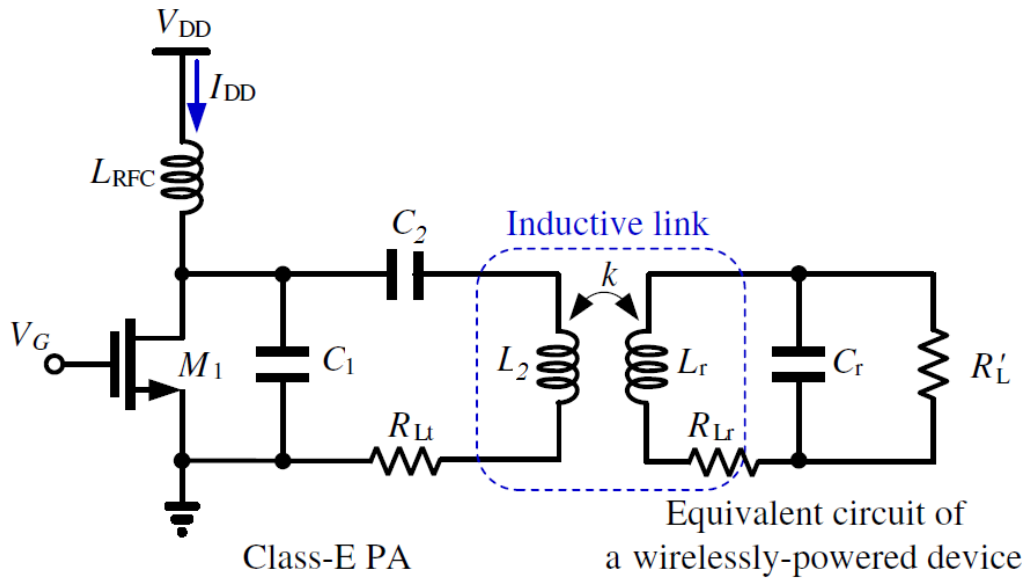


Figure 5.26: Basic schematic of a class-E power amplifier driving an IPT link. Figure extracted from [91].

The capacitor’s values C_1 and C_2 and the value of the transmitting inductor L_2 are chosen in the properly tuned function.

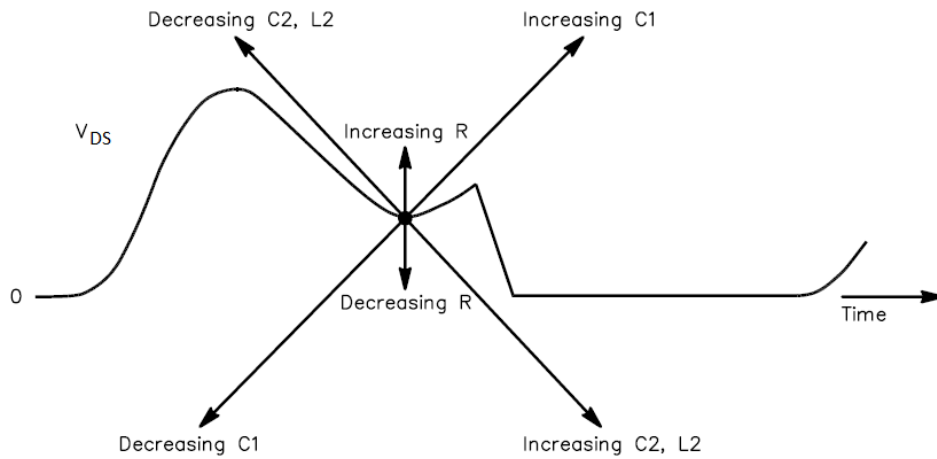


Figure 5.27: Description of the effects of adjusting load-network components C_1 , C_2 and L_2 on V_{DS} waveform. Reprinted from [92].

The effects of adjusting load-network components are susceptible since a slight variation in the value of one of these causes a large variation in the output signal [92]. These considerations are confirmed from the ASK simulations in Figure 5.19 of Section 5.3.1. Figure 5.27 and Figure 5.28 show how small variations of design affect the V_{DS} waveform of the transistor M_1 .

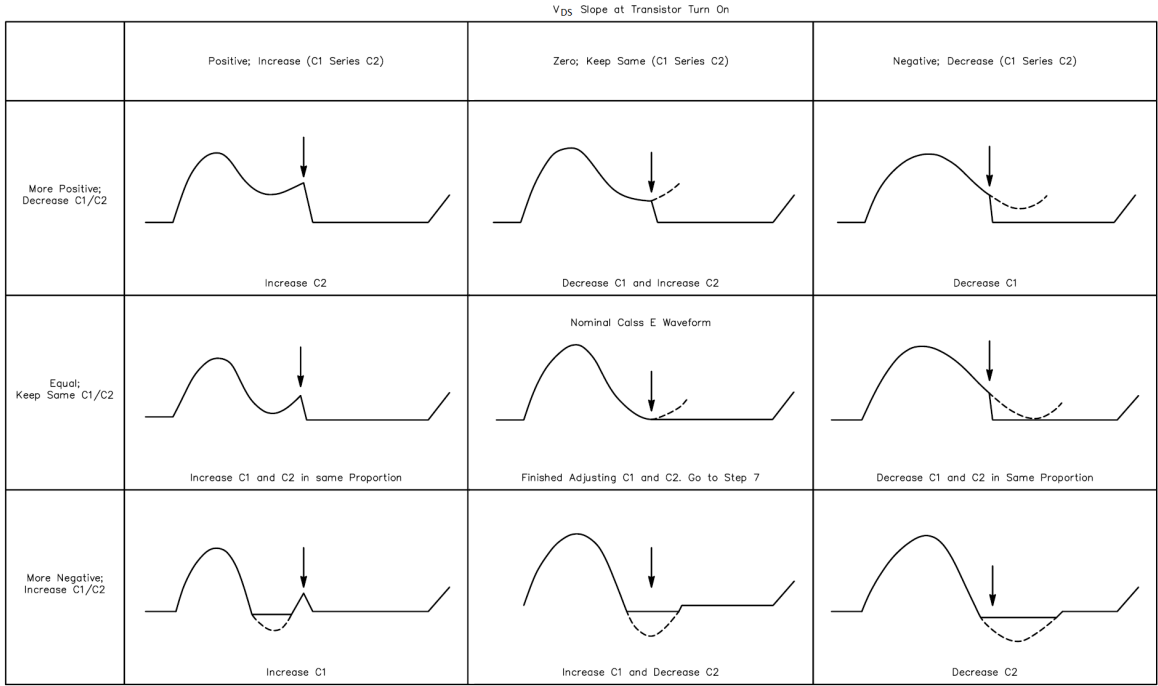


Figure 5.28: Detailed description of the effects of adjustment procedure of the C_1 and C_2 components on V_{DS} waveform. The vertical arrow represents the transistor M_1 turn-on. Reprinted from [92].

5.4.1 PA Design Procedure

This section reports the procedure to design PA, obtaining the values of the schematic of class-E PA shown in Figure 5.26. Starting from the carrier frequency RF_o and the supply voltage V_{DD} , the proper PA design follows [93].

Since L_{RFC} has no resistance characterizes, therefore assumed ideal, the supply voltage V_{DD} must be equivalent to the average of the voltage across the shunt capacitor C_1 (i.e. V_C). This produces the first design relationship as (5.21):

$$V_{DD} = \frac{1}{2\pi} \int_{\pi}^{2\pi} V_C(\omega_c t) d(\omega_c t) = \frac{I_0}{\pi \omega_c C_1} \quad (5.21)$$

where, ω_c is the resonant frequency and I_0 is the current derived by (5.22), known the power load P_{LOAD} and the supply voltage V_{DD} :

$$I_0 = \frac{P_{LOAD}}{V_{DD}} \quad (5.22)$$

Substituting I_0 in (5.21), the shunt capacitor C_1 is extracted. The load resistance R_L placed before L-match, generally characterized by a low value, is:

$$R_L = \frac{8V_{DD}^2}{(\pi^2 + 4) \cdot P_{LOAD}} \quad (5.23)$$

The series capacitor C_2 is extracted by (5.24):

$$C_2 = \frac{1}{Q \omega_c R_L} \quad (5.24)$$

Finally, the design of L_{RFC} is at least an order of magnitude higher than the R_L in order not to be self-resonant at the first harmonics. The reduction of its values increases the AC power losses due to core losses and the skin effect. Therefore, to minimize these effects, L_{RFC} is required more extensive than three times of the transmitting inductor L_2 [93].

The class-E power amplifier results to be susceptible to the inductive parameters of the transmission (e.g. Tx and Rx inductances, matching networks, penetration depth), being critical in the case of multiple freestanding implants. The class-E PA is generally selected for power signals due to several advantages: simple design, high power transmission, low power consumption, and highest efficiency [87]. On the other side, it is susceptible to adjusting load-network components: a slight network variation causes a considerable variation in the powering signal. This condition finally leads to a sensitive Tx system which may cause poor robustness to noise. In the case of wirelessly powered IMDs, most design constrains came from the implant side. Therefore, the Tx side's efficiency may be sacrificed for a more robust and insensitive base station. Moreover, in a distributed network of miniaturised implant, each powering transmission line (from the common Tx front-end to the single receiver back-end) has a different impedance. Therefore, the power amplifier needs to be a trade-off between gain, power and linearity. For these reasons, a class-AB PA is used. To summarize, a class-AB PA has been selected to solve the problems related to poor robustness and high susceptibility to adjusting load-network components.

5.4.2 PA Implementation and Analysis

A class-AB PA (i.e. RF5110G by *Qorvo*) characterised for RF applications at the frequency between $150 \div 960$ MHz and internally matched at 50Ω has been used. It is a PA characterised by high-power, high-gain and high-efficiency. Table 5.3 reports its key features and its electrical specifications.

Parameters	Rating
Voltage Supply (V)	$2.8 \div 3.6$
Power Control Voltage V_{APC} (V)	$-0.5 \div +3.0$
Band Frequency Operation (MHz)	$150 \div 950$
DC Supply Current (mA)	2400
RF Input Power (dBm)	+13
Output Power (dBm)	+32
Efficiency (%)	53
Duty Cycle at Max Power (%)	50
Gain at 450 MHz (dBm)	32.5
Efficiency at 450 MHz (%)	50.5
Package Style	QFN, 16-Pin, 3 x 3 mm
Applications	FM Radio 450 MHz

Table 5.3: Key features and electrical specifications of the RF5110G power amplifier. Values extracted from the datasheet provided by *Qorvo* company.

The RF5110G PA is 16-pad 3 x 3 mm lead frame-based (QFN) package. It has been tested though its Evaluation Kit tuned to 900 MHz. Since this work is characterised at 433.92 MHz, Figure 5.29 shows the evaluation board's schematic with components substitution (in red) to shift its resonance in the range $350 \div 450$ MHz band.

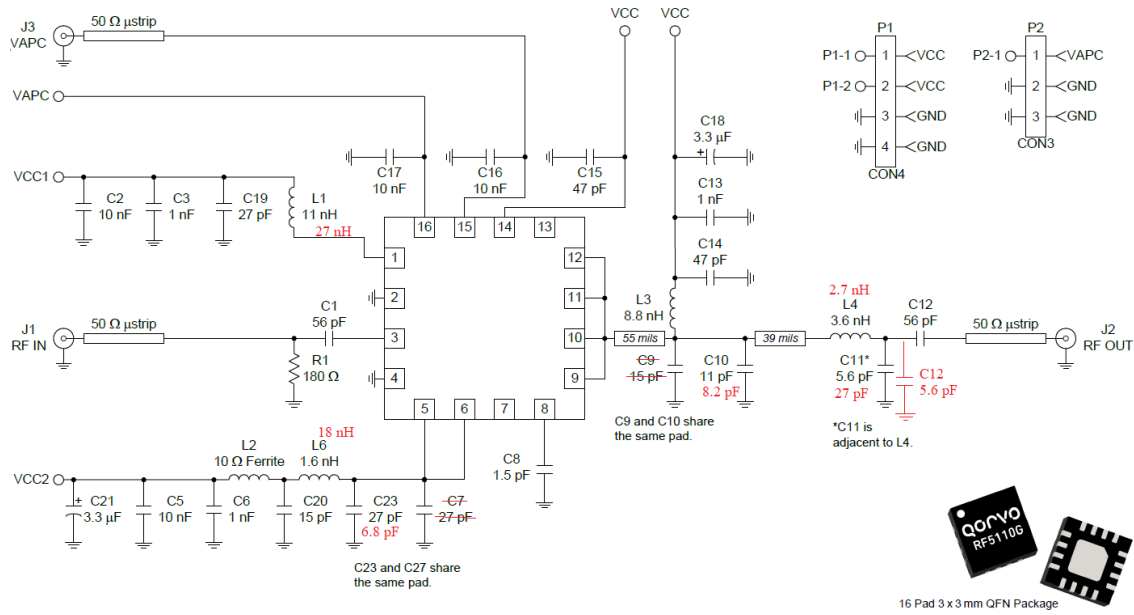


Figure 5.29: Evaluation board schematic at 900 MHz lumped element. The variations of passive component's values are reported in red colour in order to tune the Demo Board in the range 350 to 430 MHz, for $P_{in} = 0$ dBm, $P_{out} \geq 34$ dBm, $V_{CC} = 3.6$ V. Figure extracted from the datasheet provided by Qorvo company.

Instead, Figure 5.30 shows more at a high level the typical test setup.

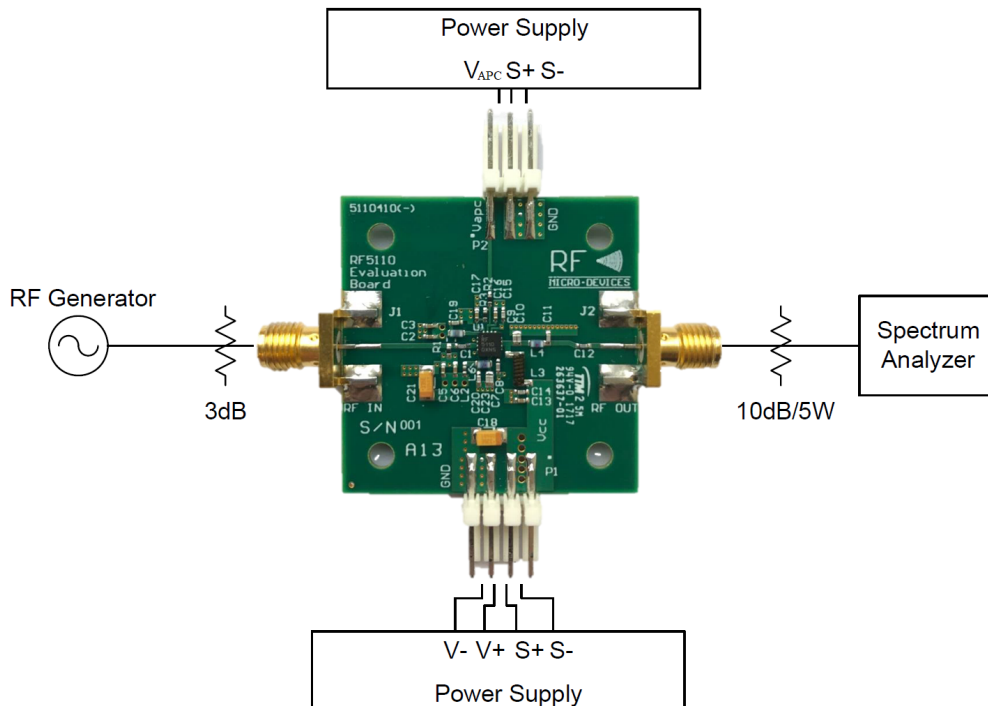


Figure 5.30: Typical test setup with evaluation board PCB information. Figure extracted from the datasheet provided by Qorvo company.

The measurements of the PA has been conducted using coaxial RF cables and Sub-Miniature version A (SMA) connectors. Some connections have been implemented on the breadboard, while an RF Waveform Generator instrument have been used to generate a sine wave at 433.92 MHz. A Signal Analyzer instruments has been used to extract the output power, expressed in dBm. Appendix A.5 reports how to convert dBm quantities in mW quantities.

Moreover, the provided datasheet recommends to include two attenuators. First, the 3 dB attenuator placed in RF_i pad reduces the signal generator's effects since the input impedance variations caused by V_{APC} changes may cause variations of output signal level or frequency. Second, the 10 dB attenuator prevents damages to the Signal Analyzer driven by high powers.

Figure 5.31 reports the Evaluation Kit implemented on breadboard with the two attenuators in RF_i and RF_o . The two voltages are V_{DD} equal to 3.6 V and V_{APC} fixed to 2.8 V.

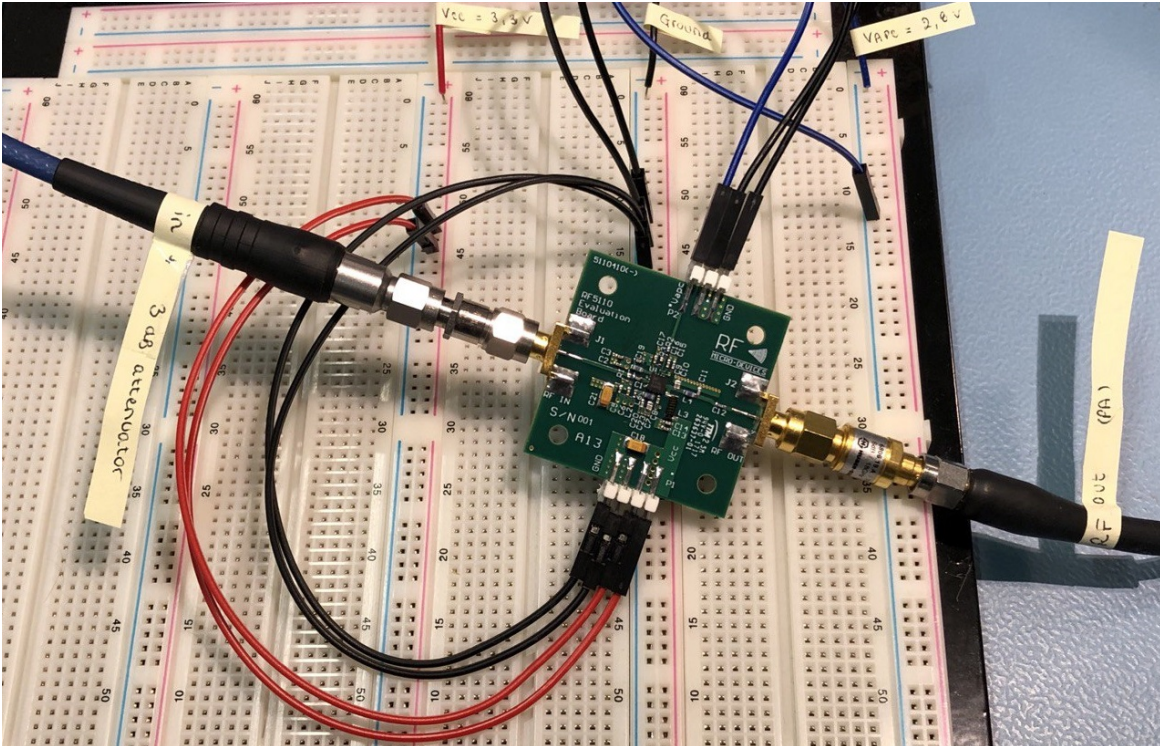


Figure 5.31: Implementation of the Evaluation Kit on breadboard with 3 dB attenuator on the left and the 6 dB attenuator on the right. Presence of jumper wires to power up the Demo Board with the two different voltages. The red wires are V_{DD} , the blue ones are V_{APC} and the black ones are ground.

Figure 5.30 shows the circuit implemented on breadboard. Instead, Table 5.4 reports the characterization of the PA obtained by the testing at 433.92 MHz. The input power P_{in} is set with the Waveform Generator instrument. The output power P_{out} is instead extracted from the Signal Analyzer instrument's display. The gain expressed in dBm is defined as:

$$Gain = 30 + 10 \cdot \log_{10} \left(\frac{P_{out}}{P_{in}} \right) \quad (5.25)$$

where the ratio of the powers is expressed in mV. The current I_{CC} is extracted from the Voltage Generator instrument after setting the current limits declared by the Absolute Maximum Rating (i.e. 2400 mA) issued by the Voltage Generator instrument to avoid permanent damages to the power amplifier. Finally, the PAE is derived by (5.20).

RF_o (MHz)	P_{in} (dBm)	P_{in} (mW)	P_{out} (dBm)	P_{out} (mW)	Gain (dBm)	V_{CC} (V)	V_{APC} (V)	I_{CC} (A)	PAE (%)
433.92	-30	0.0010	-7.50	0.2	22.50	3.3	2.8	0.231	0.02
433.92	-29	0.0013	-6.61	0.2	22.39	3.3	2.8	0.234	0.03
433.92	-28	0.0016	-5.64	0.3	22.36	3.3	2.8	0.235	0.03
433.92	-27	0.0020	-4.65	0.3	22.35	3.3	2.8	0.235	0.04
433.92	-26	0.0025	-3.66	0.4	22.34	3.3	2.8	0.236	0.05
433.92	-25	0.0032	-2.68	0.5	22.32	3.3	2.8	0.236	0.07
433.92	-24	0.0040	-1.70	0.7	22.30	3.3	2.8	0.236	0.09
433.92	-23	0.0050	-0.72	0.8	22.28	3.3	2.8	0.237	0.11
433.92	-22	0.0063	0.28	1.1	22.28	3.3	2.8	0.238	0.13
433.92	-21	0.0079	1.24	1.3	22.24	3.3	2.8	0.239	0.17
433.92	-20	0.0100	2.22	1.7	22.22	3.3	2.8	0.240	0.21
433.92	-19	0.0126	3.20	2.1	22.20	3.3	2.8	0.241	0.26
433.92	-18	0.0158	4.17	2.6	22.17	3.3	2.8	0.244	0.32
433.92	-17	0.0200	5.17	3.3	22.17	3.3	2.8	0.247	0.40
433.92	-16	0.0251	6.12	4.1	22.12	3.3	2.8	0.250	0.49
433.92	-15	0.0316	7.19	5.2	22.19	3.3	2.8	0.256	0.62
433.92	-14	0.0398	8.33	6.8	22.33	3.3	2.8	0.263	0.78
433.92	-13	0.0501	9.22	8.4	22.22	3.3	2.8	0.272	0.93
433.92	-12	0.0631	10.10	10.2	22.10	3.3	2.8	0.283	1.09
433.92	-11	0.0794	10.96	12.5	21.96	3.3	2.8	0.298	1.26
433.92	-10	0.1000	11.78	15.1	21.78	3.3	2.8	0.317	1.43
433.92	-9	0.1259	12.60	18.2	21.6	3.3	2.8	0.341	1.61
433.92	-8	0.1585	13.30	21.4	21.30	3.3	2.8	0.369	1.74
433.92	-7	0.1995	14.20	26.3	21.20	3.3	2.8	0.407	1.94
433.92	-6	0.2512	14.80	30.2	20.80	3.3	2.8	0.446	2.03
433.92	-5	0.3162	14.80	30.2	19.80	3.3	2.8	0.446	2.03
433.92	-4	0.3981	16.10	40.7	20.10	3.3	2.8	0.537	2.28
433.92	-3	0.5012	16.50	44.7	19.50	3.3	2.8	0.589	2.27
433.92	-2	0.6310	17.00	50.1	19.00	3.3	2.8	0.644	2.33
433.92	-1	0.7943	17.00	50.1	18.00	3.3	2.8	0.675	2.21
433.92	0	1.0000	16.90	49.0	16.90	3.3	2.8	0.732	1.99
433.92	1	1.2589	16.60	45.7	15.60	3.3	2.8	0.793	1.70
433.92	2	1.5849	16.20	41.7	14.20	3.3	2.8	0.854	1.42
433.92	3	1.9953	15.70	37.2	12.70	3.3	2.8	0.915	1.16
433.92	4	2.5119	15.10	32.4	11.10	3.3	2.8	0.974	0.93
433.92	5	3.1623	14.50	28.2	9.50	3.3	2.8	1.030	0.74
433.92	6	3.9811	13.90	24.5	7.90	3.3	2.8	1.088	0.57
433.92	7	5.0119	13.30	21.4	6.30	3.3	2.8	1.138	0.44

Table 5.4: Experimental values extracted in laboratory with evaluation board.

Although the used evaluation kit is not tuned to the right frequency of 430 MHz, it provides output up to 50 mV when $P_{in} = -2$ dBm, ensuring the highest PAE equal to 2.33%. The low values of PAE are justified by not correct tuning in terms of frequency. Finally, the value of gain remains constant up to $P_{in} = -12$ dBm.

The values in Table 5.4 can be considered reliable up to $P_{in} = -12$ dBm, guaranteeing an amplification in terms of power guaranteed by the PA of about +22 dBm.

The datasheet declares that with the right tuning at 430 MHz, it is possible to obtain the gain and PAE behaviour, as in Figure 5.32. A reasonable working point is for P_{out} equal to 32 dBm, obtaining: $Gain = 41$ dBm and $PAE = 38\%$. The Matlab code generated to obtain the following graph is reported in Appendix A.3.

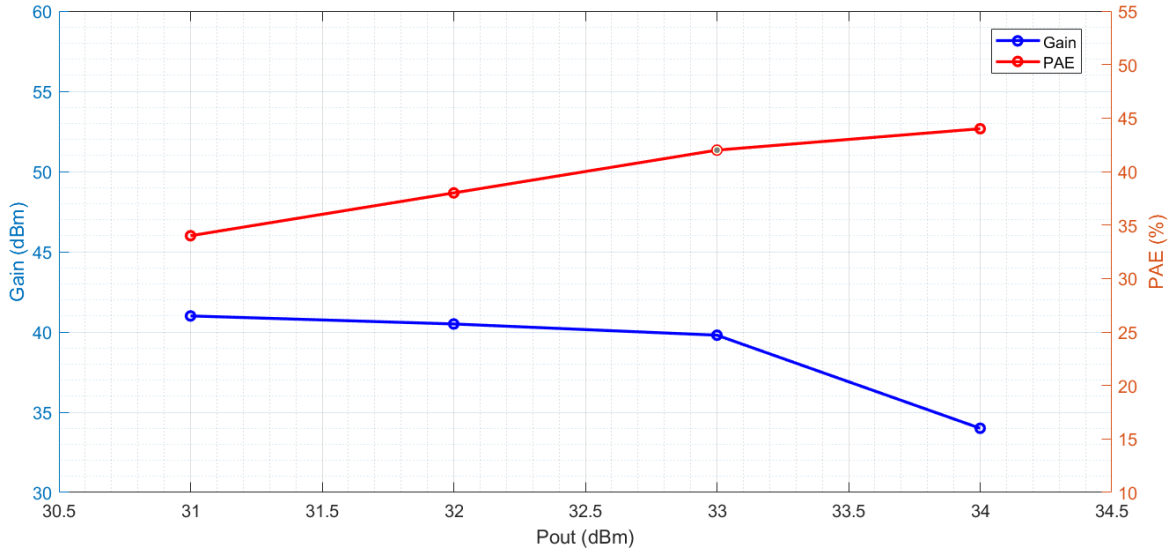


Figure 5.32: Qualitative gain and PAE behaviour vs P_{out} at 430 MHz. Graphs derived from values declared in the Qorvo RF5110 PA's datasheet.

Figure 5.33 shows the testbench of the PA. The value of currents and powers are estimated with R_{load} equal to 50Ω fixed by the DSO. Therefore, $I_1 = 252 \text{ mA}$, $I_2 = 250.17 \text{ mA}$, $I_3 = 1.83 \text{ mA}$, $V_{DD} = 3.3 \text{ V}$, $V_{out} = 260 \text{ mV}_{pp}$, $P_{in} = -30 \text{ dBm} = 1 \mu\text{W}$, $P_{out} = -8 \text{ dBm} = 170 \mu\text{W}$. The calculated amplification of the PA is $+22 \text{ dBm}$ as expected. The measured P_{out} extracted with the spectrum analyzer is -8.48 dBm .

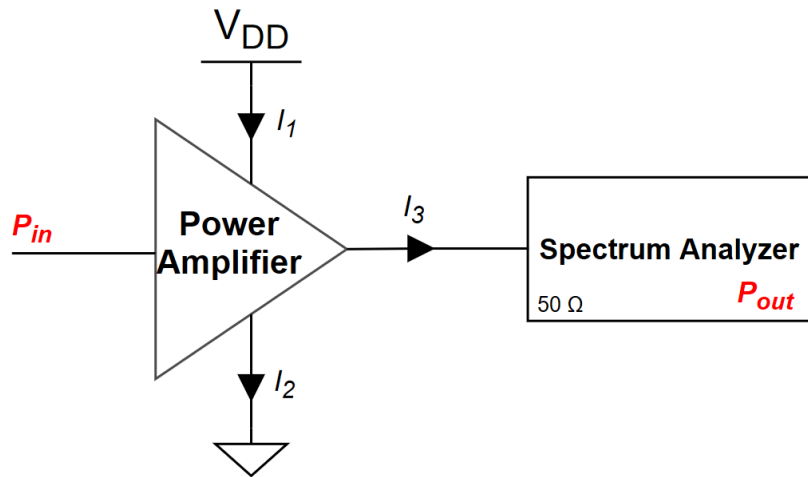


Figure 5.33: Testbench of PA.

The dissipated power of the PA is 825.6 mW . The measured value of P_{out} is verified with the spectrum analyzer. Figure 5.34 shows the peak of frequency at center frequency of 433.92 MHz , with a span of 25 kHz where it is possible to note the P_{out} equal to -8.48 dBm when P_{in} is fixed to -30 dBm .

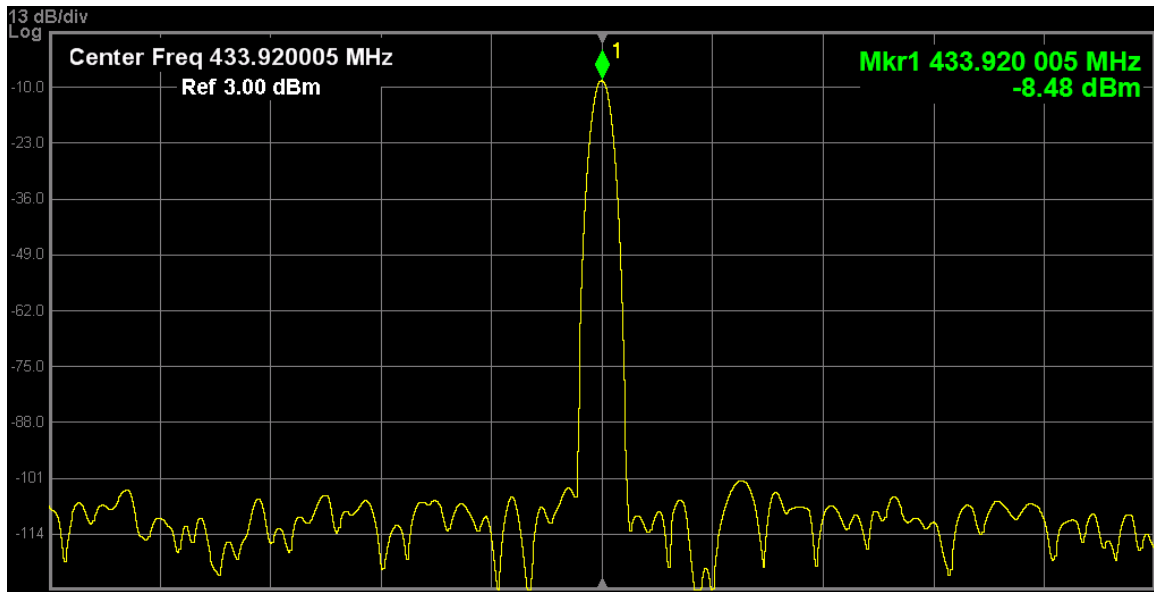


Figure 5.34: Display of the Signal Analyzer instrument. Peak of frequency at 433.92 MHz when the input power P_{in} is fixed to -30 dBm.

5.5 Transmitting Coil

The most appropriate solution for this proposed application and several biomedical neural systems is the wireless power transfer method. Nowadays, many papers describe in detail the methodologies to design and optimize the WPT for biomedical applications, exploiting the inductive power transfer. One of the most relevant parameter to ensure an efficient power transmission is the frequency choice described in Chapter 4. Other important parameters are fundamental to the realization of an optimal design. These are the tissue loss constrained, and the choice of the coil geometries [94]. Regarding the latter, several factors are taken into account, such as the width w , the internal diameter d_i , the external diameter d_o , the thickness t , the number of turns N of both the transmitting and receiving coils and the distance at which these are placed, the load resistance R_L and mutual inductance M . The Tx-Rx distance influences strongly the transmission efficiency since the latter is inversely proportional to the distance with a factor d^6 . Moreover, the shape influences the power efficiency and, in general, the square spiral coil maximizes the power transfer area [95]. Finally, the capacitance C_1 and C_2 , related to the transmitting and receiver side, are used to tune the inductive power link at the proper Self-Resonant Frequency (SRF), which depends on the coil geometries and the surrounding material. For instance, human body tissues are ameliorative in terms of frequency but not in terms of amplitude. The SRF is a crucial parameter for coils used in inductive power transfer links. The inductor's SRF is the particular frequency at which the quality factor Q become equal to zero, and the coil behaves like a resistor of high impedance (i.e. open circuit). The point where this happens is:

$$SRF = \frac{1}{2\pi\sqrt{LC}} \quad (5.26)$$

The coil behaves like an inductor up to SRF. Above this value, the coil attenuates the signal near the SRF due to its high impedance. The coils' design strongly influences the SRF. In particular, if the SRF is lower than the operating frequency, losses in efficiency may occur. Therefore, implanted coils have strict geometry limitations.

Regarding the receiving coil, it is the only one that has technological limits due to the design specs in terms of area and absorption of tissues and related to the photolithography process steps imposed by the Foundry TSMC. In particular,

- **Width.** The minimum width imposed by the Foundry is $2 \mu\text{m}$.
- **Technological node.** Photolithography process depends on the chosen technological node.
- **Thickness.** It is related to the imposed width with the following relation:

$$t \simeq \frac{w}{2} \quad (5.27)$$

- **Absorption of tissues.** The design in respect of the SAR is crucial for the receiving coil since implanted.
- **Capacitor.** For the receiving side, the matching capacitor's size is the main limitation since its high value may occupy a too much quantity of availability area, which is not possible for this application due to the challenging physical dimensions of the implanted neural system.

5.5.1 Coil Design Procedure

Coils are classified in two main classes: Wire-Wound Coils (WWCs) [96] and Planar Spiral Coils (PSCs) [97]. WWCs are characterised by an high quality factor than PSCs. On the other hand, PSC has high reliability, and are compatible with μ -fabrication processes. Figure 5.35 shows some variants for the coil design with their main key parameters.

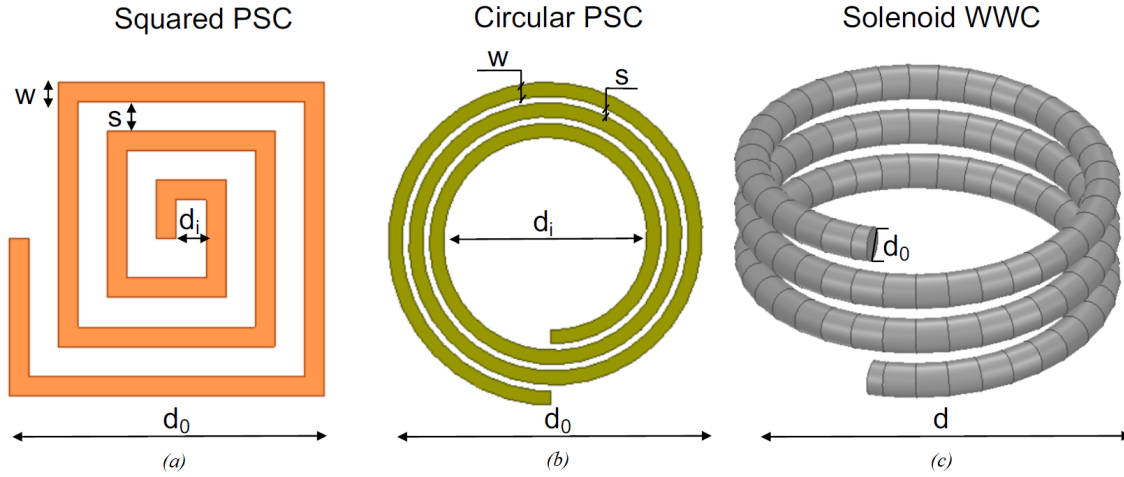


Figure 5.35: Variants for the coil design. (a) squared PSC; (b) circular PSC; (c) solenoid WWC. Reprinted from [37].

Different design for resonant inductive links have been presented [98]. In particular, Figure 5.36 reports the both series and parallel LC-resonant-tank configurations [99].

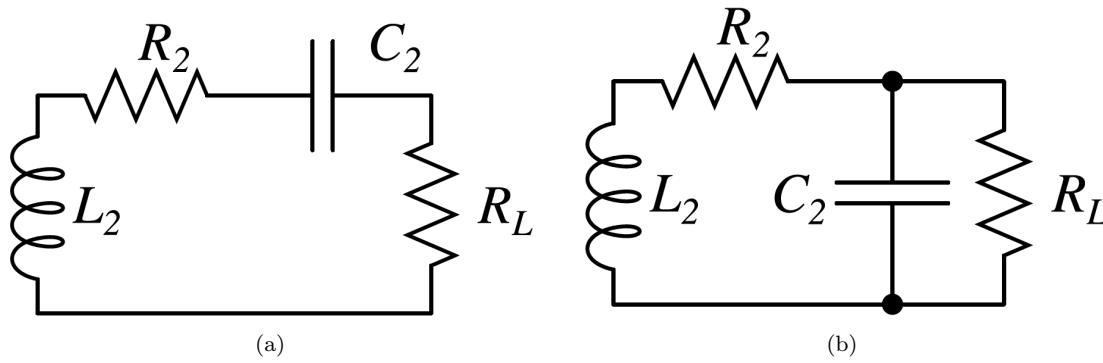


Figure 5.36: Equivalent circuit for an inductive link with (a) series and (b) parallel-resonant cases. Reprinted from [99].

5.5.2 Coils Design and Simulation

In the case of 3-coils IPT systems for multiple miniaturised implants, the resonator diameter d_{Res} is selected from the area of coverage, which is always application-constrained. Then, the optimal Tx diameter d_{Tx} that will maximise the magnetic coupling with the resonator is calculated as [100]:

$$d_{Tx} = \sqrt{d_{Res}^2 + 4 \cdot d_{12}^2} \quad (5.28)$$

where d_{12} is the Tx-resonator distance. In particular, $d_{Tx} \simeq 40 \text{ mm}$ for a $d_{Res} = 10 \text{ mm}$ and a $d_{12} = 20 \text{ mm}$, reasonable values for thousands of sub-mm neural implants. Therefore, the Tx coil is characterized by one turn of 40 mm of diameter and $500 \mu\text{m}^2$ of section, realized in copper (Cu). The simulations are realized on Ansys HFSS software [101].

The coil has to be placed on a thin substrate of glass-reinforced epoxy laminate material, known as FR4. Moreover, the whole structure has been incorporated in a wide air-box, which defines the working

volume. The air-box surface is used to define the boundary conditions which cancel both electric field \mathcal{E} and magnetic field \mathcal{H} at the boundary, avoiding reflections. Figure 5.37 shows the Ansys HFSS design model of the Tx coil.

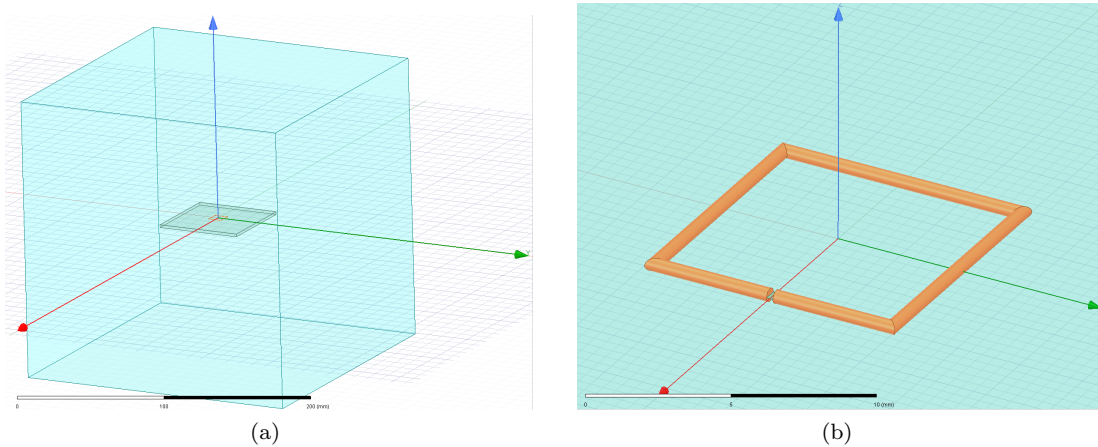


Figure 5.37: HFSS design model. (a) Transmitting coil. (b) Close up view.

Figure 5.38 shows the project manager. In the left column, all steps to set for the simulation are shown. The steps to define the solid model are described on the right column. In this regard, the three main blocks are: the airbox, the Cu transmitting coil and the FR4 substrate. Moreover, a sheet with a lumped port of $50\ \Omega$ defines the port excitation.

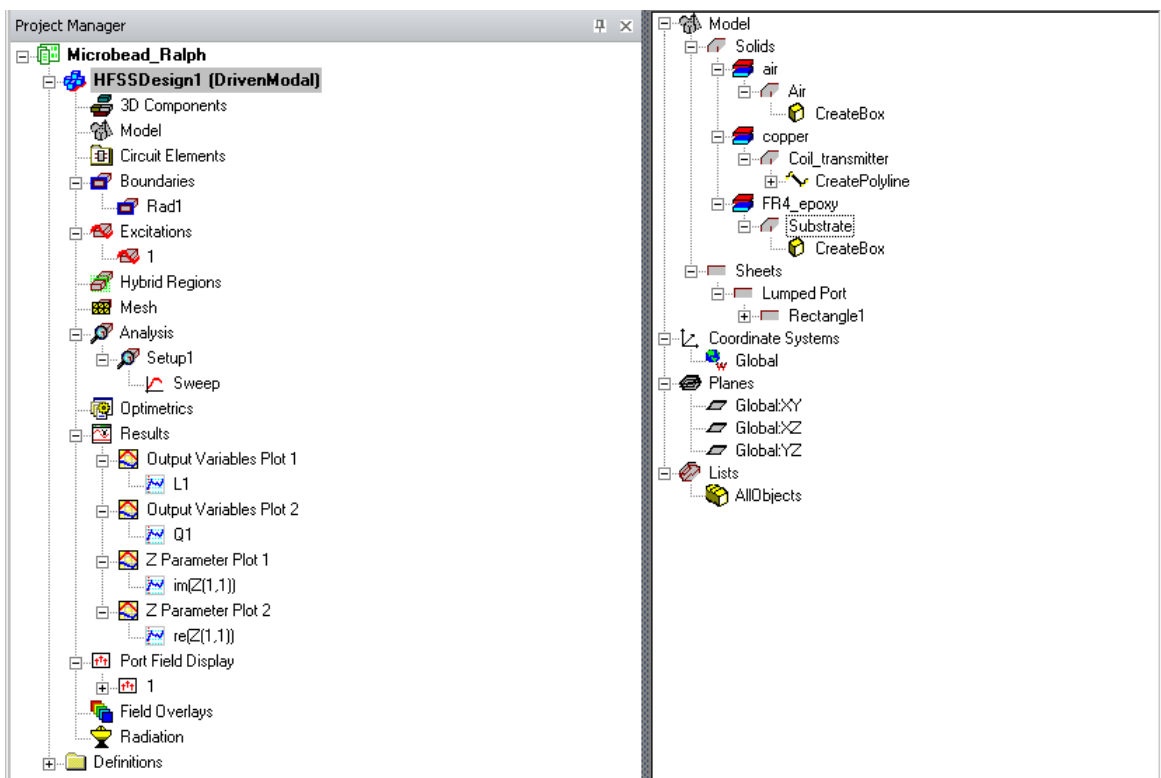


Figure 5.38: Ansys HFSS project manager of the transmitting coil.

Since the Tx and Rx coils may have different SRFs, the critical aspect is their matching. The trade-off is given by the transmission and receiving efficiencies. In particular, the risk is to have: i) at low frequency, a suitable transmitter but a low ability to receive the data at the receiving end, and ii) at high frequency, a suitable receiver but low ability to transmit the data from the transmitting end. An intervention on the quality factors Q is required to match the two curves.

The quality factor is defined in (5.29) as the absolute value of the ratio between the imaginary part and the real part of the admittance:

$$Q_i = \left| \frac{\Im \{Y_i\}}{\Re \{Y_i\}} \right| \quad (5.29)$$

where $\Im \{Y_i\}$ and $\Re \{Y_i\}$ are the imaginary and real parts of the admittance.

As a matter of fact, Q is also dependent on the mutual inductance M_{12} , which depends on the distance between Tx and Rx coils and their geometries through an elliptic integral [37]. Using an equivalent two ports network (e.g. from the Ansys HFSS point of view), the mutual inductance can be defined as (5.30):

$$M_{12} = \frac{1}{2\pi f \cdot \Im \{Z_{21}\}} \quad (5.30)$$

where $\Im \{Z_{21}\}$ is the imaginary parts of the impedance. Figure 5.39 shows the quality factor of the coil.

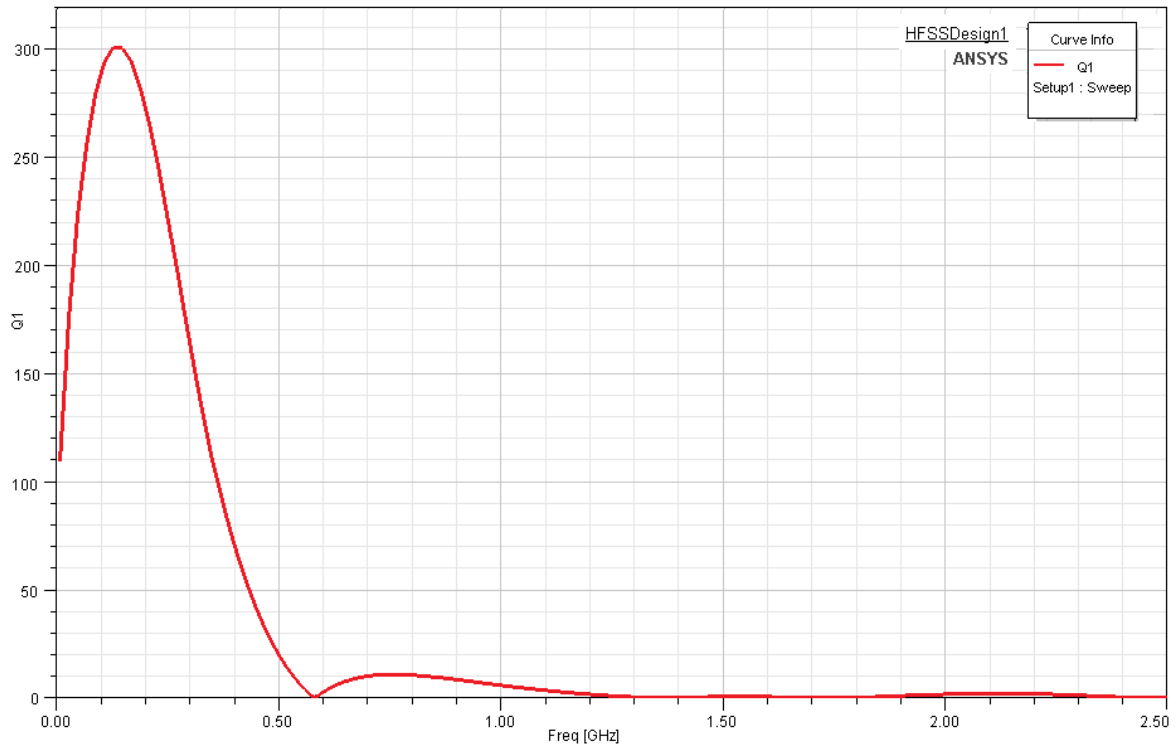


Figure 5.39: Ansys HFSS simulation. Quality factor Q of the Tx coil with $d_{Tx} = 40$ mm.

The value of the series inductor L_s is extracted as:

$$L_s = \frac{\Im \{Z_s\}}{2\pi f} \quad (5.31)$$

Figure 5.40-a shows the impedance's imaginary part $\Im\{Z_1\}$ for the Tx coil, which represent the Tx L_s . L_s is important since is the starting point to calculate the required matching capacitor C_{match} of the LC-tank to resonate at the working frequency. C_{match} can be calculated as follows:

$$C_{match} = \frac{1}{2\pi f \cdot L_s} \quad (5.32)$$

Another important parameter is the series resistance R_s of the coil, which has to minimized inasmuch it represents the loss resistance. The series resistance R_s is defined in (5.33) as the real part of series impedance $\Re\{Z_s\}$, as in Figure 5.40-b.

$$R_s = \Re\{Z_s\} \quad (5.33)$$

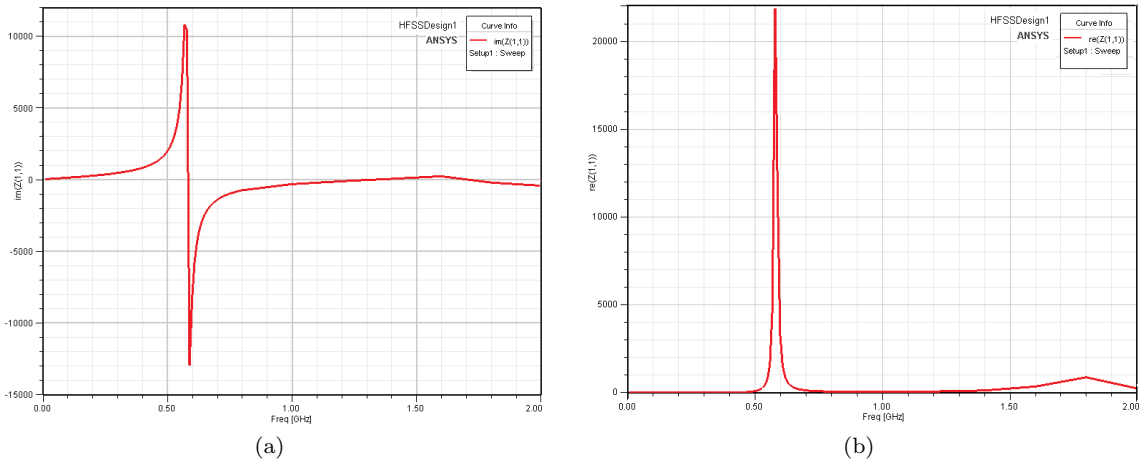


Figure 5.40: Ansys HFSS simulation of the Tx coil with $d_{Tx} = 40$ mm. (a) Series inductor L_s ; (b) Series resistance R_s .

Finally, the PTE and PDL are calculated by (3.5) and (3.6).

5.5.3 Coils Measurements

To test the transmitter and the IPT link, the Tx and Rx coils are realized by hand using: i) the copper wires with a circular section, ii) the FR4 substrates, and iii) SMA connectors. For the sake of simplicity, the Rx coil is identical to the Tx coil. Figure 5.41 shows the implemented coils. The Tx and Rx coils are realized in a square shape, welded to the SMA connector and placed on the FR4 epoxy resin substrate [102]. A Vector Network Analyzer (VNA) is used for the measurements of the coils.

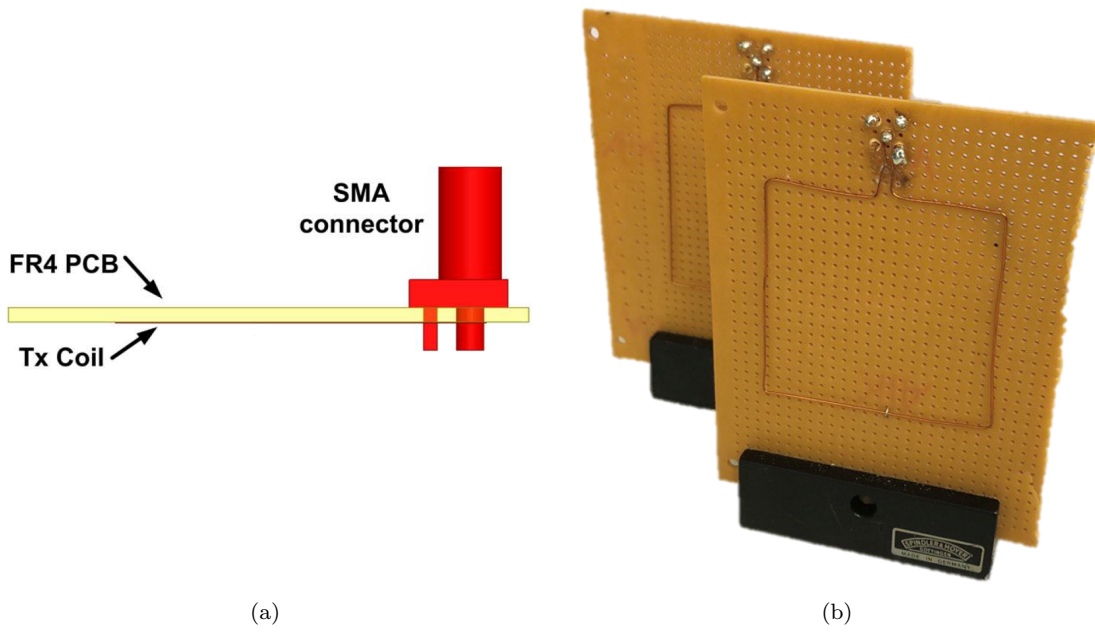


Figure 5.41: Coils implementation. (a) Conceptual front view of the coil, reprinted from [102]. (b) Tx and Rx coils realized on FR4 substrate.

Instead, Figure 5.42 shows the measurements of the obtained R_s (red) and L_s (blue) extracted by the VNA instrument.

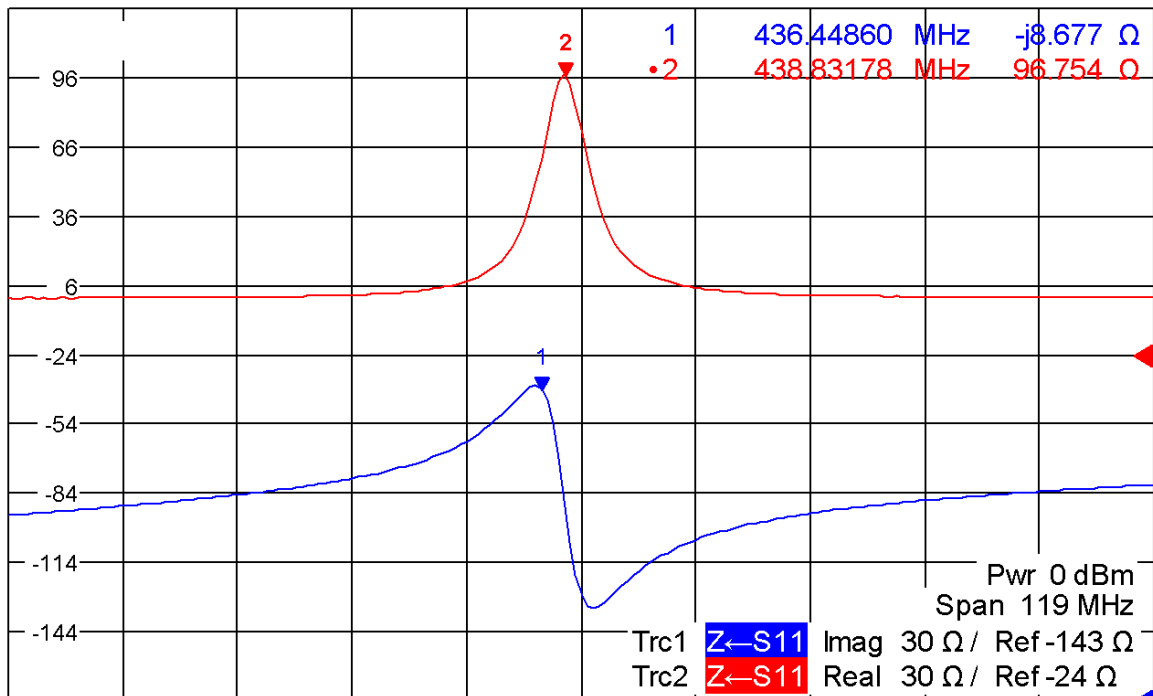


Figure 5.42: VNA measurements of the Tx coil with $d_{Tx} = 40$ mm. Series inductor L_s (Trace 2); Series resistance R_s (Trace 1).

At 433.92 MHz, the number of Tx turns is mainly limited by the SRF. A single turn Tx coil is selected to restrict the SRF degradation. As a result, the return loss S_{11} simulated on Ansys HFSS and measured with VNA instrument of the realized squared Tx coil is shown in Figure 5.43 to compare the two trends. The graph is implemented on Matlab, and its code is reported in Appendix A.6.

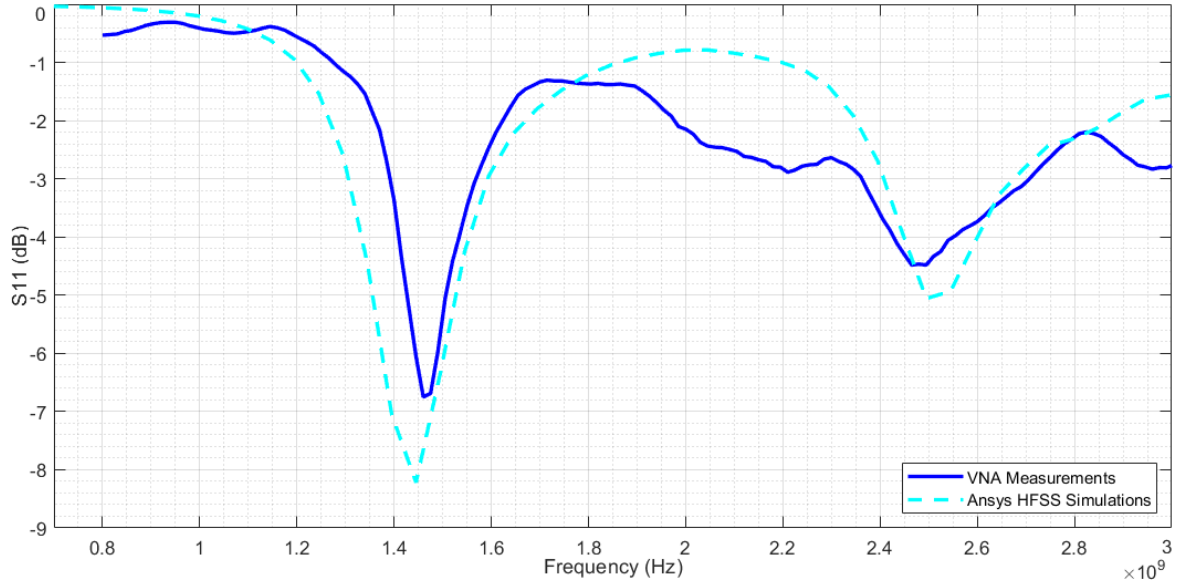


Figure 5.43: S_{11} (dB) vs Frequency (Hz). VNA measurement in blue and Ansys HFSS in light blue.

The two curves are pretty similar. The two SRF peaks almost coincide both in frequency and in amplitude (i.e. $SRF \simeq 1.43$ GHz and $S_{11} \simeq -7$ dB). The coarse Tx and Rx coil, realized by hand and soldered roughly, can justify these slight variations. Moreover, Ansys HFSS simulations do not consider the effects due to cables, welding and SMA connector. Two SRFs are present. The first one is around 1.42 GHz; the second one is around 2.42 GHz but smaller. As expected, the SRF (i.e. 1.42 GHz) is three or four times higher than the operating frequency (i.e. 433.92 MHz) [103]. This is favourable to minimize the losses and to ensure a high-quality factor at the operating frequency.

Chapter 6

Results and Discussion

This section describes the results of the RF SWIPT system. Each electric component has been tested individually, up to recompose the entire transmitting chain.

Figure 6.1 and 6.2 show the TB and the final result of the study respectively. The measured output of the PA highlights the ASK modulation performed with a MI of 8%. 14.8 and 14.4 dBm are respectively measured for the "high" and "low" states of the RF SWIPT system for an P_{RF_i} of -30 dBm. The green square wave is the digital input data D_{in} that pilots the switch SW of the ASK modulator. Instead, the blue sine wave is the output modulated signal RF_o received by the Rx coil connected to the DSO.

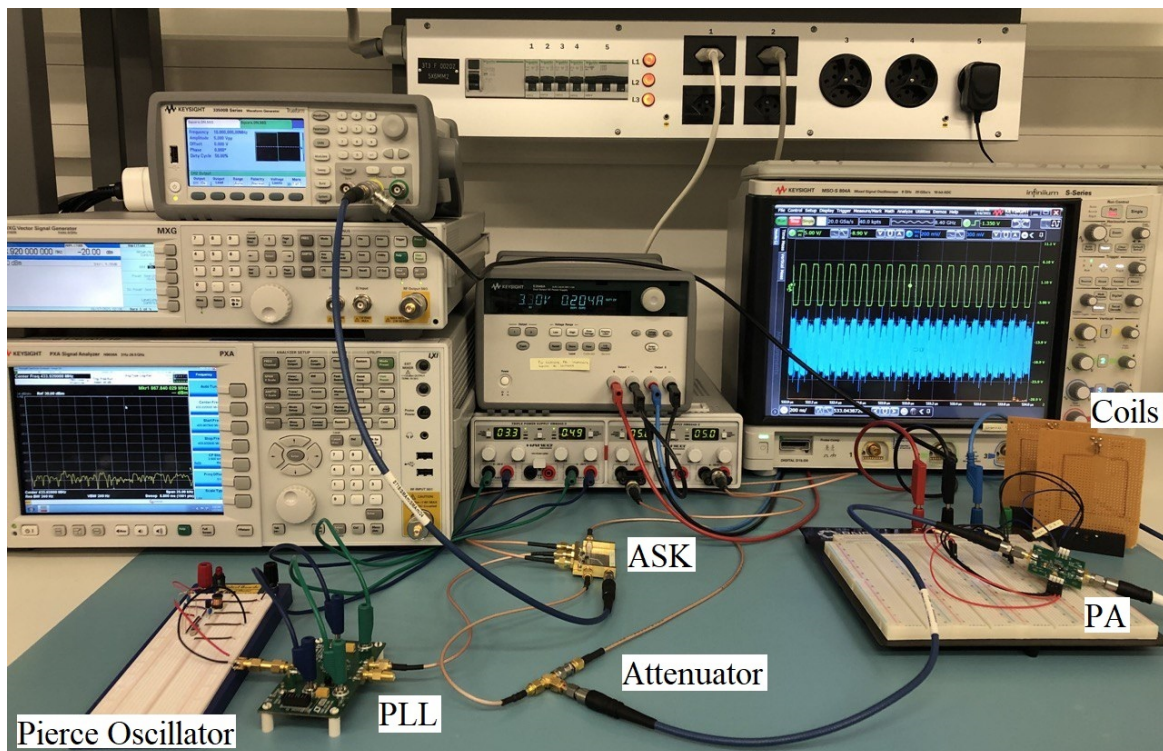


Figure 6.1: Testbench of the RF ASK transmitter.



Figure 6.2: Measurement of the RF ASK transmitter.

Figure 6.3 reports the study's final result characterized by a random string of bits in the input. The Waveform Generator generates the latter.

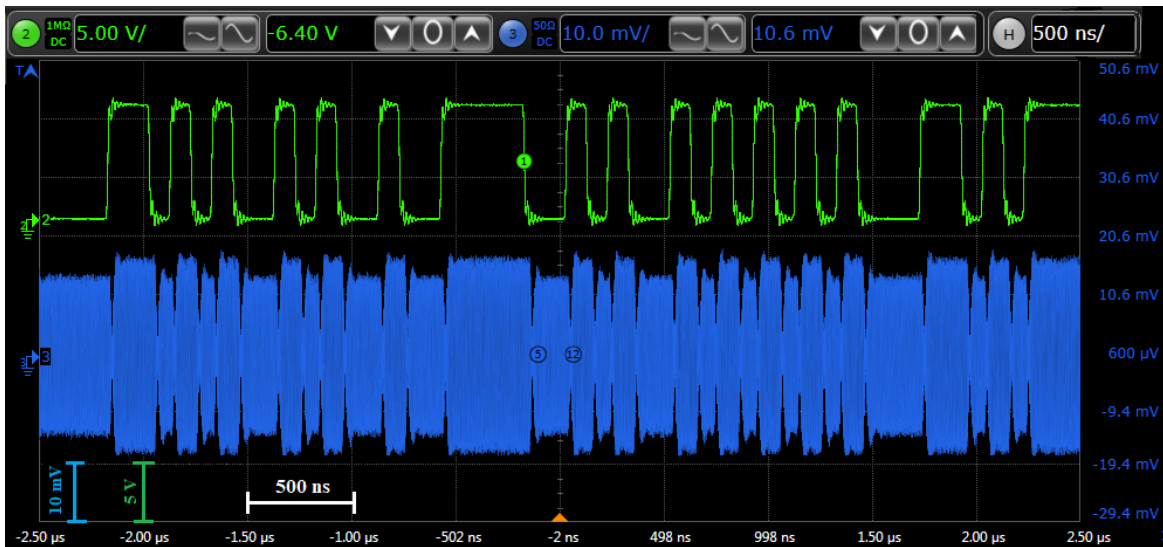


Figure 6.3: Measurement of the RF ASK transmitter with random string of bits in input.

The transition times present some glitches due to the high rising and falling times of the digital waveform generator. These are comparable with the ASK modulator's switching times. In particular, for waveform generator, t_{rise} and t_{fall} are both 8.4 ns. On the other hand, for ASK modulator, t_{rise} and t_{fall} are 3.3 ns and 4.6 ns, respectively. Being of the same order of magnitude, the switch causes therefore glitches. As the data rate increases, the glitches increase, leading to high BER. Figure 6.4

shows some measurements with the design of different MI (i.e. 8%, 17%, 20%) for different data rate (i.e. 10, 20, 40 Mbps). The comparison emerges that a high data rate (i.e. 40 Mbps) leads to high unreliable data transmission because glitches overlook the signal. Therefore, the "high" and "low" states become indistinguishable. A data rate of 20 Mbps is considered enough reliable for the data and power transmission.

From the measurements, a SWIPT transmitter ASK modulated with data rate up to 20 Mbps has been demonstrated. Over 20 Mbps, glitches overlook the signal. Nevertheless, this limit is imposed by the high t_{rise} and t_{fall} of the used digital waveform generator. Therefore, obtaining lower t_{rise} and t_{fall} (i.e. hundreds of ps), a higher data rate can be reached.

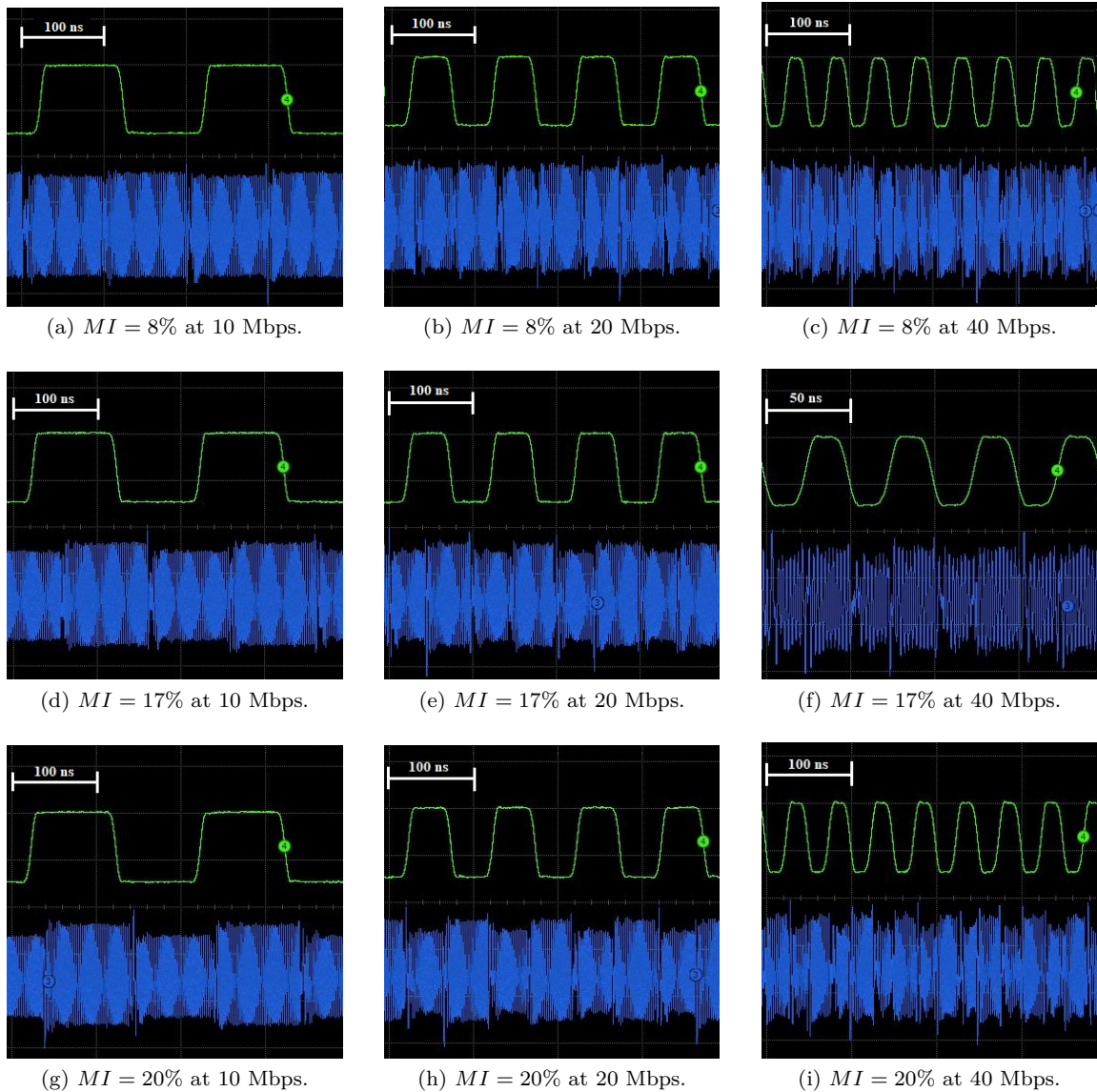


Figure 6.4: Measurements extracted with DSO with different design of MI and data rate.

Table 6.1 compares the RF transmitter with the state-of-the-art, highlighting some relevant parameters in SWIPT systems.

Year, Ref	f_0 (MHz)	Modulation Technique (Downlink)	SWIPT System	Data Rate (Mbps)	P_{out} (dBm)	η (%)	V_{DD} (V)	FoM
2020, [21]	915	PWM-ASK	Yes	1	8	NA	0.6 ÷ 1	0.11
1997, [104]	10	ASK	Yes	0.12	NA	99*	5	0.12
2013, [105]	915	FSK	Yes	1.5	0	18	1.2	0.14
2004, [49]	0.7	ASK	Yes	0.06	17	36	5	0.18
2018, [86]	10	ASK	Yes	1	13.8	42	2.4	0.46
2008, [106]	433	OOK	Yes	10	-12.7	4.5	1	0.62
This work	433	ASK	Yes	20	32	38*	5	0.97
2010, [107]	400	FSK	No	1.25	-2	7	0.5	0.16
2011, [108]	2400	OOK	No	4	7.47	NA	1.8	0.19
2018, [109]	144	OOK	No	33	-4	NA	0.85	1.95
2014, [110]	430	OOK	No	60	-0.37	NA	0.5	2.02

* PA only

Table 6.1: State-of-the-art comparison of RF transmitter on IPT link.

The relation between data rate and the carrier frequency is essential in evaluating the performance of the systems. In this application, a high data rate is required to ensure visual temporal resolution. As a rule of thumb, the data rate may be increased by increasing the carrier frequency, but this leads to a higher SAR and high amplitude attenuation by human tissues. Hence, a high data rate is needed, but with a not too high carrier frequency. In particular, a new Figure of Merit (FoM) is here then proposed, measured in $(\text{Mbps}^2/\text{MHz})^{1/3}$ and defined as:

$$FoM = \sqrt[3]{\frac{DR^2}{f_0}} \quad (6.1)$$

where DR is the data rate, expressed in Mbps, and f_0 is the carrier frequency, expressed in MHz. The FoM is proportional to DR and inversely proportional to f_0 . In (6.1), DR^2 is used instead of DR to highlight its relevance. The cubic root is implemented to obtain significant changes in FoM values between the different transmitters of Table 6.1.

The RF transmitters are listed in increasing order of FoM, organized in SWIPT systems and not. In particular, OOK architectures present the highest FoM due to their simple modulation and demodulation schemes. On the other side, these OOK transmitters are not designed as a SWIPT system since only data transmission has been implemented [109][110]. In the case of miniaturised chips, OOK modulation is critical in providing a stable supply at the implant side if the SWIPT signal is the only source of energy for the implanted neural system due to the completely absence of batteries. As expected, FSK transmitters show low values of FoM since they are not able to achieve high DR. Finally, basing on the new FoM and not considering the transmitters not designed as a SWIPT system, the transmitter proposed in this thesis presents the best performances with respect to similar work previously published. In particular, it shows the highest output power (i.e. $P_{out} = +32$ dBm) and the highest data rate (i.e. $DR = 20$ Mbps). Regarding the efficiency η , the majority of the SWIPT systems exploit a class-E PA, which usually ensures efficiencies higher than 97%. The proposed transmitter has not been implemented on PCB yet. Therefore, the declared efficiency is related only to the class-AB PA (i.e. $\eta = 38\%$).

To conclude, differently from [86], the RF ASK modulation is performed before the amplification stage (as in Figure 5.2), thus obtaining a data rate of 20 Mbps, which is the highest with respect to other similar SWIPT system.

To conclude, Figure 6.5 reports the pie chart of the absorbed power $P_{absorbed}$ of each block of the RF SWIPT system. Its Matlab code is reported in Appendix A.7.

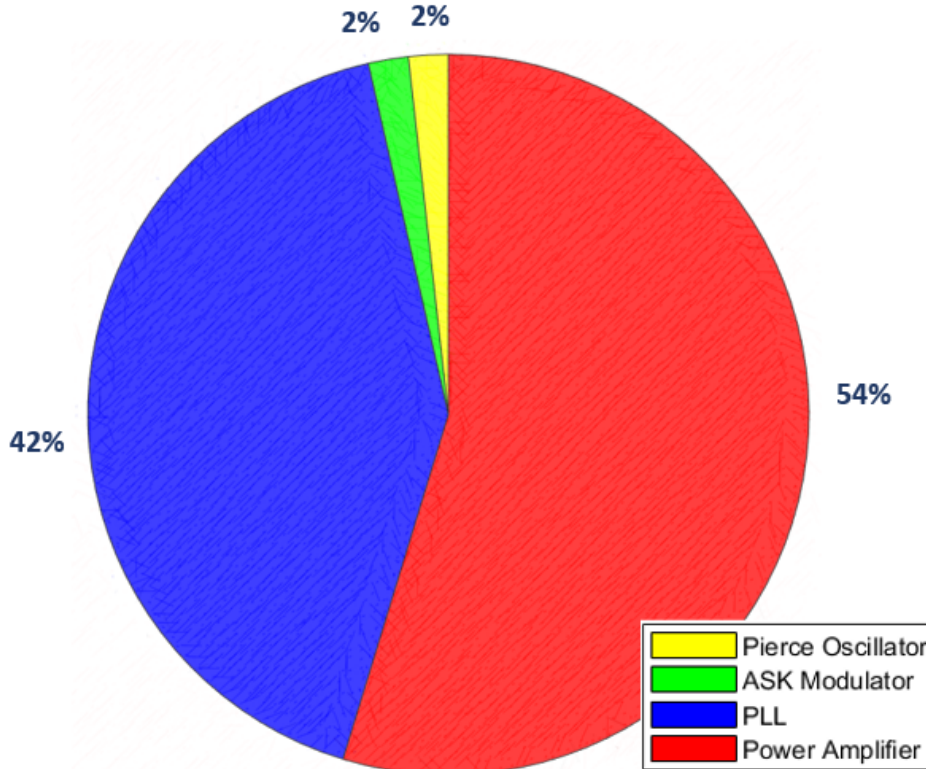


Figure 6.5: Pie chart of $P_{absorbed}$ required by the main blocks of the RF SWIPT transmitter.

The pie graph emerges that PLL and power amplifier require the highest powers. On the other hand, the Pierce Oscillator and ASK modulator require the lowest powers. Table 6.2 reports their absolute values.

Component	$P_{absorbed}$ (mW)
LF Pierce Oscillator	24.8
Phase-locked Loop	582
ASK Modulator	25
Class-AB Power Amplifier	763

Table 6.2: Absolute values of the absorbed power.

6.1 Commercial Integrated RF Transmitter Comparison

Nowadays, the dependence on technology increases with the strong growth in deployment, development and request in many different sectors, such as telecommunication, automotive and industry, up to reach the healthcare sector. In particular, single-chip RF transmitters are present on the market and commercialised. In general, these systems are versatile since they have a programmable output power and a wide range of selectable operating frequency, consuming low power.

Several integrated RF transmitters and modulators are commercialised from different electronic manufacturer, such as Texas Instruments, Micrel, STMicroelectronics (STM), Analog Devices (AD), Maxim,

and Microchip. These are just some of the manufacturers present on the market. For instance, Ibrahim and Mustapha proposed the use of an OOK transmitter IC of Micrel company for remote wireless applications [111]. They propose a frequency range is from 300 to 450 MHz, delivering up to +10 dBm as output power.

Table 6.3 compares the new designed RF SWIPT transmitter with some of the fully integrated transmitters presents nowadays on the market.

Fully Integrated Tx	Manufacturer	Range of Frequency (MHz)	Modulation Technique	Interface	Output Power (dBm)	Data rate (kbps)
MICRF112	Micrel	300 ÷ 450	ASK, FSK	NA	+10	1
MICRF113	Micrel	30 ÷ 450	ASK/OOK	NA	+10	20
ADF7020	AD	431 ÷ 478	ASK, FSK	Serial	+13	64
MAX7044	Maxim	300 ÷ 450	ASK/OOK	I ² C	+13	100
ADF7012	AD	75 ÷ 1000	ASK, OOK	Serial	+10	179.2
MAX41460	Maxim	300 ÷ 960	ASK, FSK	SPI	+16	200
S2-LPTX	STM	413 ÷ 479	ASK, OOK	SPI	+16	500
SPIRIT	STM	387 ÷ 470	ASK, OOK	SPI	+16	500
This work	-	350 ÷ 450	ASK	SPI	+32	20000

Table 6.3: Comparison of fully integrated transmitters present on the market.

Table 6.3 reports the main single-chip RF transmitter selected to have: i) the range of operating frequency containing $RF_i = 433.92$ MHz, ii) ASK modulation technique and iii) the highest achievable data rate. The RF transmitters are listed in increasing order of data rate. The reported fully integrated transmitters show low output power. The highest P_{out} is +16 dBm. The same considerations can be made for the data rate. The highest achievable data rate is hundreds of kbps. In particular, this amount is two orders of magnitude lower than the requested data rate (i.e. up to tens of Mbps). The work described in this thesis results in the best one thanks to its high data rate and high output power: the highest ones if compared with others. In particular, the data rate is two orders of magnitude higher than the highest one, and the output power is double than the highest P_{out} present on the market. It is tuned to work in the range of frequency of $350 \div 450$ MHz due to the design of the class-E PA, and it has an SPI interface for the setting of the PLL's registers.

Future work will include PCB fabrication of the whole RF SWIPT system, including the printed Tx coil. Figure 6.6 reports the electrical schematic of the future PCB realized on Altium Designer software.

Chapter 7

Conclusions

Over the last years, wireless power transfer has shown tremendous advantages for next-generation implantable neural systems. Miniaturisation and large scale distribution are crucial elements for the future of precision medicine and therapy. In particular, wireless power transfer via inductive links has shown promising results in efficiency and robustness.

In particular, a wireless implantable neural system able to restore some form of vision for blind patients is proposed. The primary goal is to stimulate the cortical visual pathway, suggesting a novel approach eliminating transcranial and transcutaneous cables, thus avoiding the onset of infections.

Figure 7.1 shows the central concept of this work. First, the video camera integrated into a pair of glasses records the images that are processed. Second, the external base station transmits power and data to the neural implants simultaneously. Third, the phosphene perception is induced at a precise spatial location once the single CMOS-pixel stimulates the brain. The challenges of the whole proposed implantable system are: i) the strict dimensions of the implanted size, and ii) location of powering and receiving system in the human head. Regarding the circuit level, the presented work focuses on remote powering, analysing the coil inductive link approach's pro and cons. The inductive coupling method is considered the best candidate to face the high distance, ensuring an optimal power delivered to load and an optimal power transmission efficiency. The implanted CMOS-pixels are located at a distance of $18 \div 20$ mm from the surface. Therefore, the data and power signals have to pass through several human layers. The 3-coils inductive link provides the optimal parameters for transmission of power and data. The external base station requires a battery providing about 5 V. On the other hand, the implanted system is battery-less due to the strict constraints in terms of sizes, fixed to $200 \times 200 \times 30 \mu\text{m}^3$.

A novel method that guarantees a high data rate in amplitude-shift keying modulation is developed to provide the implanted system's necessary power. In the experimental work of the present thesis, a novel radio-frequency structure is realised and measured for simultaneous wireless power transfer and downlink data communication. It works at 433.92 MHz, and it is combined with an amplitude-shift keying modulation characterised by a variable modulation index as low as 8% and a data rate as high as 20 Mbps. The strengths and weaknesses of the current state-of-the-art have been analysed. The external radio-frequency base station is composed of quartz, a low frequency Pierce oscillator, a phase-locked loop, an amplitude-shift keying modulator, a class-AB power amplifier and a transmitting coil. Each block of the whole chain has been designed, simulated and tested. A high data rate and low modulation index might enable the implantation of thousands of freestanding and miniaturised neural implants. The final system has been compared with the current state-of-the-art showing one of the highest data rate and transmitted power while maintaining robustness and gain.

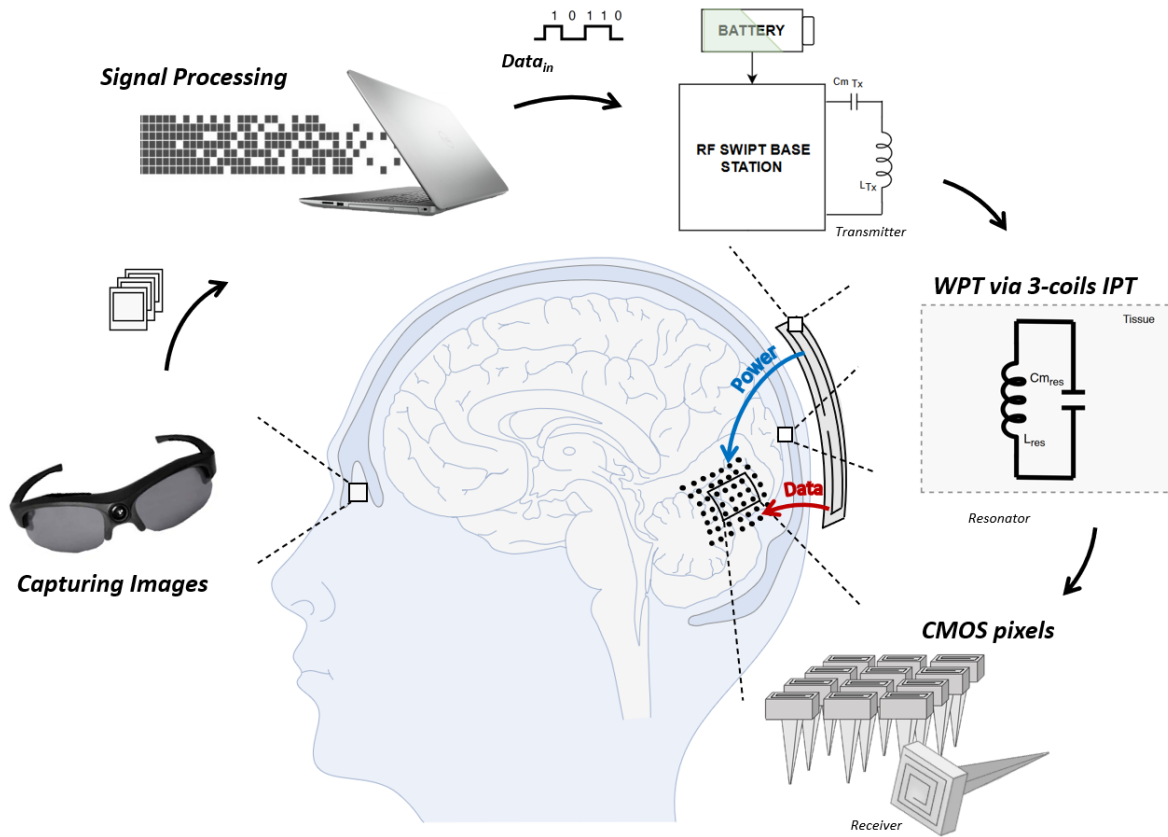


Figure 7.1: Complete system overview of Smart Micro Neural Dust for reverting blindness.

7.1 Future Works

Future work will include printed circuit board fabrication of the whole system, including the printed transmitting coil. The final transmitter will be used to characterise and test the 3-coils inductive link itself with miniaturised receivers.

Although improvements need to be carried out, the proposed neural implant system covers future works and a wide range of medical therapy applications to a substantial fraction of the blind population worldwide. The current developments represent promising progress in the field of visual restorative medicine. Besides cortical visual prosthesis, the same approach can ideally be used in a wide range of medical therapy applications, such as deep brain stimulators [112] for Parkinson's disease, epilepsy, obsessive-compulsive behaviour and addiction; spinal cord stimulators [113] for motor recovery and pain relief; cochlear implants [114] to revert deafness; pacemakers for cardiac dysfunctions; sensory and motor nerve stimulators [115].

This typology of approach finds application in every implantable device used for medical purpose. This work shows the feasibility of wirelessly remote control of a battery-less system. This approach will change the wide modern medicine world.

Appendix A

Insights

A.1 Comma to Dot Conversion Function

Generally, the Italian convention of the numeric representation is different from the American one. The Italian decimal numbers are expressed with a comma, while the American with a dot. Therefore, the following Matlab code is implemented to convert values expressed with the comma into values expressed with the dot. For simplicity, values are extracted by text file and rewritten in a different text file to do not lose the source values.

```
1 %% Comma to dot Conversion Function
2
3 clc;
4 clear all;
5 close all;
6
7 Data = fileread('C:\Users\fabio\OneDrive\Desktop\values_with_dot.txt');
8 Data = strrep(Data, ',', '.');
9 FID = fopen('C:\Users\fabio\OneDrive\Desktop\values_with_comma.txt', 'w');
10 fwrite(FID, Data, 'char');
11 fclose(FID);
```

Listing A.1: Matlab code: comma to dot conversion function.

A.2 Graph Code of Conductivity and Relative Permittivity

In this section is reported the implemented Matlab code to obtain the graphs of electrical conductivity σ and relative permittivity ϵ_r described in the Section 4.2.

```
1 %% Plot of Conductivity (S/m) of the following materials: Cortical Bone, Brain Grey Matter,
   Dura Madre, Cerebrospinal Fluid (CSF), Fat, Muscle and Dry Skin
2
3 clear
4 clc
5 close all
6
7 % Aquisition values from the table (file .txt)
8 A = readtable('Values_Conductivity.txt');
```

```

9 % Definition of variables
10 frequency = A{:,1};
11 cortical_bone_cond = A{:,2};
12 grey_matter_brain_cond = A{:,3};
13 dura_madre_cond = A{:,4};
14 cerebrospinal_fluid_cond = A{:,5};
15 fat_cond = A{:,6};
16 muscle_cond = A{:,7};
17 dry_skin_cond = A{:,8};
18
19 figure(1);
20 plot(frequency, cortical_bone_cond, '-r', 'LineWidth', 2);
21 hold on;
22 plot(frequency, grey_matter_brain_cond, '-c', 'LineWidth', 2);
23 plot(frequency, dura_madre_cond, '-g', 'LineWidth', 2);
24 plot(frequency, cerebrospinal_fluid_cond, '-k', 'LineWidth', 2);
25 plot(frequency, fat_cond, '-m', 'LineWidth', 2);
26 plot(frequency, muscle_cond, '-b', 'LineWidth', 2);
27 plot(frequency, dry_skin_cond, '-y', 'LineWidth', 2);
28 hold off
29
30 % Specs plot
31 grid on;
32 grid minor;
33 title('Behaviour of Conductivity (S/m) in function of Frequency (Hz) with step of 20 MHz');
34 xlabel('Frequency (Hz)');
35 ylabel('Conductivity (S/m)');
36 legend('Cortical Bone', 'Brain Grey Matter', 'Dura Madre', 'Cerebrospinal Fluid (CSF)', 'Fat', 'Muscle', 'Dry Skin', 'Location', 'northwest');
37 xlim([0 10e9]);
38 ylim([0 16]);
39
40
41 %% Plot of Relative Permittivity of the following materials: Cortical Bone, Brain Grey Matter, Dura Madre, Cerebrospinal Fluid (CSF), Fat, Muscle and Dry Skin
42
43 % Aquisition values from the table (file .txt)
44 B = readtable('Values_Permittivity.txt');
45
46 % Definition of variables
47 frequency = B{:,1};
48 cortical_bone_perm = B{:,2};
49 grey_matter_brain_perm = B{:,3};
50 dura_madre_perm = B{:,4};
51 cerebrospinal_fluid_perm = B{:,5};
52 fat_perm = B{:,6};
53 muscle_perm = B{:,7};
54 dry_skin_perm = B{:,8};
55
56 figure(2);
57 semilogx(frequency, cortical_bone_perm, '-r', 'LineWidth', 2);
58 hold on;
59 semilogx(frequency, grey_matter_brain_perm, '-c', 'LineWidth', 2);
60 semilogx(frequency, dura_madre_perm, '-g', 'LineWidth', 2);

```

```

61 semilogx(frequency, cerebrospinal_fluid_perm, '-k', 'LineWidth', 2);
62 semilogx(frequency, fat_perm, '-m', 'LineWidth', 2);
63 semilogx(frequency, muscle_perm, '-b', 'LineWidth', 2);
64 semilogx(frequency, dry_skin_perm, '-y', 'LineWidth', 2);
65 hold off
66
67 % Specs plot
68 grid on;
69 %grid minor;
70 title('Behaviour of Relative Permittivity in function of Frequency (Hz) with step of 20
      MHz');
71 xlabel('Frequency (Hz)');
72 ylabel('Relative Permittivity');
73 legend('Cortical Bone', 'Brain Grey Matter', 'Dura Madre', 'Cerebrospinal Fluid
      (CSF)', 'Fat', 'Muscle', 'Dry Skin', 'Location', 'northeast');
74 xlim([1e7 10e9]);
75 ylim([0 380]);

```

Listing A.2: Matlab code: plot of electrical conductivity σ and relative permittivity ϵ_r .

A.3 Graph Code of Gain and Efficiency of Power Amplifier

In this section is reported the implemented Matlab code to obtain the graphs of gain and PAE described in the Section 5.4.2.

```

1  %% Plot of Gain (dBm) and PAE (%) versus Pout (dBm)
2
3  clear
4  clc
5  close all
6
7  % Aquisition values from the table (file .txt)
8  A = readtable('gain_pae_value.txt');
9
10 % Definition of variables
11 p_out = A(:,1);
12 gain = A(:,2);
13 pae = A(:,3);
14
15 yyaxis left
16 plot(p_out, gain, '-ob', 'LineWidth', 2);
17 yyaxis right
18 plot(p_out, pae, '-or', 'LineWidth', 2);
19
20 grid on;
21 grid minor;
22 set(gcf, 'color', 'w');
23 title('Gain and PAE vs Pout at 430 MHz');
24 legend('Gain', 'PAE');
25
26 xlabel('Pout (dBm)');
27 xlim([30.5 34.5]);

```

```

28 yyaxis left
29 ylabel('GainL(dBm)');
30 ylim([30 60]);
31
32 yyaxis right
33 ylabel('PAEL(%)')
34 ylim([10 55]);

```

Listing A.3: Matlab code: plot of gain and efficiency of power amplifier.

A.4 Design Equations Resolution of Amplitude-Shift Keying

The implemented code based on the resolution of systems of equations allows making computation the design of amplitude-shift keying, described in detail in Section 5.3.1.

```

1 %% Design Equations Resolution
2
3 close all;
4 clc;
5 clear;
6
7 % Rb
8 % Declarations variables and equations
9 syms MI Vcc Ra Rb Vbe;
10 eqn1 = MI == (Vcc*Ra) / ((Vcc*(Ra + 2*Rb)) - (4*(Ra + Rb)*Vbe));
11 % Assignment of variables
12 vars1 = [MI Vcc Ra Vbe];
13 vals1 = sym([0.10 3.4 33 0.6]);
14 % Result
15 eqn1 = subs(eqn1,vars1,vals1);
16 Rb_result = vpasolve(eqn1, Rb)
17
18 % L2
19 % Declarations variables and equations
20 syms f L2 C2;
21 eqn2 = f == 1 / (2*pi*sqrt(L2*C2));
22 % Assignment of variables
23 vars2 = [f C2];
24 vals2 = sym([433e6 1e-12]);
25 % Result
26 eqn2 = subs(eqn2,vars2,vals2);
27 L2_result = vpasolve(eqn2, L2)
28
29 % Req
30 % Declarations variables and equations
31 syms Req M12 f L2 RL;
32 eqn3 = Req == (M12* 2*pi*f)^2 / ((L2* 2*pi*f)^2 / RL);
33 % Assignment of variables
34 vars3 = [M12 f L2 RL];
35 vals3 = sym([1.27e-8 433e6 L2_result 50]);
36 % Result
37 eqn3 = subs(eqn3,vars3,vals3);

```

```

38 Req_result = vpasolve(eqn3, Req)
39
40 % C1
41 % Declarations variables and equations
42 syms C1 f L1 Req;
43 eqn4 = C1 == 1 / ((2*pi*f)^2 *(L1 - (1.1552*Req / (2*pi*f))));
44 % Assignment of variables
45 vars4 = [f L1 Req];
46 vals4 = sym([433e6 45e-9 Req_result]);
47 % Result
48 eqn4 = subs(eqn4,vars4,vals4);
49 C1_result = vpasolve(eqn4, C1)
50
51 % C0
52 % Declarations variables and equations
53 syms C0 f Req;
54 eqn5 = C0 == 1 / ((2*pi*f) *(5.4466*Req));
55 % Assignment of variables
56 vars5 = [f Req];
57 vals5 = sym([433e6 Req_result]);
58 % Result
59 eqn5 = subs(eqn5,vars5,vals5);
60 C0_result = vpasolve(eqn5, C0)

```

Listing A.4: Matlab code: design equations resolution of amplitude-shift keying.

A.5 Absolute Decibel: dBm to Watt Conversion

The power is often expressed in decibels. The relation used to convert dBm to Watt is derived by (A.1):

$$P(W) = 1W \cdot \frac{10^{\frac{P(\text{dBm})}{10}}}{1000} = 10^{\frac{P(\text{dBm})-30}{10}} \quad (\text{A.1})$$

The following Matlab code plots its trend (Figure A.1).

```

1 %% dBm to Watts Conversion Function
2
3 clc;
4 clear all;
5 close all;
6
7 x = linspace(0,40,100);
8 P = 10.^((x-30)/10);
9
10 %Plotting the conversion function
11 figure(1);
12 hold on;
13 grid on;
14 grid minor;
15 xlabel("Powerd(dBm)");
16 ylabel("Powerd(mW)");
17 title("dBmdtodWatts");

```

```

18 plot(x, P, '-r', 'LineWidth', 2);
19 ylim([8 40])
20 ylim([0 1e1])
21
22 % Example 34 dBm
23 x_pos = 34; %dBm
24 y_pos = 10.^((x_pos-30)/10); %mW
25 plot(x_pos, y_pos, 'k*')

```

Listing A.5: Matlab code: dBm to Watts conversion function.

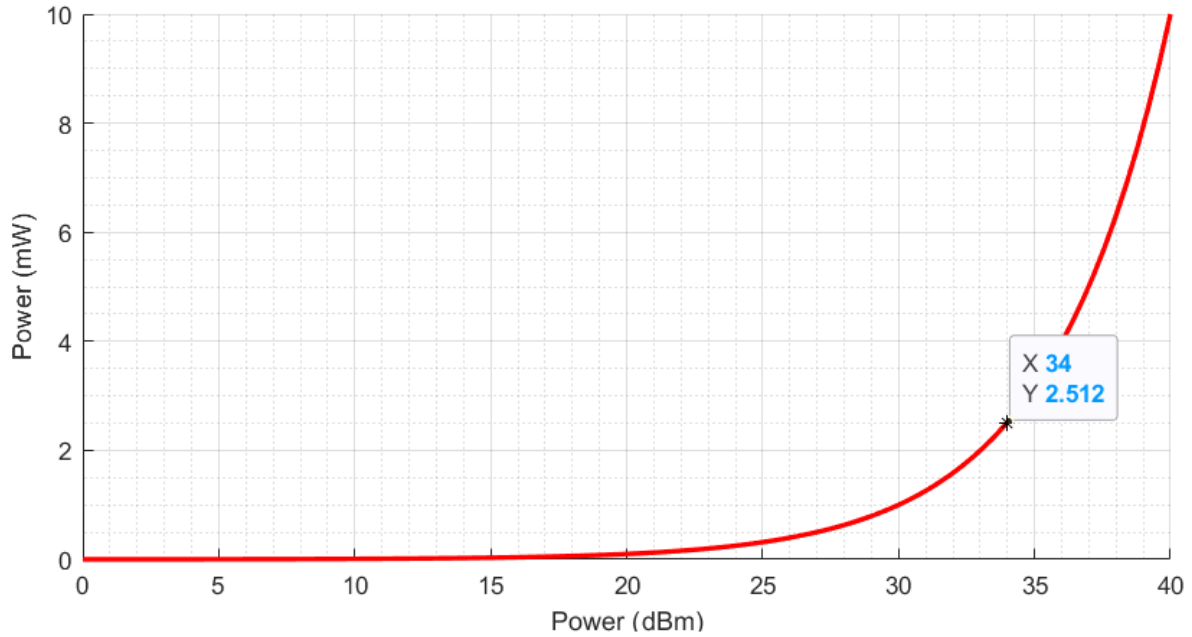


Figure A.1: dBm to Watt Conversion. Example value of 34 dBm with its respective value converted in mW.

A.6 Graph Code of S_{11} vs Frequency

The implemented code is used to compare the trends of the S_{11} simulated on Ansys HFSS and the measured with VNA instrument (Section 5.5.2).

```

1 %% S11 (dB) vs Frequency (Hz)
2
3 clear
4 clc
5 close all
6
7 % Aquisition values from the table (file .txt)
8 A = readtable('Values_S11_VNA.txt');
9 B = readtable('Values_S11_Ansys.csv');
10
11 % Definition of variables

```

```

12 frequency_VNA = A{:,1};
13 S11_VNA = A{:,2};
14 frequency_Ansys = B{:,1};
15 S11_Ansys = B{:,2};
16
17 figure(1);
18 plot(frequency_VNA, S11_VNA, '-b', 'LineWidth', 2);
19 hold on;
20 plot(frequency_Ansys, S11_Ansys, '--c', 'LineWidth', 2);
21 hold off;
22
23 % Specs plot
24 grid on;
25 grid minor;
26 set(gcf, 'color', 'w');
27 title('S11(dB) vs Frequency(Hz)');
28 xlabel('Frequency(Hz)');
29 ylabel('S11(dB)');
30 legend('VNA_Measurements', 'Ansys_HFSS_Simulations', 'Location', 'southeast');
31 xlim([0.7E+009 3E+009]);

```

Listing A.6: Matlab code: S_{11} (dB) vs frequency (Hz).

A.7 Graph Code of Absorbed Power

The implemented code reports the absorbed power $P_{absorbed}$ of the RF SWIPT transmitter described with a pie graph. Chapter 6 describes in detail the main considerations.

```

1 %% Plot Pie Graph Absorbed Power
2
3 clear
4 clc
5 close all
6
7 % Acquisition values from the table (file .txt)
8 X = [0.02475 0.02 0.5817 0.7631];
9 labels = {'Pierce_oscillator', 'ASK', 'PLL', 'PA'};
10 explode = [0 0 0 0];
11
12
13 % Definition of variables
14 pie(X, explode);
15 colormap([1 1 0;
16          0 1 0;
17          0 0 1;
18          1 0 0]);
19 legend(labels)
20 set(gcf, 'color', 'w');
21 %title('Absorbed power Pabsorbed(W) distribution of the Tx chain');

```

Listing A.7: Matlab code: pie graph of absorbed power

Bibliography

- [1] Philipp Gutruf et al. “Fully implantable optoelectronic systems for battery-free, multimodal operation in neuroscience research”. In: *Nature Electronics* 1.12 (2018), pp. 652–660.
- [2] Michael W Baker and Rahul Sarpeshkar. “Feedback analysis and design of RF power links for low-power bionic systems”. In: *IEEE transactions on biomedical circuits and systems* 1.1 (2007), pp. 28–38.
- [3] Sandro Carrara. “Body Dust: Well Beyond Wearable and Implantable Sensors”. In: *IEEE Sensors Journal* (2020).
- [4] Ryan M Neely et al. “Recent advances in neural dust: towards a neural interface platform”. In: *Current opinion in neurobiology* 50 (2018), pp. 64–71.
- [5] Denis Spirjakin, Alexander M Baranov, and Vladimir Sleptsov. “Design of smart dust sensor node for combustible gas leakage monitoring”. In: *2015 Federated Conference on Computer Science and Information Systems (FedCSIS)*. IEEE. 2015, pp. 1279–1283.
- [6] Gian Luca Barbruni et al. “Body Dust: Ultra-Low Power OOK Modulation Circuit for Wireless Data Transmission in Drinkable sub-100 μm -sized Biochips.” In: *ArXiv: 1912.02670* (2019).
- [7] Jan Snoeijs, Georgiou Pantelis, and Carrara Sandro. “CMOS body dust—Towards drinkable diagnostics.” In: *2017 IEEE Biomedical Circuits and Systems Conference (BioCAS)* (2017).
- [8] Dongjin Seo et al. “Neural dust: An ultrasonic, low power solution for chronic brain-machine interfaces”. In: *ArXiv:1307.2196* (2013).
- [9] Michael J Sailor and Jamie R Link. “Smart dust: nanostructured devices in a grain of sand”. In: *Chemical Communications* 11 (2005), pp. 1375–1383.
- [10] Edward Bloch, Yvonne Luo, and Lyndon da Cruz. “Advances in retinal prosthesis systems”. In: *Therapeutic advances in ophthalmology* 11 (2019).
- [11] Elisa Castaldi et al. “Visual bold response in late blind subjects with Argus II retinal prosthesis”. In: *PLoS biology* 14.10 (2016).
- [12] David Borton et al. “Personalized Neuroprosthetics”. In: *Science Translational Medicine* 5.210 (2013). ISSN: 1946-6234.
- [13] Hilda Petrs-Silva and Rafael Linden. “Advances in gene therapy technologies to treat retinitis pigmentosa”. In: *Clinical Ophthalmology (Auckland, NZ)* 8 (2014), p. 127.
- [14] Diego Ghezzi. “Retinal prostheses: progress toward the next generation implants”. In: *Frontiers in neuroscience* 9 (2015), p. 290.
- [15] James R Golden et al. “Simulation of visual perception and learning with a retinal prosthesis”. In: *Journal of neural engineering* 16.2 (2019).
- [16] Kai-Wen Yang, Keonghwan Oh, and Sohmyung Ha. “Challenges in Scaling Down of Free-Floating Implantable Neural Interfaces to Millimeter Scale”. In: *IEEE Access* 8 (2020), pp. 133295–133320.

-
- [17] Benjamin C Johnson et al. “StimDust: A 6.5 mm³, wireless ultrasonic peripheral nerve stimulator with 82% peak chip efficiency”. In: *2018 IEEE Custom Integrated Circuits Conference (CICC)*. IEEE. 2018, pp. 1–4.
- [18] David K Piech et al. “StimDust: A mm-scale implantable wireless precision neural stimulator with ultrasonic power and communication”. In: *ArXiv:1807.07590* (2018).
- [19] Adam Khalifa et al. “The microbead: A 0.009 mm³ implantable wireless neural stimulator”. In: *IEEE transactions on biomedical circuits and systems* 13.5 (2019), pp. 971–985.
- [20] Nur Ahmadi et al. “Towards a distributed, chronically-implantable neural interface”. In: *2019 9th International IEEE/EMBS Conference on Neural Engineering (NER)*. IEEE. 2019, pp. 719–724.
- [21] Jihun Lee et al. “Wireless Ensembles of Sub-mm Microimplants Communicating as a Network near 1 GHz in a Neural Application”. In: *bioRxiv* (2020).
- [22] Vincent W Leung et al. “A CMOS distributed sensor system for high-density wireless neural implants for brain-machine interfaces”. In: *ESSCIRC 2018-IEEE 44th European Solid State Circuits Conference (ESSCIRC)*. IEEE. 2018, pp. 230–233.
- [23] Jongyup Lim et al. “26.9 A 0.19×0.17 mm² Wireless Neural Recording IC for Motor Prediction with Near-Infrared-Based Power and Data Telemetry”. In: *2020 IEEE International Solid-State Circuits Conference-(ISSCC)*. IEEE. 2020, pp. 416–418.
- [24] Jayant Charthad et al. “A mm-sized wireless implantable device for electrical stimulation of peripheral nerves”. In: *IEEE transactions on biomedical circuits and systems* 12.2 (2018), pp. 257–270.
- [25] Sohmyung Ha et al. “Silicon-integrated high-density electrocortical interfaces”. In: *Proceedings of the IEEE* 105.1 (2016), pp. 11–33.
- [26] Xiaojuan Wei and Jing Liu. “Power sources and electrical recharging strategies for implantable medical devices”. In: *Frontiers of Energy and Power Engineering in China* 2 (Mar. 2008), pp. 1–13.
- [27] D. Kwon and G. A. Rincon-Mora. “A 2- μ m BiCMOS Rectifier-Free AC–DC Piezoelectric Energy Harvester-Charger IC”. In: *IEEE Transactions on Biomedical Circuits and Systems* 4.6 (2010), pp. 400–409.
- [28] S. Ayazian and A. Hassibi. “Delivering optical power to subcutaneous implanted devices”. In: *2011 Annual International Conference of the IEEE Engineering in Medicine and Biology Society*. 2011, pp. 2874–2877.
- [29] K. Goto et al. “An implantable power supply with an optically rechargeable lithium battery”. In: *IEEE Transactions on Biomedical Engineering* 48.7 (2001), pp. 830–833.
- [30] Y. Zhang et al. “A Batteryless 19 μ W MICS/ISM-Band Energy Harvesting Body Sensor Node SoC for ExG Applications”. In: *IEEE Journal of Solid-State Circuits* 48.1 (2013), pp. 199–213.
- [31] Haiyu Huang et al. “RFID tag helix antenna sensors for wireless drug dosage monitoring”. In: *IEEE journal of translational engineering in health and medicine* 2 (2014), pp. 1–8.
- [32] Andrew Ma and Ada SY Poon. “Midfield wireless power transfer for bioelectronics”. In: *IEEE Circuits and Systems Magazine* 15.2 (2015), pp. 54–60.
- [33] Han-Joon Kim et al. “Review of near-field wireless power and communication for biomedical applications”. In: *IEEE Access* 5 (2017), pp. 21264–21285.
- [34] Gürkan Yılmaz. “Wireless power transfer and data communication for intracranial neural implants case study”. Tech. rep. EPFL, 2014.

- [35] Reza Erfani, Fatemeh Marefat, and Pedram Mohseni. “Biosafety considerations of a capacitive link for wireless power transfer to biomedical implants”. In: *2018 IEEE Biomedical Circuits and Systems Conference (BioCAS)*. IEEE. 2018, pp. 1–4.
- [36] David K Piech et al. “A wireless millimetre-scale implantable neural stimulator with ultrasonically powered bidirectional communication”. In: *Nature Biomedical Engineering* 4.2 (2020), pp. 207–222.
- [37] G. L. Barbruni et al. “Miniaturised Wireless Power Transfer Systems for Neurostimulation: A Review”. In: *IEEE Transactions on Biomedical Circuits and Systems* 14.6 (2020), pp. 1160–1178.
- [38] Shaul Ozeri and Doron Shmilovitz. “Ultrasonic transcutaneous energy transfer for powering implanted devices”. In: *Ultrasonics* 50.6 (2010), pp. 556–566.
- [39] David B Christensen, Hamid Basaeri, and Shad Roundy. “A computationally efficient technique to model depth, orientation and alignment via ray tracing in acoustic power transfer systems”. In: *Smart Materials and Structures* 26.12 (2017), p. 125020.
- [40] Rangarajan Jegadeesan et al. “Wireless power delivery to flexible subcutaneous implants using capacitive coupling”. In: *IEEE Transactions on Microwave Theory and Techniques* 65.1 (2016), pp. 280–292.
- [41] Reid R Harrison. “Designing efficient inductive power links for implantable devices”. In: *2007 IEEE International Symposium on Circuits and Systems*. IEEE. 2007, pp. 2080–2083.
- [42] U. Jow and M. Ghovanloo. “Design and Optimization of Printed Spiral Coils for Efficient Inductive Power Transmission”. In: *2007 14th IEEE International Conference on Electronics, Circuits and Systems*. 2007, pp. 70–73.
- [43] Andre Kurs et al. “Wireless power transfer via strongly coupled magnetic resonances”. In: *science* 317.5834 (2007), pp. 83–86.
- [44] Mehdi Kiani, Uei-Ming Jow, and Maysam Ghovanloo. “Design and optimization of a 3-coil inductive link for efficient wireless power transmission”. In: *IEEE transactions on biomedical circuits and systems* 5.6 (2011), pp. 579–591.
- [45] S Abdollah Mirbozorgi, Pyungwoo Yeon, and Maysam Ghovanloo. “Robust wireless power transmission to mm-sized free-floating distributed implants”. In: *IEEE transactions on biomedical circuits and systems* 11.3 (2017), pp. 692–702.
- [46] Manuel Monge et al. “A fully intraocular high-density self-calibrating epiretinal prosthesis”. In: *IEEE transactions on biomedical circuits and systems* 7.6 (2013), pp. 747–760.
- [47] Byunghun Lee and Maysam Ghovanloo. “An overview of data telemetry in inductively powered implantable biomedical devices”. In: *IEEE Communications Magazine* 57.2 (2019), pp. 74–80.
- [48] Wentai Liu et al. “A neuro-stimulus chip with telemetry unit for retinal prosthetic device”. In: *IEEE Journal of Solid-State Circuits* 35.10 (2000), pp. 1487–1497.
- [49] Michael Catrysse, Bart Hermans, and Robert Puers. “An inductive power system with integrated bi-directional data-transmission”. In: *Sensors and Actuators A: Physical* 115.2-3 (2004), pp. 221–229.
- [50] Sohmyung Ha et al. “Energy recycling telemetry IC with simultaneous 11.5 mW power and 6.78 Mb/s backward data delivery over a single 13.56 MHz inductive link”. In: *IEEE Journal of Solid-State Circuits* 51.11 (2016), pp. 2664–2678.
- [51] Ahmed I Al-Kalbani, Mehmet R Yuce, and Jean-Michel Redouté. “Performance of a biomedical implant communication system using PWM coded ASK”. In: *2012 International Symposium on Communications and Information Technologies (ISCIT)*. IEEE. 2012, pp. 133–138.

- [52] Jan Rabaey. *Low power design essentials*. Springer Science & Business Media, 2009.
- [53] Mircea R Stan and Wayne P Burleson. “Bus-invert coding for low-power I/O”. In: *IEEE Transactions on very large scale integration (VLSI) systems* 3.1 (1995), pp. 49–58.
- [54] Guillaume Simard, Mohamad Sawan, and Daniel Massicotte. “High-speed OQPSK and efficient power transfer through inductive link for biomedical implants”. In: *IEEE Transactions on biomedical circuits and systems* 4.3 (2010), pp. 192–200.
- [55] Fuqin Xiong. *Digital Modulation Techniques, Second Edition (Artech House Telecommunications Library)*. USA: Artech House, Inc., 2006. ISBN: 1580538630.
- [56] Yamu Hu and Mohamad Sawan. “A fully integrated low-power BPSK demodulator for implantable medical devices”. In: *IEEE Transactions on Circuits and Systems I: Regular Papers* 52.12 (2005), pp. 2552–2562.
- [57] Ahmed Al-Kalbani, Mehmet R Yuce, and Jean-Michel Redouté. “Electromagnetic interference in brain implants using multiple coils: biosafety and data communication performance”. In: *IEEE transactions on electromagnetic compatibility* 56.2 (2013), pp. 490–493.
- [58] Mehdi Lotfi Navaii, Mohsen Jalali, and Hamed Sadjedi. “A 34-pJ/bit area-efficient ASK demodulator based on switching-mode signal shaping”. In: *IEEE Transactions on Circuits and Systems II: Express Briefs* 64.6 (2016), pp. 640–644.
- [59] M Ghovanloo and K Najafi. “High data rate frequency shift keying demodulation for wireless biomedical implants”. In: *IEEE Transactions on Circuits and Systems I* 51.12 (2004), pp. 2374–2383.
- [60] Zhu Liu and Zhizhang David Chen. “New Wireless Power Transfer Systems Against Misalignments between Transmitters and Receivers”. In: *2018 18th International Symposium on Antenna Technology and Applied Electromagnetics (ANTEM)*. IEEE, 2018, pp. 1–2.
- [61] Bo Zhao et al. “A Batteryless Padless Crystalless 116 μm x 116 μm Dielet Near-Field Radio With On-Chip Coil Antenna”. In: *IEEE Journal of Solid-State Circuits* 55.2 (2019), pp. 249–260.
- [62] Andreas Christ et al. “Assessing human exposure to electromagnetic fields from wireless power transmission systems”. In: *Proceedings of the IEEE* 101.6 (2013), pp. 1482–1493.
- [63] “IEEE Standard for Safety Levels with Respect to Human Exposure to Radio Frequency Electromagnetic Fields, 3 kHz to 300 GHz”. In: *IEEE Std C95.1, 1999 Edition* (1999), pp. 1–83.
- [64] “IEEE Recommended Practice for Measurements and Computations of Electric, Magnetic, and Electromagnetic Fields with Respect to Human Exposure to Such Fields, 0 Hz to 100 kHz”. In: *IEEE Std C95.3.1-2010* (2010), pp. 1–101.
- [65] “IEEE Recommended Practice for Determining the Peak Spatial-Average Specific Absorption Rate (SAR) in the Human Head from Wireless Communications Devices: Measurement Techniques - Redline”. In: *IEEE Std 1528-2013 (Revision of IEEE Std 1528-2003) - Redline* (2013), pp. 1–500.
- [66] Salah Yahya. “Factors Influencing the EM Interaction between Mobile Phone Antennas and Human Head”. In: vol. 166. June 2011, pp. 106–120.
- [67] Antonios Drossos, Veli Santomaa, and Niels Kuster. “The dependence of electromagnetic energy absorption upon human head tissue composition in the frequency range of 300-3000 MHz”. In: *IEEE transactions on microwave theory and techniques* 48.11 (2000), pp. 1988–1995.
- [68] Hannah McCann, Giampaolo Pisano, and Leandro Beltrachini. “Variation in reported human head tissue electrical conductivity values”. In: *Brain topography* 32.5 (2019), pp. 825–858.

- [69] Andreas Christ et al. “The dependence of electromagnetic far-field absorption on body tissue composition in the frequency range from 300 MHz to 6 GHz”. In: *IEEE transactions on microwave theory and techniques* 54.5 (2006), pp. 2188–2195.
- [70] Fabrizio Pizzotti. “Tessuti organici e assorbimento specifico da tecnologia WiFi”. In: *Arpa Emilia-Romagna Rivista* N. 4 luglio-agosto (2008).
- [71] *Calculation of the Dielectric Properties of Body Tissues in the frequency range 10 Hz ÷ 100 GHz*. URL: <http://niremf.ifac.cnr.it/tissprop/htmlclie/htmlclie.php>.
- [72] A.S. Poon, S. O’Driscoll, and T.H. Meng. “Optimal operating frequency in wireless power transmission for implantable devices”. In: *2007 29th Annual International Conference of the IEEE Engineering in Medicine and Biology Society*. IEEE. 2007, pp. 5673–5678.
- [73] S Abdollah Mirbozorgi et al. “A single-chip full-duplex high speed transceiver for multi-site stimulating and recording neural implants”. In: *IEEE transactions on biomedical circuits and systems* 10.3 (2015), pp. 643–653.
- [74] Fields into Biological. “Coupling of electromagnetic fields into biological systems”. In: *Electromagnetic Fields in Biological Systems* (2016), p. 1.
- [75] Syahrim Azhan, Nurliza Salim, and Hafizah Binti. “Remote Wireless System Using Amplitude Shift Keying Modulation”. In: Dec. 2010.
- [76] Cotter Sayre. *Complete Wireless Design*. Vol. 3. McGrawHill Professional, 2008.
- [77] Willy M Sansen. *Analog design essentials*. Vol. 859. Springer Science & Business Media, 2007.
- [78] Kin Keung Lee, Kristian Granhaug, and Nikolaj Andersen. “A study of low-power crystal oscillator design”. In: *2013 NORCHIP*. IEEE. 2013, pp. 1–4.
- [79] Ramon Cerda. “Pierce-gate crystal oscillator, an introduction”. In: *Crytek Corporation* (2008), p. 1.
- [80] S. Raza. “Fundamentals: Understanding the basics of the Pierce oscillator”. In: 53 (July 2011).
- [81] Behzad Razavi and Razavi Behzad. *RF microelectronics*. Vol. 2. Prentice Hall New York, 2012.
- [82] Dante Del Corso. *Elettronica per telecomunicazioni: transistori e operazionali fuori linearità, phase-lock loop, conversione A/D e D/A, interfacciamento e interconnessioni*. Libreria editrice universitaria Levrotto & Bella, 1990.
- [83] Ray Sun. “How to Design and Debug a Phase-Locked Loop (PLL) Circuit”. In: ().
- [84] Chua-Chin Wang et al. “Self-sampled all-MOS ASK demodulator for lower ISM band applications”. In: *IEEE Transactions on Circuits and Systems II: Express Briefs* 57.4 (2010), pp. 265–269.
- [85] Jeff Gambino et al. “Reliability of an Al₂O₃/SiO₂ MIM Capacitor for 180nm (3.3 V) Technology”. In: *2019 IEEE International Reliability Physics Symposium (IRPS)*. IEEE. 2019, pp. 1–5.
- [86] Mehdi Lotfi Navaii, Hamed Sadjedi, and Amir Sarrafzadeh. “Efficient ASK data and power transmission by the class-E with a switchable tuned network”. In: *IEEE Transactions on Circuits and Systems I: Regular Papers* 65.10 (2018), pp. 3255–3266.
- [87] Saad Mutashar Abbas, MA Hannan, and AS Salina. “Efficient class-E design for inductive powering wireless biotelemetry applications”. In: *2012 International Conference on Biomedical Engineering (ICoBE)*. IEEE. 2012, pp. 445–449.
- [88] Frederick H Raab. “Effects of circuit variations on the class E tuned power amplifier”. In: *IEEE Journal of Solid-State Circuits* 13.2 (1978), pp. 239–247.

- [89] Anthony N Laskovski and Mehmet R Yuce. “Analysis of class-E amplifier with mixed data modulation for biotelemetry”. In: *2007 29th Annual International Conference of the IEEE Engineering in Medicine and Biology Society*. IEEE. 2007, pp. 5679–5682.
- [90] M. K. Kazimierczuk. “Class E tuned power amplifier with nonsinusoidal output voltage”. In: *IEEE Journal of Solid-State Circuits* 21.4 (1986), pp. 575–581.
- [91] Mohammad Mahdi Ahmadi and Mohammadreza Sarbandi-Farahani. “A Class-E Power and Data Transmitter with On–Off Keying Data Modulation for Wireless Power and Data Transmission to Medical Implants”. In: *Circuits, Systems, and Signal Processing* (2020), pp. 1–13.
- [92] Nathan O Sokal. “Class-E RF power amplifiers”. In: *Qex* 204.1 (2001), pp. 9–20.
- [93] Bill Slade. “Notes on designing class-E RF power amplifiers”. In: *no. May* (2010), pp. 1–11.
- [94] Enver G Kilinc, Catherine Dehollain, and Franco Maloberti. “Design and optimization of inductive power transmission for implantable sensor system”. In: *2010 XIth international workshop on symbolic and numerical methods, modeling and applications to circuit design (SM2ACD)*. IEEE. 2010, pp. 1–5.
- [95] Kanber Mithat Silay, Catherine Dehollain, and Michel Declercq. “Improvement of power efficiency of inductive links for implantable devices”. In: *2008 Ph. D. Research in Microelectronics and Electronics*. IEEE. 2008, pp. 229–232.
- [96] Ahmed Ibrahim and Mehdi Kiani. “A figure-of-merit for design and optimization of inductive power transmission links for millimeter-sized biomedical implants”. In: *IEEE transactions on biomedical circuits and systems* 10.6 (2016), pp. 1100–1111.
- [97] Uei-Ming Jow and Maysam Ghovanloo. “Design and optimization of printed spiral coils for efficient transcutaneous inductive power transmission”. In: *IEEE Transactions on biomedical circuits and systems* 1.3 (2007), pp. 193–202.
- [98] Uei-Ming Jow and Maysam Ghovanloo. “Modeling and optimization of printed spiral coils in air, saline, and muscle tissue environments”. In: *IEEE transactions on biomedical circuits and systems* 3.5 (2009), pp. 339–347.
- [99] Bert Lenaerts and Robert Puers. *Omnidirectional inductive powering for biomedical implants*. Springer, 2009.
- [100] Uei-Ming Jow and Maysam Ghovanloo. “Optimization of a multiband wireless link for neuro-prosthetic implantable devices”. In: *2008 IEEE Biomedical Circuits and Systems Conference*. IEEE. 2008, pp. 97–100.
- [101] *Ansys HFSS Frequency Electromagnetic Simulation Software*. URL: <https://www.ansys.com/it-it/products/electronics/ansys-hfss>.
- [102] Dukju Ahn and Maysam Ghovanloo. “Optimal design of wireless power transmission links for millimeter-sized biomedical implants”. In: *IEEE transactions on biomedical circuits and systems* 10.1 (2015), pp. 125–137.
- [103] Zhi Yang, Wentai Liu, and Eric Basham. “Inductor modeling in wireless links for implantable electronics”. In: *IEEE Transactions on Magnetics* 43.10 (2007), pp. 3851–3860.
- [104] J. Parramon et al. “ASIC-based batteryless implantable telemetry microsystem for recording purposes”. In: *Proceedings of the 19th Annual International Conference of the IEEE Engineering in Medicine and Biology Society*. Vol. 5. IEEE. 1997, pp. 2225–2228.
- [105] K. Abdelhalim et al. “915-MHz FSK/OOK wireless neural recording SoC with 64 mixed-signal FIR filters”. In: *IEEE Journal of Solid-State Circuits* 48.10 (2013), pp. 2478–2493.
- [106] M Kumarasamy Raja and Yong Ping Xu. “A 52 pJ/bit OOK Transmitter with adaptable data rate”. In: *2008 IEEE Asian Solid-State Circuits Conference*. IEEE. 2008, pp. 341–344.

- [107] A. Bonfanti et al. “A multi-channel low-power IC for neural spike recording with data compression and narrowband 400-MHz MC-FSK wireless transmission”. In: *2010 Proceedings of ESSCIRC*. IEEE. 2010, pp. 330–333.
- [108] Zhang Qi, Kuang Xiaofei, and Wu Nanjian. “An ultra-low-power RF transceiver for WBANs in medical applications”. In: *Journal of Semiconductors* 32.6 (2011).
- [109] I. Intzes, H. Meng, and J. Cosmas. “High Data Rate FinFET On-Off Keying Transmitter for Wireless Capsule Endoscopy”. In: (2018).
- [110] M. Yousefi et al. “A 430 MHz fully integrated high efficiency OOK transmitter for wireless biomedical application”. In: *International Journal of Electrical & Computer Sciences* 4 (2014), pp. 1–5.
- [111] Syahrim Azhan, Nurliza Salim, and Hafizah Binti. “Remote Wireless System Using Amplitude Shift Keying Modulation”. In: Dec. 2010.
- [112] Alim Louis Benabid et al. “Deep brain stimulation of the subthalamic nucleus for the treatment of Parkinson’s disease”. In: *The Lancet Neurology* 8.1 (2009), pp. 67–81.
- [113] Fabien B Wagner et al. “Targeted neurotechnology restores walking in humans with spinal cord injury”. In: *Nature* 563.7729 (2018), pp. 65–71.
- [114] Jay T Rubinstein. “Paediatric cochlear implantation: prosthetic hearing and language development”. In: *The Lancet* 360.9331 (2002), pp. 483–485.
- [115] Stanisa Raspopovic et al. “Restoring natural sensory feedback in real-time bidirectional hand prostheses”. In: *Science translational medicine* 6.222 (2014).
- [116] Adam Khalifa et al. “A compact, low-power, fully analog implantable microstimulator”. In: *2016 IEEE International Symposium on Circuits and Systems (ISCAS)*. IEEE. 2016, pp. 2435–2438.
- [117] *Fundamental Operating Principles*. Tech. rep. 2010. Chap. 3, pp. 29–59.
- [118] Maysam Ghovanloo and Khalil Najafi. “A wideband frequency-shift keying wireless link for inductively powered biomedical implants”. In: *IEEE Transactions on Circuits and Systems I: Regular Papers* 51.12 (2004), pp. 2374–2383.
- [119] Gürkan Yilmaz, Oğuz Atasoy, and Catherine Dehollain. “Wireless energy and data transfer for in-vivo epileptic focus localization”. In: *IEEE Sensors Journal* 13.11 (2013), pp. 4172–4179.
- [120] Eric Y Chow et al. “Wireless powering and the study of RF propagation through ocular tissue for development of implantable sensors”. In: *IEEE Transactions on Antennas and Propagation* 59.6 (2011), pp. 2379–2387.
- [121] Keith Mathieson et al. “Photovoltaic retinal prosthesis with high pixel density”. In: *Nature photonics* 6.6 (2012), pp. 391–397.

Index

- 2-coils IPT link, 15
- 3-coils IPT link, 17
- 4-coils IPT link, 17

- Acoustic power transfer, 13
- Age-related Macular Degeneration, 2
- Amplitude-shift keying, 20
- Angular rotation, 26
- Ansys HFSS, 64
- ASK modulator, 46

- Blindness, 2
- Body Dust, 1
- Body energy harvesters, 11
- Bus invert, 21

- Capacitive power transfer, 14
- Class-AB Power Amplifier, 55
- Class-E Power Amplifier, 47
- CMOS technology, 4
- Cortical visual prostheses, 2

- Darlington emitter-follower, 47, 74
- Data encoding, 21
- Data Rate, 32
- Data Transfer, 4
- Demodulator, 46
- Downlink communication, 20

- Electrical conductivity, 29
- ENGINI, 8

- Far-field radiation, 13
- Figure of merit, 74
- Fraunhofer distance, 12
- Frequency, 27, 31
- Frequency phase-shift, 32
- Frequency-shift keying, 22

- Gain, 55

- Human body tissue, 27
- IEEE Standard, 27

- Implantable electronic unit, 2
- Implantable medical device, 1
- Implantable pulse generator, 2
- Implanted batteries, 11
- Inductive power transfer, 15

- Lambert-Beer, 14

- Maxwell-Faraday, 27
- Micro-electrode array, 1
- Microbead, 7
- Miniaturisation, 4
- Misalignment, 4, 26
- Modulation index, 20
- Modulation technique, 32

- Neural Dust, 1
- Neurograins, 8
- Neurostimulation, 2

- On-fff keying, 21
- On-off keying, 32

- Packaging, 4
- Parallel resonant frequency, 37
- Phase-locked loop, 42
- Phase-shift keying, 22, 32
- Phosphenes, 2
- Photoreceptors, 2
- Pierce Oscillator, 36
- Power added efficiency, 55
- Power consumption, 4
- Printed circuit board, 76
- Printed spiral coils, 64
- Pulse Modulation Technique, 22
- Pulse position modulation, 32

- Quartz, 36

- Relative permittivity, 29
- Reliability, 4
- Retinal ganglion cell, 3
- Retinitis Pigmentosa, 2

Robustness, 20

Safety, 4

Scalability, 4

Series resonant frequency, 37

Smart Dust, 1

Spatial selectivity, 4

Specific absorption rate, 27

StimDust, 6

T-pad voltage divider, 50

Tissue adsorption, 29

Transcranial wires, 2

Transcutaneous wires, 2

Transmitter, 34

Transmitting coil, 64

Uplink communication, 20

Visual restorative medicine, 3

Visual retinal prostheses, 2

Wire wound coils, 64

Wireless data transmission, 19

Wireless power transfer, 4, 11